2019

The role of VEC and local atomic environment in structural transitions and stability of complex intermetallic compounds through theoretical and experimental study of γ-brasses

Stephanie L. Eveland

Iowa State University

Recommended Citation

The role of VEC and local atomic environment in structural transitions and stability of complex intermetallic compounds through theoretical and experimental study of γ-brasses

by

Stephanie Eveland

A dissertation submitted to the graduate faculty

in partial fulfillment of the requirements for the degree of

DOCTOR OF PHILOSOPHY

Major: Chemistry

Program of Study Committee:
Gordon Miller, Major Professor
Joseph Burnett
Patricia Thiel
Theresa Windus
Yulia Zaikina

Iowa State University

Ames, Iowa

2019

DEDICATION

I'd like to thank my friends and family, first and foremost to my parents, for always encouraging me to pursue my dreams even if that meant moving halfway across the country. I owe a debt of gratitude to my church-family for keeping my head on straight when times were tough, and to my fur-baby Charlie, who with his walnut sized brain brought me comfort and a sense of purpose when life wasn't hopping along so well. My friends and fellow graduate students, Becca Hansen, Ellie Fought, and Laura Burns, their encouragement and reminders to break for lunch were key to my success in the final days of this process. I'd like to thank David, for keeping me laughing, being my rock in stormy seas and reminding me that my value comes from Christ, for always reaching everything on the top shelf, and joining in on this adventure called life. And many thanks to everyone who helped me through these past ten years of education. I would not have become the person I am today without all of you, and my degrees would be less meaningful without all of you to celebrate with.

TABLE OF CONTENTS

LIST OF FIGURES

LIST OF TABLES

NOMENCLATURE

VEC	Valence Electron Concentration
TB-LMTO-ASA	Tight Binding Linear Muffin Tin Orbital Atomic Sphere Approximation
VASP	Vienna ab-initio Simulation Package
SEM	Scanning Electron Microscopy
PAW	Projector Augmented Wave
SCXRD	Single Crystal X-ray Diffraction
PXRD	Powder X-ray Diffraction
SQUID	Super Conducting Quantum Interference Device
MPMS	Magnetic Property Measurement System
ICSD	International Crystal Structure Database
EDS	Energy Dispersive Spectroscopy
DFT	Density Functional Theory
RBM	Rigid Band Model

ACKNOWLEDGMENTS

I would like to thank my Ph.D advisor Dr. Gordon J. Miller for teaching me to approach the world of scientific inquiry as a critical and actively engaged participant and most importantly to take ownership of my research. After six years I have learned just as much about myself as I have intermetallics and solid state chemistry while under his training. I would like to thank all my committee members, Dr.s Theresa Windus, Vitalij Pecharsky, Yulia Zaikina, Patricia Thiel, and Joseph Burnett for the unique perspective and expertise they each brought to my career at Iowa State.

I would also like to thank some of the professors I have had the opportunity to teach with, Dr. Irmi Schewe-Miller, Dr. Joseph Burnett, Dr. Sara Pistolesi, and Dr. Robyn Anand for understanding the delicate equilibrium between research and teaching. Specifically, to Dr. Joseph Burnett for having my back my first semester when teaching was new, and students were scary. I'd like to thank the members of the Miller group for taking the time to teach me both computational and experimental techniques, listen and challenge me during group meetings, and to kill the occasional cockroach. Also, thanks to Ames lab for funding support. (Contract No. DE-AC02-07CH11358)

ABSTRACT

The fusion of computational and synthetic techniques provides a powerful investigative arsenal for a systematic consideration of the factors governing the structural makeup and observed physical properties of complex intermetallic compounds such as the non-uniform mixed sites in $Mn_{2+x}Zn_{11-x}$, VEC driven structural transition in $Mn_{5-y}Al_{8-x}Zn_{x+y}$, and atypical atomic decoration of Cu_9Al_4 γ-brasses. Classic solid state synthetic techniques, self-flux techniques, as well as multiple structural characterization methods such as X-ray diffraction and electron microscopy were employed in the experimental portion of this work. Magnetic susceptibility measurements were utilized when appropriate in the study of the γ- brasses of $Mn_{2+x}Zn_{11-x}$. To compliment the information from synthetic experiments DFT based first-principles computational methods, TB-LMTO-ASA and VASP, were used to investigate the electronic structure of hypothetical colorings of unit cells with mixed site occupancy, and in order to structurally relax the unit cell near an experimentally observed structural transition.

In $Mn_{2+x}Zn_{11-x}$ a phase width was identified experimentally, and electronic structure calculations were used to show the role of heteroatmic bonding in promoting stability through inter- and intra-cluster bonding leading to overall stability near $Mn_{2.2}Zn_{10.8}$.

Through systematic doping of Mn_5Al_8 with Zn a series of compounds ($Mn_{5-y}Al_{8-x}Zn_{x+y}$) was created highlighting the role of VEC in the stability of different structures without introducing size effects changing atomic radii by less than 15%. Zn does not preferentially substitute Al, it dopes into both Mn and Al rich sites and as a net process

lowers the VEC. The structural transition from R3m to I-43m passes through a phase width ending in $Mn_{2+x}Zn_{11-x}$.

The primitive decoration of Cu_9Al_4 has two geometrically and compositionally distinct 26-atom clusters which increases the number of unique connections and increases the number of heteroatomic contacts as compared to body centered decorations, by spreading out Al to two separate crystallographic sites with optimized contact distances.

CHAPTER 1.   INTRODUCTION

Defining Complex Metallic Alloys

Intermetallic compounds contain two or more metallic or semi-metallic elements. Minority components may include nonmetallic elements. [1] Intermetallic compounds cannot always be simply interpreted in terms of covalent bonding in the way that organic molecules can due to the mobile nature of the valence electrons in metallic and semi-metallic elements. Another feature of intermetallic compounds is the formation of crystal structures that differ from one or both constituent elements' crystal structure, often in complex ways. This is observed in γ-brasses such as $Li_{21}Si_5$ in which the two clusters of the unit cell have different compositions and complementing charges, [2] as well as in quasicrystals (QC) where slight changes in composition lead to drastically different observed structures [3]. The structural and compositional complexity of intermetallic compounds and related oxides can be used to tune the physical characteristics and properties of materials such as observed in $RhP_{3-x}Si_x$ and $YBa_2Cu_3O_{7-x}$ [4-5] where small deviations in composition have drastic changes to physical properties such as magnetism.

Complex Metallic Alloys (CMAs), a subgroup of intermetallic compounds, may not always form crystalline products like most other intermetallic compounds, but through electron microscopy and X-ray fluorescence techniques, similar studies into stoichiometric variation, defects, and structural transitions can be performed [6]. Even for inexpensive, earth-abundant, and non-toxic materials, such as those found in various types of steels and industrial alloys, it is important to understand how small variations in stoichiometry, defects, or structural variation are correlated with changes in physical properties. An example of how physical properties can change is the industrial alloy Aluminum 7075, a candidate for

selective laser melting, which benefits from additions of 4% Si to diminish cracks and grain elongation in bulk materials. [7]

Structural Complexity In Intermetallic Compounds

CMAs are of great interest to a swath of science and engineering researchers due to their structural complexity, solid solution behavior and local atomic environments absent in normal metallic alloys. [8] The large unit cells often associated with CMAs tend to have large variations in local atomic environments. However, these complex unit cells can often be described in terms of packings of well-defined clusters, chains, or networks of atoms [9-10]. These clusters, chains, and networks can display partial chemical disorder, ordered vacancies and slight structural variation, all of which influence the electronic structure. Many CMA electronic structures feature gaps or pseudogaps near the Fermi energies (EF) which distinguish them from the observed electronic structures of normal metallic compounds. The stability ranges of CMAs are often associated with specific valence electron per atom (e/a) ratios [11].

Hume-Rothery and the e/a trend
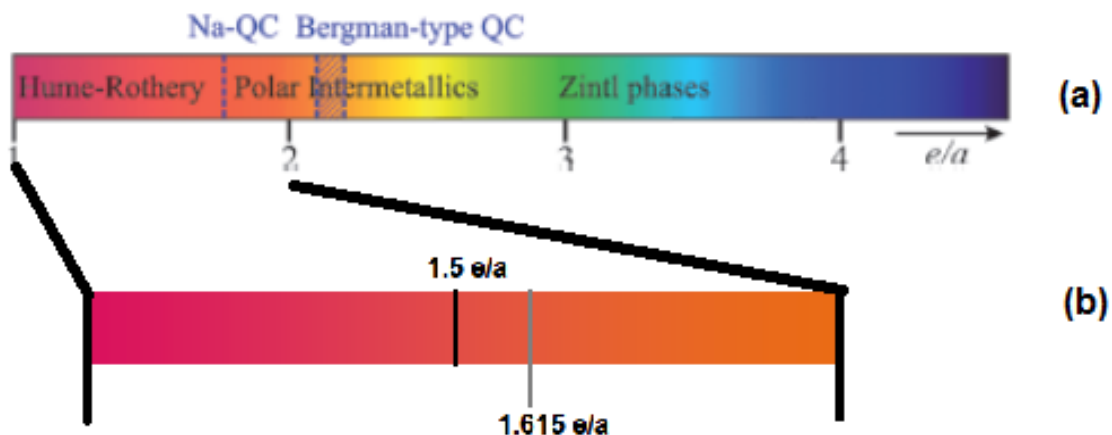
Figure 1.1: (a)The general trend of *e/a* ratios highlighting Hume-Rothery phases, Polar Intermetallics, quasicrystals (QC), and Zintl phases. [12] (b) cut out of range 1.0 – 2.0 *e/a* featuring the ideal γ-brass formation valence electron concentration of 1.615 *e/a*.

The stability ranges of CMAs of various degrees of structural complexity can be described using the Hume-Rothery rules. For low e/a ratios multicenter bonding flourishes leading to densely packed structures. As the *e/a* ratio increases, the electrons become increasingly localized in two-center bonds and covalent-bonded open networks stuffed with active metals are the norm. Figure 1.1. shows the general ranges of *e/a* emphasizing the region from 1-2 e/a where Hume-Rothery phases exist and polar intermetallics begin to form.

How *e/a* is calculated is dependent on the constituent elements. In Hume-Rothery compounds such as Cu_5Zn_8 [19], the valence electrons of late and post-transition metals and the total number of atoms in the formula unit are used to determine the *e/a* ratio. For structures containing elements with larger differences in electronegativity, the counting scheme includes the electrons of the late transition metals and post-transition metals as well as active metals but excludes the active metals from the number of atoms in the polar-covalent structure. For a Zintl phase compounds such as NaTl, the polar-covalent structure forms from a diamond lattice of Tl atoms and the tetrahedral holes are filled with Na atoms [11]. Tl brings 3 valence electrons and Na contributes 1 electron, however, the Na, as an active metal, is not included in the polar covalent diamond structure and leaves the VEC at (3 Tl electrons + 1 Na electron)/1Tl atom or 4.0 *e/a*.

A connection between stability and chemical composition within the γ-brass family was accomplished using Hume-Rothery's valence electron counting rules, noting that Cu_5Zn_8, Ag_5Zn_8, and Au_5Zn_8 formed with ideally 21 valence *s* and *p* electrons per 13 atoms in the formula unit, shown at 1.615 *e/a* in Figure 1.1 (b) [12]. Mizutani assigned γ-brasses into three groups according to their constituent elements: Group I γ-brasses have a monovalent noble metal and a polyvalent metal or metalloid with a well-defined valency;

Group II γ-brasses have a partially-filled 3*d* metal with a fully-filled valence *d*-band element (e.g. Zn or Cd) or a trivalent metal such as Al; and Group III γ-brasses consist of cases that do not include transition metals [12, 14]. In particular, it is the Group II γ-brasses with the partially-filled *d* orbitals that provide an avenue to study the complex relationships among physical structure, electronic structure, composition, and atomic decoration.

Properties in relationship to symmetry changes

Magnetic properties depend on the relative location of atoms with magnetic moments. The Hume-Rothery trends show that structure, therefore the relative location of atoms, can be dependent on the overall *e/a* ratio. In an effort to modify or enhance magnetic properties, non-magnetic elements are occasionally added as dopants to magnetic compounds like what is observed in silicon-based semiconductors [15]. Manyala et al. showed that doping Mn into FeSi allows paramagnetic behavior to be observed down to 1.7 K and an insulator-to-metal transition occurs almost immediately, $Fe_{1-x}Mn_xSi$ (x ~0.01) [15]. Without proper preemptive investigation, there is a possibility that adding a dopant will negatively disrupt the desired magnetic ordering due to changes in symmetry.

While systematically doping a nonmagnetic element for a magnetic element the *e/a* ratio may alter enough for a change in overall structural symmetry to occur. For example, the Wyckoff site in a cubic structure with antiferromagnetic coupling where the original magnetic moment resides may split into three sites. It is possible that up to all three sites could exhibit magnetic moments (see Figures 1.2 (b), (c) and (d)). In certain cases, such as antiferromagnetic coupling the magnetic moments may become frustrated due to the presence of a non-optimized moment on the neighboring atom of two out of 3 sites, Figure 1.2 (b). To alleviate that frustration the moments may reorient themselves, as illustrated in Figure 1.2 (c) and (d). The degree to which they reorient could result in a canted (Figure 1.2

(c)) or ferromagnetic alignment Figure 1.2 (d), which could be counter to the desired

orientation [16]. If instead of a symmetry transformation, the original Wyckoff site exhibited

mixed occupation of a magnetic and nonmagnetic element, the magnetic ordering of the unit

cell is not reoriented, but the magnitude of the magnetic moment would be dampened as

shown in green in Figure 1.2 (e).
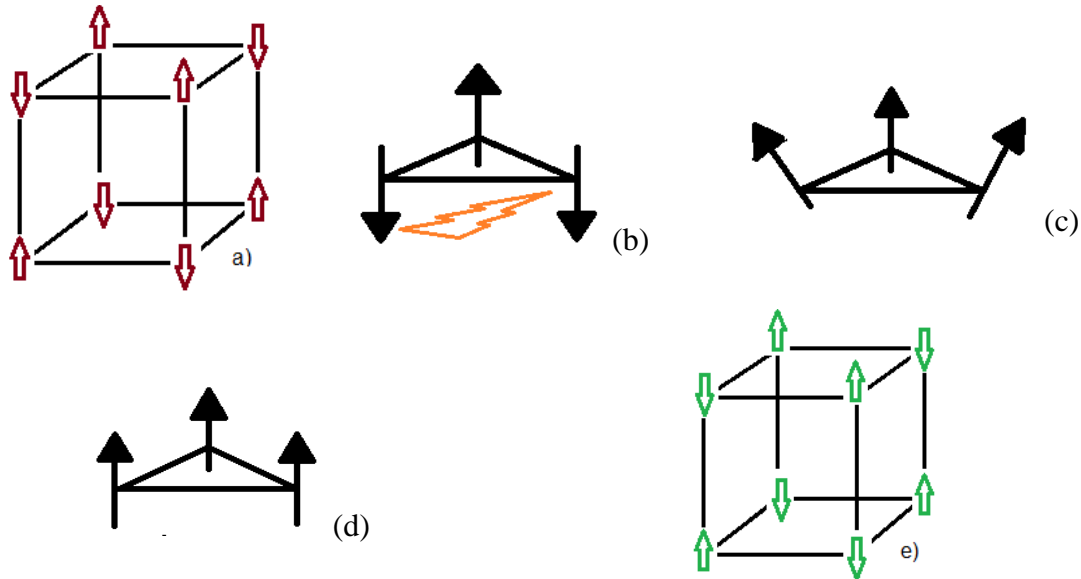
Figure 1.2: Effects of breaking symmetry vs mixed site occupation on Magnetic moments: Green arrows indicate dampened magnitude magnetic moment, red indicates original magnetic moment magnitude remains (a) Antiferromagnetic ordering across a primitive cubic unit cell (b) one Wyckoff site splits into three due to structural transition leaving two of the three sites with frustrated magnetic moments, (c) magnetic frustration is relieved by reordering the orientation to canted orientation (d) frustration relieved by oriented ferromagnetically in the three sites (e) Symmetry remains the same and the resulting magnetic moment is dampened by site mixing between magnetic and nonmagnetic elements

Understanding the electronic rationale for mixed-site occupancy versus structural

transformation in Hume-Rothery phases is crucial for explaining the observed physical

phenomena, as well as directing the synthesis of targeted phases with specific properties.

Γ-brasses in Detail

Γ-brasses are ideal structures for investigating the relationships between e/a structural transitions and mixed-site occupancy both experimentally and computationally. They exhibit a cornucopia of structural variations; mixed occupancy of one or more Wyckoff sites and phase widths are commonly observed. In all γ-brasses, a 26-atom cluster serves as the base unit in different packing schemes of γ-brasses. Face-centered packings of 26-atom clusters are observed in MnGa [16], primitive decorations of a body-centered packing are observed in Cu_9Al_4 [18-19], body-centered packings in Cu_5Zn_8 [20] as well as rhombohedral or distorted body-centered packings in Mn_5Al_8[20]. Each 26-atom cluster is composed of four concentric shells of symmetry-equivalent atoms. The first and second shells are tetrahedra, the third shell is an octahedron and the fourth is a cuboctahedron. In the distorted body-centered packing (rhombohedral packing) the concentric shells of atoms are not all symmetry-equivalent, but each shell is composed of two or three sets of symmetry-equivalent atoms.

Table 1.1: Prototypical packings of 26-atom clusters in γ- brasses

	GaCr	Cu_9Al_4	Cu_5Zn_8	Mn_5Al_8
S.G.	$R3m$	$P\bar{4}3m$	$I\bar{4}3m$	R3m
Type	ξ_2-GaMn	Cu_9Al_4	Cu_5Zn_8	Cr_5Al_8
VEC*	1.5	1.615	1.615	1.846
ref.	[17]	[18,19]	[20]	[21]

*The VEC is calculated based on stoichiometric compositions of the prototypical colorings shown in row 2.

The variation between distinct decorations and distortions of 26-atom packings within the γ-brass family has been intrinsically tied to the e/a ratio by previous work [22]. Site mixing, as well as non-stoichiometric chemical formulae, are a common observation within the Group II γ-brasses. The appearance of ordered vacancies is a suggested counterbalance resisting structural transition when e/a ratios begin to increase beyond the stable range for a

particular packing of 26-atom clusters [23]. For example, Co–Zn γ-brasses show evidence of these ordered vacancies on the inner tetrahedra on the 26-atom cluster [24].

Symbiosis: Computation and Experiment

Predicting the formation of new compounds by means of ab-initio methods is not impossible; however, it is limited in what we can derive from electronic structure calculations, even the highest quality ones. The factors driving the experimentally determined structures are both thermodynamic and kinetic in nature, although, ab-initio calculations assume conditions at zero kelvin, an unrealistic temperature for experimental observation and structure determination. Thermodynamic characteristics of solids such as total energies, heat capacities, and local and collective atomic displacements have been improved recently, most demonstrably by Dronskowski et. al., although limitations in the validity of heat capacity terms calculated from the distribution of electrons over temperature-independent bands persists. The heat capacity at low temperatures is extremely small and scales linearly with temperature in ab-initio calculations such as VASP [25].
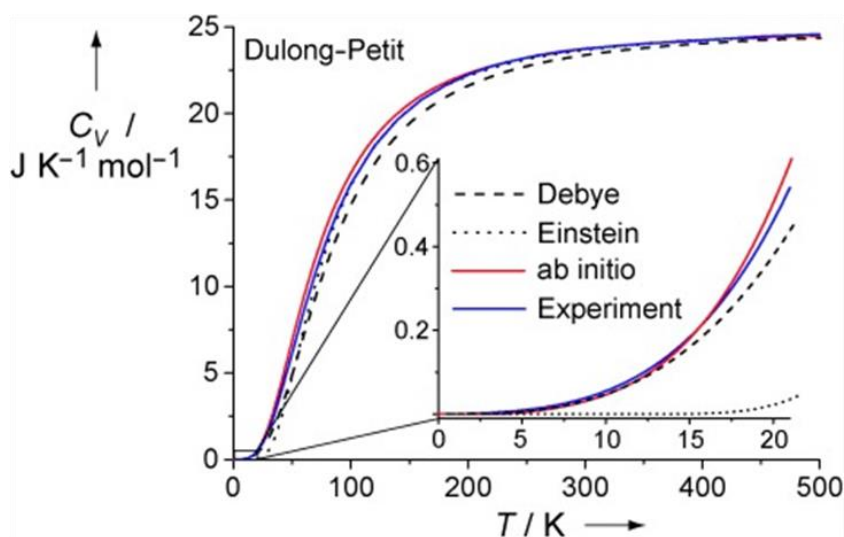
Figure 1.3: Density-Functional Theory calculated heat capacity of FCC Cu at constant volume as a function of temperature referenced to experimental values [26].

It should be noted that for the systems studied in the following work, temperature dependent limitations were not a factor. Crystallographic information determined at room temperature (0.0257 eV above absolute zero) were used as input for ab-initio calculations and when decorated in different colorings the energy differences between competing colorings were outside the 0.0257 eV difference.

The coloring problems in intermetallic compounds

Coloring is defined as the decoration of a structure in which there are more than one element and more than one atomic site making the network of an intermetallic compound [27]. A coloring problem includes determining how elements distribute across the network of an intermetallic compound. Understanding it is essential for investigating the driving forces behind any structure-property relationship. A preferred coloring scheme provides the lowest total energy. However, comparing two different models must be done within the same frame of reference; only same-composition lattices can be directly compared.
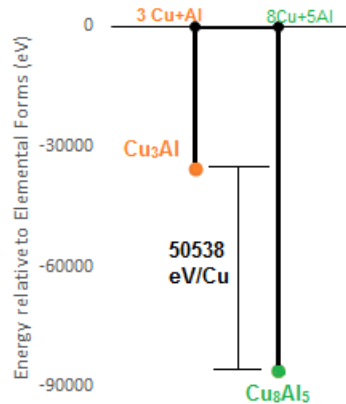
Table 1.2: Disproportionation comparison of different composition lattices

Disproportionation reaction	Relative ΔE/Cu (eV)
$4Cu_3Al \rightarrow 3Cu(FCC) + Al(FCC)$	+ 50538.37
$Cu_{32}Al_{20} \rightarrow 8Cu (FCC) + 5Al(FCC)$	0

When comparing two competing structures, a same-composition option is not always available. Comparing the free energy using disproportionation can be a first step in deciding

between two competing structures by calculating how much each phase is favored over the constituent elemental forms. Table 1.2 shows the disproportionation comparison of Cu_8Al_5 (shown as $Cu_{32}Al_{20}$) compared to a competing high-temperature binary Cu_3Al [28]. The Cu_8Al_5 structure is favored as compared to the constituent elements FCC Cu and FCC Al by 50.5 keV/Cu atom than Cu_3Al.

Phase stability

The DOS is a plot of energy vs all possible populated and unpopulated states of an individual site or total elemental contribution and when integrated up to the Fermi level, shows the number of valence electrons. The DOS is heavily relied upon when assessing the stabilities of structures and coloring options of intermetallic compounds. A significant feature of this electronic structure diagram often located at or near EF is a pseudogap, which is a region of the electronic structure diagram where there are very few states populated relative to the energy levels above and below [29]. Compounds such as γ-brasses that have a pseudogap at or near EF are favorable relative to any distorted structure and are more likely to form at the calculated composition. In situations where the pseudogap is a significant distance from the EF or is not present at all, a distortion, structural or magnetic may be observed. In particular, the presence of a peak at EF in the DOS indicates a possible structural or electronic instability, a sign that long-range magnetic ordering is another possible outlet to alleviate this electronic instability. Peaks at the Fermi level also can indicate that the chosen structure type is likely to distort from the calculated composition. The rhombohedral ternary model "$Mn_{10}Al_6Zn_4$" (see Chapter 5) shows a peak in the DOS near the EF and a significant pseudogap below the EF. The peak, a marker of instability for the calculated composition of 154 electrons, along with the gap at 150.01 electrons (0.3 eV below the Fermi level) agree with the experimental results that a composition with more Zn

and less Al, which lowers the electron count from the computational model, is observed in $Mn_{5-y}Al_{8-x}Zn_{x+y}$ SCXRD refinements. This generalization must be considered carefully due to the limitations of the rigid band model in the $Mn_{5-y}Al_{8-x}Zn_{x+y}$ system.

The Rigid Band Model (RBM) states that the electronic structure of any lightly doped alloy remains the same as that of the pure metal [30]. This can be interpreted to mean that small changes in composition should not affect the shape of a DOS significantly and can be used for small changes in valence electron count. Applying the RBM to hypothetical compositions of a calculated structure allows one to shift the Fermi level up to incorporate more electrons or shift the Fermi level down to incorporate fewer electrons. The assumption is the shape of a given DOS or COHP curve will not change significantly between two same-composition coloring models and allows an approximate prediction of structural formation and stability with shifting e/a ratio. This is especially important for Hume-Rothery phases due to their previously mentioned structural dependence on e/a ratios. However, when the electronic structure does change significantly between colorings and the compositional change one is investigating requires adding or mixing with an element of a considerably different basis set, RBM must be applied with care. The RBM, its application and limitations will be discussed in detail in the following chapters.

Computation to explain observed phase widths and coloring

Beyond looking at the electronic structure of a single coloring, one can determine relative stabilities of various, same-composition colorings by comparing the total energies, numbers of heteroatomic contacts, and numbers of homoatomic contacts [31]. Intermetallic solids, especially CMAs, can have large numbers of distinct atomic interactions, and optimization of these pairwise orbital overlaps is one way of explaining the compositional phase width and the site preferences of the constituent elements. By analyzing the COHP curves of several same-composition coloring schemes, one can see which arrangement and the corresponding numbers of heteroatomic and homoatomic contacts lead to the lowest total energy.

These methods can help determine the role specific bonding interactions have in the overall stability of a structure. Determining the energy relative to EF at which the total COHP curve becomes antibonding and assists in understanding if bonding is optimized at the calculated composition and can provide insight into experimentally observed mixed occupancy of individual sites. If the COHP indicates that homoatomic interactions are antibonding, but heteroatomic interaction would be bonding, then mixing site occupations could alleviate the instability by providing an opportunity to have both homoatomic and heteroatomic overlap. In Figure 1.4 the Zn–Zn COHP stays positive above the EF while the Mn–Mn COHP crosses below the E_F.
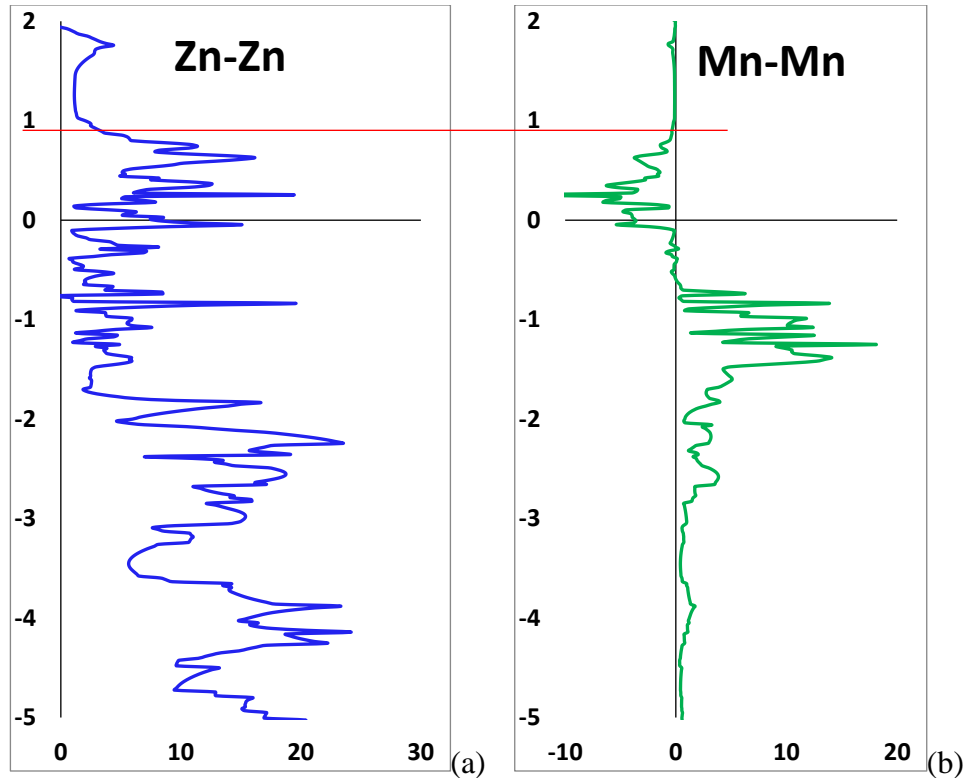
Figure 1.4: Elemental COHP (a) Zn–Zn COHP curve showing large bonding region from -5 eV to 1 eV above the calculated Fermi energy then becoming antibonding at approximately 2 eV above the Fermi energy. (b) Mn–Mn COHP curve showing bonding overlap between -5 eV and -0.75 eV which changes to nonbonding and then antibonding overlap at approximate the calculated Fermi energy.

The RBM can also be applied to the analysis of COHP data. By changing the number of valence electrons, one can shift the E_F higher or lower which gives insight into the role of individual overlaps with changing *e/a*. In Figure 1.4(a) increasing the *e/a* ratio, by hypothesizing a Zn-rich composition, would shift the E_F higher to the location of the red line at the edge of a wide pseudogap. This region is indicative of a nonbonding portion of the COHP curve in Figure 1.4(b), essentially optimizing the Zn–Zn interactions. However, if that same location were the E_F, the Mn–Mn interactions shown in Figure 1.4(b) would have to pass through an antibonding region. This instability would likely prevent this structure from forming with the composition at the *e/a* ratio represented by the red line. Using this

process, maximum and minimum composition ranges can be estimated from these calculations and used to support SCXRD refinements or guide synthetic strategies. See Chapter 3 for a more detailed discussion.

After a phase width has been observed experimentally or suggested by means of first-principles calculations, the remaining question is whether or not computational experiments can assist in the confirmation of atomic decoration and provide support for mixed sites refined via SCXRD. The integrated density of states (IDOS) evaluated at individual sites can assist in making a qualitative determination of such. In Table 1.3 the IDOS for one coloring of "$Mn_{21}Al_{57}$" is shown (See Chapter 4).

Table 1.3: Charge Density Analysis of "$Mn_{21}Al_{57}$" γ-Brass

Location (multiplicity)	Δ IDOS/ atom
IT(1)	Al: (+0.206)
IT(3)	Al: (+0.219)
OT(1)	Mn: (-0.108)
OT(3)	Mn: (+0.008)
OH(3a)	Mn: (-0.028)
OH(3b)	Al: (+0.116)
CO(3a)	Al: (+0.218)
CO(6)	Al: (+0.150)
CO(3b)	Al: (+0.202)

In a binary model such as "$Mn_{21}Al_{57}$" comparisons can be made between sites occupied by the same element to determine the locations more likely to mix between the constituent elements or accept to a dopant atom. The values in Table 1.3 are the number of electrons a neutral atom would contain minus the number of electrons calculated for that site by IDOS. Sites with negative IDOS/Atom values indicate more electrons than the neutral atom designated by the coloring for the site in question. Positive IDOS/Atom values indicate the site is allocated fewer electrons than the neutral atom assigned by the coloring.

In "Mn$_{21}$Al$_{57}$" Mn is considered to have seven valence electrons and Al is assigned three valence electrons. Due to the different basis sets for Mn 4s/3d and Al 4s/4p in "Mn$_{21}$Al$_{57}$", mixing between the main group element and the transition metal cannot be directly inferred from the IDOS/Atom listed in Table 1.3. What can be inferred is the location most likely to accept a dopant such as Zn, as is observed in the Mn$_{5-y}$Al$_{8-x}$Zn$_{x+y}$. When Zn replaces an Al site the electron density at that site is lowered because d orbitals are not among the basis set at an Al site and the, Zn is considered to provide just two valence electrons.

When Zn replaces a Mn occupied site, where the d orbitals are included in the basis set at that site, Zn is assigned twelve valence electrons replacing a seven valence electron atom, thereby increasing the electron density at that site. All Al occupied sites, all are positive indicating a lower valence electron element like Zn could mix into these sites. At values of +0.219 and +0.218 IDOS/Atom, the IT(3) and CO(3a) have the greatest driving force for Zn replacing Al over the other Al sites. More detail is provided in Chapter 4.

Even with limitations discussed above, reliance on the atomic spheres approximation, possible insufficiency of the RBM, and temperature dependence of electron-electron interactions in ab-initio calculations in metallic systems, the usefulness of electronic structure calculations cannot be overstated. A wealth of calculations have been performed on analogous systems under comparable conditions and provide points of reference for results of future analysis of electronic structure calculations. One can compare features of electronic structure diagrams such as gaps, pseudogaps, band splitting, and overall shape. The trends in bonding and site energy between similar systems allow one to make inferences into the chemical behavior of the system, such as structural stability and compositional phase width.

In this dissertation, DOS and COHP curves and their comparison to previous work are used extensively to rationalize structure formation at experimentally observed compositions for the group II γ-brasses of the Mn–Zn, and Mn–Zn–Al systems as well as provide a rationale for the formation of an atypical γ-brass in Cu_9Al_4.

Purpose of Dissertation

The tie that binds the following projects together is to investigate the role of local atomic interactions and valence electron concentration in structural and compositional variations of complex intermetallic structures. The use of first principles methods of calculation helps rationalize the decoration of CMAs by investigating three γ-brass structure types (Ni_2Zn_{11} cI52, Cu_5Al_8 cI52, and Mn_5Al_8 cP78) [32, 20, 21]. The result is an avenue for understanding how various local environments affect structure-property relationships. An attempt is made to combine theory and experiment to present both quantitative and qualitative indications for individual structure, decoration, and formation.

Organizational Overview

This work consists of six Chapters.

Chapter two of this thesis contains the experimental and computational methods used in this body of research to address the questions raised in previous sections via a thorough investigation described in the subsequent three chapters.

Chapter three discusses the structural and electronic characteristics of $Mn_{2+x}Zn_{11-x}$ (x=0.06-0.60) and makes connections to previous work regarding $CoPdZn_{11}$ and Ni_2Zn_{11}, discusses Mn site preferences as well as the effect of local environment on stability specifically concerning Zn $3d$-$3d$ repulsion, and examines the possibility for doping through charge density analysis. Site preference of Mn for one of the two 8c sites is confirmed.

Chapter four studies the Mn–Zn-Al system using experimental and theoretical means; studying the effect of introducing and increasing Zn content in the Mn5Al8 compound transforming the structure from R3m to I-43m ending in a binary I-43m $Mn_{2+x}Zn_{11-x}$ γ-brass. This work shows clear preferences for atomic site occupation for Zn in both rhombohedral and cubic decorations. In binary and ternary cubic unit cells Mn atoms prefer to occupy 8c sites and additional Mn occupies the 12e sites.

Chapter five examines the electronic structural factors governing the preference of Cu_9Al_4 to form as a primitive decorated γ-brass and the implications on the coloring problem as the composition moves toward Cu_8Al_5.

Chapter 6 ties together all the conclusions made by the body of work represented in Chapters three through five.

The appendix includes a list of all additional reactions and experiments that I attempted during my time as a Ph.D. student and any additional structures that were discovered.

References

[1] Westbrook, J. H.; Fleischer, R. L. Intermetallic Compounds: Principles and Practice, Wiley, 2002

 [2] H.-G. von Schnering and R. Nesper, "Li21Si5 Hume Rothery and Zintl," Journal of Solid State Chemistry, pp. 47-52, 1987

[3] Pham, Joyce and Meng, Fanqiang and Lynn, Matthew J. and Ma, Tao and Kreyssig, Andreas and Kramer, Matthew J. and Goldman, Alan I. and Miller, Gordon From Quasicrystals to Crystals with Interpenetrating Icosahedra in Ca-Au-Al: In Situ Variable-Temperature Transformation, Journal of the American Chemical Society, 140, 4, 1337-1347, 2018

[4] M. Kirschen, H. Vincent, Ch. Perrier, P. Chaudouet, B. Chenevier, R. Madar, Synthesis and crystal structure of rhodium and iridium new phospho-silicides, Materials Research Bulletin, Volume 30, Issue 4, 1995, Pages 507-513]

[5] Nakao, J.; Miura, K.; Noboru, Kiyoshi, T; Shin-ichi, U.; Hidenori, T.; Takahiro, W.;

Shoji, K.; Superconductivity in $YBa_2Cu_3O_{7-x}$ in a 100 Tesla magnetic field, Nature, 332, 816references here, using a style appropriate to journals or papers in your field. Single space, double space between.]

[6] Fei Chen, Zhiqiang Cao, Gang Chen, Xizhou Kai, Jili Wu, Yutao Zhao, Synchrotron radiation micro-beam analysis of the effect of strontium on primary silicon in Zn–27Al–3Si alloy, Journal of Alloys and Compounds, Volume 749,2018, 575-579

[7] Montero-Sistiaga, M.; Mertens, R.; Vrancken, B.; Wang, X.; Van Hooreweder, B.; Kruth, J.; Van humbeeck, J. Changing the alloy composition of Al7075 for better processability by selective laser melting, Journal of Materials Processing, 238, 437-445

[8] Dubois, J. M.; Belin-Ferré, E.; Feuerbacher, M., Complex Metallic Alloys: Fundamentals and Applications, Wiley, New York, 2010.

[9] Toombs, Asa; Miller, Gordon Rhombohedral Distortion of the cubic MgCu2-type Structure in Ca2, *Crystals* 2018, *8*(5), 186

[10] Melissa L. Rhodehouse, Thomas Bell, Volodymyr Smetana, Anja-Verena Mudring, and Gerd H. Meyer, From the Nonexistent Polar Intermetallic Pt3Pr4 via Pt2–xPr3 to Pt/Sn/Pr Ternaries, *Inorganic Chemistry* 2018 *57* (16), 9949-9961

[11] Schneider J., Cation short-range order in non-stoichiometric NaTl, Mater. Sci. Forum, Vol. 27/28, 1988, p 63-68

[12] Mizutani, U., Hume-Rothery Rules for Structurally Complex Alloy Phases, CRC Press, New York, 2010

[13] Smetana, V.; Lin, Q.; Pratt, D.; Kressig, A.; Ramanazoglu M.; Corbett, J.; Goldman, A.; Miller, G., A Sodium- Containing Quasicrystal: Using Gold To Enhance Sodium's Covalency in Intermetallic Compounds, Angewandte Chemie, 51, 51, 12699-12702

[14] A. F. Phragmen and G. Westgren, "X-Ray Studies on Alloys," *Metallwirtschaft,* pp. 380-385, 1929.

[15] Ncholu Manyala, Yvan Sidis, John F. DiTusa, Gabriel Aeppli, David P. Young, and Zachary Fisk Large anomalous Hall effect in a silicon-based magnetic semiconductor Nature Materials 3, 255-262 (2004)

[16] M. Kuepers, L. Lutz-Kappelman, Yuemei Zhang, G. J. Miller, B. P. T. Fokwa, Spin Frustration and Magnetic Ordering from One-Dimensional Stacking of Cr3 Triangles in TiCrIr2B2 Inorganic Chemistry, 2016, 5640 – 5648

[17] Gourdon O., and Miller G.J., Reinvestigation of the GaMn structure and theoretical studies of its electronic and magnetic properties, J. Solid State Chem., Vol. 173, 2003, p 137-147

[18] Arnberg L., and Westman S., Crystal Perfection in a Non-Centrosymmetrie Alloy. Refinement and Test of Twinning of the γ-Cu9Al4 Structure, Acta Crystallogr. A, Vol. 34, 1978, p 399-404

[19] De Lima J.C., Triches D.M., Dos Santos V.H.F., and Grandi T.A., Formation of γ-$Cu_{67}Al_{33}$ alloy by mechanical alloying, J. Alloys Compd., Vol. 282, 1999, p 258-260

[20] Degtyareva V.F., Sakharov M.K., Novokhatskaya N.I., Degtyareva O., Dera P., Mao H.K., and Hemley R.J., Stability of Hume-Rothery Phases in Cu-Zn Alloys at Pressures up to 50 GPa, Metall. Mater. Trans. A, Vol. 37, 2006, p 3381-3385

[21] S. Thimmaiah, Z. Tener, T. N. Lamichhane, P. C. Canfield and G. J. Miller, "Crystal structure, homogeneity range and electronic structure of rhombohedral γ-Mn5Al8," *Zeitschrift fuer Kristallographie-Crystalline Materials,* vol. 232, no. 7-9, pp. 601-610, 2017

[22] Hornfeck, Wolfgang; Thimmiaiah, Srinivasa; Lee, Stephen, Structure composition Relations for the Partly Disordered Hume-Rothery Phase $Ir_{7+78}Zn_{97-11d}$ Chemistry: a European journal. , 2004, Vol.10(18), p.4616-4626

[23] Thimmaiah, Srinivasa; Miller, Gordon J., Rhombohedrally Distorted γ-Au 5– x Zn 8+ y Phases in the Au–Zn System, Inorganic chemistry. , 2013, Vol.52(3), p.1328-1337

[24] Xie, Weiwei; Miller, Gordon J., New Co–Pd–Zn γ-Brasses with Dilute Ferrimagnetism and Co2Zn11 Revisited: Establishing the Synergism between Theory and Experiment, Chemistry of Materials, 2014, pgs 2624-2634

[25] Stoffel, R. P.; Wessel, C.; Lumey, M.-W.; Dronskowski, R. Angew. Chem. Int. Ed. 2010, 49, 5242.

[26] G. Ahlers, Rev. Sci. Instrum. 1966, 37, 477. *AND G. K. White, S. J. Collocott, J. Phys. Chem. Ref. Data 1984, 13, 1251.*

[27] Miller G. J. Eur. J. Inorg. Chem. 1998, 523

[28] W.G. Wang, J.H. Li, Y. Dai & B.X. Liu (2010) *Ab initio* calculations to determine the formation enthalpy of Cu3Au phases, Philosophical Magazine Letters, 90:11, 801-807, DOI: 10.1080/09500839.2010.507177

[29] Gourdon, O.; Gout, D.; Miller, G. J. In Encyclopedia of Condensed Matter Physics; Franco, B., Gerald, L. L., Peter, W., Eds.; Elsevier: Oxford, 2005, p 409.

[30] *Uichiro Mizutani (2001). Introduction to the electron Theory of metals. Cambridge University Press*

[31] Kohn, W.; Sham, L. J. Phys. Rev. 1965, 140, A1133. & Gimarc, B. M. J. Am. Chem. Soc. 1983, 105, 1979

[32] A. Johansson, H. Ljung and S. Westman, "X-Ray and Neutron Diffraction Studies on γ-Ni, Zn and γ-Fe. Zn," *Acta Chemica Scandinavica,* vol. 22, pp. 2743-2753, 1968.

CHAPTER 2.   EXPERIMENTAL AND COMPUTATIONAL TECHNIQUES

This Chapter includes a description of experimental techniques and theoretical approaches used to complete the dissertation work, their purposes, and limitations. The specific issues surrounding each technique can be found in the corresponding Chapters.

Computational Methods

Two main methods were employed in the following work. The basis sets for each are different, so that the total energies cannot be directly compared, but when these methods are employed in tandem information provided can answer a wider variety of questions. The speed at which TB-LMTO-ASA provides approximations of electronic structure calculations is valuable, however TB-LMTO -ASA does not optimize structural coordinates effectively. Starting from experimental coordinates VASP can optimize structures and then utilizing TB-LMTO-ASA quickly producing electronic structure diagrams provides insight into structural changes effect on electronic structure and behavior.

Tight Binding Linear Muffin-Tin Orbital with the Atomic Sphere Approximation (TB-LMTO-ASA)[1].

TB-LMTO-ASA is one of the first principles calculation techniques used to evaluate the electronic structure of the systems described below. This computational approach uses a superposition of an approximate set of wave functions for isolated, spherical atoms. The electrons are tightly bound to the atom and interactions with neighboring atoms are affected by overlap. The total wave function is a sum of Bloch wavefunctions with 3D space divided into overlapping spherical. Any remaining space is filled with so-called empty spheres. TB-LMTO-ASA involves a self-consistent calculation which gives its output a high level of accuracy, although the Atomic Spheres Approximation does levy some limitations due to neglecting the contributions of interstitial regions filled with empty spheres.

Vienna Ab-initio Simulation Package (VASP).[2-5]

VASP is a first-principles based package that employs pseudopotentials and the projector-augmented wave (PAW) basis set to represent the electrons, therefore the electron density is independent of atomic positions. This makes structural optimizations and total energy calculations relatively easy to converge. The Bloch description of the PAW pseudopotentials keeps the accuracy of valence electron wavefunction behavior allowing for pseudopotentials to be analyzed based on an orbital description in a way that is familiar to chemists. The key operations used in VASP have been total energy calculations with and without spin polarization, structural optimizations with and without spin polarization, and the ability to determine electron localization through graphical representation.

Synthetic Materials and Methods

Starting materials

High purity starting materials used for synthetic reactions are listed in Table 2.1. All starting materials were stored in air at room temperature as pieces or ingots.

Table 2.1 Starting materials used for all synthetic work. (purity of individual elements is provided as a ratio based on other metallic elements)

Element	Source	Melting point (K)	Purity (%)	Form	Appearance
Mn	MPC-Ames Lab	1518.15	99.99	Chunks	grayish
Zn	Alfa-Aesar	692.73	99.999	Tear drops	Lustrous, gray
Al	MPC-Ames Lab	933.52	99.9999	Tear drops	Med. Luster gray
Purity of a specific element as a ratio based on other metallic elements.					

Special techniques and containers.

Surface oxides were removed from Mn by a dilute HNO3 bath followed by ethanol rinse and drying under vacuum, then a heat treatment with max temperature of 800 °C in an evacuated fused silica jacket. Cleaning was required for Ta ampoules, as they were cut from bulk tubing. The Ta ampoules were formed by cutting 1cm diameter Ta tubing into 3-inch lengths and cleaning in a mixed acid bath (HF and HNO3 and Aqua Regia), crimped and arc welded into shape under an argon atmosphere. To be most effective in the synthetic process, side reactions with sample containers must be minimized. Reactivity, heat resistance, cost and reactivity were considered in the choices for vessels. Alumina crucibles had a limit of 1273 K before reactions with Al or germanium were risked. Tantalum ampoules had a limit of 1123 K before reactions with Mn would begin. Silica reacts readily with Mn2O3 as well as Al at temperatures under maximum temperatures used in experimental heating schemes and for this purpose was used as a secondary container only.

Tube furnaces.

Samples were synthesized by either, using stoichiometric ratios of all constituent elements, or stoichiometric ratios of two of three elements and an excess of the third. The weighed elements were encapsulated in tantalum ampoules under an argon atmosphere for the first case, and alumina crucibles (Canfield crucibles) and surrounded by quartz wool for the latter case. These primary containers were then sealed in fused silica jackets under vacuum, approximately 10-5 torr, and then heated using a tube furnace. Each tube furnace was programmable with a temperature limit of 1373 K. and monitored by a thermocouple. Each sample had a controlled rate of heating and cooling.

For the samples with excess proportion of the third element the vessel was inverted and centrifuged immediately after removal from a tube furnace. Samples loaded with stoichiometric ratios of all elements were allowed to slowly cool to room temperature in the tube furnaces to allow optimal crystal growth.

Characterization Techniques and Analysis

Powder x-ray diffraction analysis.

A first step in characterizing samples was via Powder X-Ray Diffraction (PXRD). The 3D reciprocal space studied in SCXRD is projected onto 1D by taking the average of all oriented results. Although less information can be gathered through PXRD than by SCXRD it is still useful in its ability to identify phases in bulk material, as well as giving qualitative information about crystalline quality through analysis of peak widths and relative intensities. After heat treatment, if samples were brittle enough to immediately be ground, a fine powder would be used for PXRD. If samples were ductile, a file was used to generate a fine powder for PXRD. Both sample types were measured using a Stoe Stadii P diffractometer utilizing transmission geometry with a Cu Kα1 ($\lambda = 1.540598$ Å) radiation source. The reflections captured in each diffractogram were compared against theoretical powder patterns generated by single crystals selected from the same sample, and to theoretical powder patterns from the ICSD. Lattice parameters were determined by Werner indexing in the WinXPOW software package [6].

Single crystal x-ray diffraction analysis.

Important structural information was obtained through Single Crystal X-Ray Diffraction (SCXRD). Single crystals were selected from bulk samples using an optical microscope and glued to a glass thread using clear nail polish. Once data were collected, the structures were refined using the SHELXTL program. The diffractometer used to collect the

following data was a Bruker SMART APEX II CCD. An entire sphere or reciprocal space in increments was collected with an exposure time between 10 and 25 seconds for each frame depending on intensity of scattering. The data were analyzed using the SHELXTL program. Absorption corrections were made using semi-empirical means [7-10].

Scanning electron microscopy.

A Scanning Electron Microscope (SEM) equipped with an energy dispersive X-ray spectrophotometer (EDX-s) was employed to determine bulk compositions for both chunks and single crystals. SEM produces images by using a focused bean of electrons that interact with the electrons on the surface on the sample which produces signals which when detected contain information about composition and topography. Single crystal samples were picked, then attached to carbon tape using glass thread. Bulk samples were polished before analysis. The benefit of SEM has been a corroboration of phase compositions in samples with multiple mixed sites. Multiple points were examined on each specimen.

Physical Property Measurements

Magnetic Susceptibility Measurements.

Magnetic measurements on powder and pieces of samples were collected using a Quantum design MPMS SQUID magnetometer. The SQUID measures at temperatures in the range of 1.8-400K and in applied fields up to 70 KOe. Fitting the maximum dM/dT of magnetization versus temperature allowed for an approximation of the Curie temperature. The data collected was plot according to the Curie-Weiss law as χ^{-1} against temperature. The linear region of this plot, the paramagnetic region, the effective magnetic moments and Weiss temperature were determined.

Reference

[1] Jepsen, O.; Andersen, O.K. TB-LMTO, version 47; Max-Planck-Institut für Festkörperforschung: Stuttgart, Germany, 2000

[2] (a) Kresse, G.; Hafner, J. Phys. Rev. B1993, 47, 558. (b) Kresse, G.; Hafner, J. Phys. Rev. B1994, 49, 14251.

[3] Kresse, G.; Furthmüller, J.Comput. Mat. Sci.1996, 6, 15
.
[4] Kresse, G.; Furthmüller, J. Phys. Rev. B1996, 54, 11169.

[5] Kresse, G.; Joubert, D. Phys. Rev. B.1999, 59, 1758.

[6] WinXPOW version 3.0.1.11, 2010, Darmstadt Germany

[7] Sheldrick, G. M. SADABS, University of Gottingen: Gottingen, Germany, 2001.

[8] Sheldrick, G. M. Acta Crystallogr. A2008, 64, 112

[9] SHELXTL, version 6.10, Bruker AXS Inc.: Madison, WI, 2000.

[10] Diamond, version 3.2; Crystal Impact: Bonn, Germany, 2010

CHAPTER 3: MIXED SITE OCCUPANCY IN THE Γ-BRASSES OF THE Mn–Zn SYSTEM

Γ-brasses in the Mn–Zn System: an Experimental and Computational Study

Stephanie Eveland[a,b*], Srinivasa Thiminaiah[b], Madalynn G. Marshall[a,c], Gordon Miller[a,b]

[a] Department of Chemistry, Iowa State University Ames, IA, USA 50011

[b] Ames Laboratory Ames, IA, USA 50011

[c] Louisiana State University Baton Rouge, LA, USA 70803

Abstract

The synthesis and characterization of Ni_2Zn_{11}-type γ-brasses with composition $Mn_{2+x}Zn_{11-x}$ ($x = 0.06–0.60$) are reported. The synthesis follows standard high temperature methods and characterization by single crystal X-ray diffraction (SCXRD) and powder X-ray Diffraction (PXRD) techniques as well as Energy Dispersive Spectroscopy (EDS). First principles electronic structure calculations showed preferential heteroatomic Mn–Zn bonding and repulsive effects of Zn–Zn $3d–3d$ orbital overlap that influence the metal atom distribution in the structure. Local bonding environments and the relationship of $Mn_{2+x}Zn_{11-x}$ to other γ-brasses containing $3d$ metals such as $PdCoZn_{11}$ and Ni_2Zn_{11} are discussed.

Introduction

Γ-brasses represent a family of complex intermetallic compounds derived from defect bcc packings of atoms whose space group is determined by the coloring or decoration of individual atomic sites. A connection between stability and chemical composition within the

γ-brass family was accomplished by Hume-Rothery's valence electron counting rules, noting that Cu_5Zn_8, Ag_5Zn_8, and Au_5Zn_8 ideally formed with 21 valence *s* and *p* electrons per 13 atoms in the formula unit. Mizutani assigned the γ-brasses into three groups according to their constituent elements: Group I γ-brasses have a monovalent noble metal with a polyvalent metal or metalloid with a well-defined valency; Group II γ-brasses have a partially filled 3*d* metal with a fully filled valence *d*-band element (Zn or Cd) or a trivalent metal such as Al; and Group III γ-brasses consist of cases that do not include transition metals. [1, 2] By definition, the monovalent component of group I γ-brasses contributes one electron and the other component(s) has/have an accepted valence electron count such as Al (three electrons) or Sn (four electrons).

Within Group III γ-brasses, elements from among non-transition metals combine such as $Li_{21}Si_5$, which can be described from a Hume-Rothery as well as a Zintl-Klemm perspective due to larger electronegativity differences between the constituent atoms. The unit cell of $Li_{21}Si_5$ can be divided into two different 26-atom clusters, $Li_{22}Si_4^{4+}$ and $Li_{20}Si_6^{4-}$, to satisfy a Zintl-Klemm valence electron counting scheme. $Li_{21}Si_5$ follows the conventional counting scheme for γ-brasses and falls close to the idealized ratio of 21/13 by assigning Li one electron and Si four electrons, which gives 41 valence *s* and *p* electrons per 26 atoms in the formula unit, and which satisfies a Hume-Rothery perspective. [3] However, for Group II γ-brasses, the number of valence electrons assigned to each element with a partially filled valence *d*-band remains controversial and the elements involved have similar electronegativities making a Zintl-Klemm description incompatible. Therefore, electronic structure calculations are necessary to provide insight into the factors affecting their structural stability.

In all three groups, γ-brasses can be described in terms of 26-atom clusters which are comprised of four concentric shells of symmetry equivalent atoms shown in Figure 3.1(a). Two tetrahedra with increasing radii, viz., an inner and an outer tetrahedron (IT and OT), a larger octahedron (OH), and a distorted cuboctahedron (CO) form the concentric shells of each cluster. The interatomic distances within each shell are not necessarily within reasonable bonding ranges for the specific components.

(a)   (b)
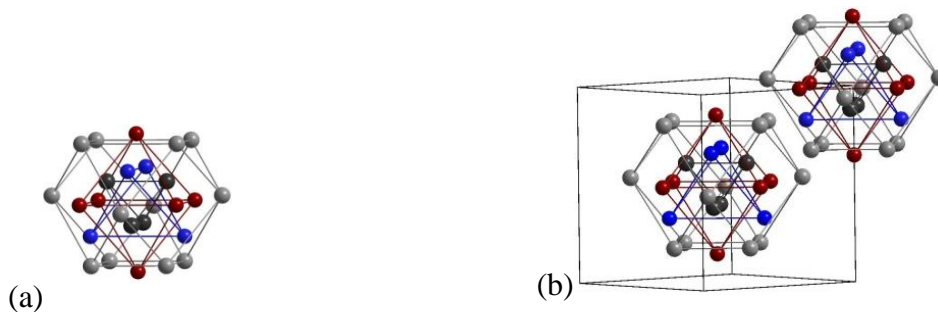
Figure 3.1 (a) 26-atom cluster from the $Mn_{2+x}Zn_{11-x}$ structure (b) two 26-atom clusters located at the corner and center of the cubic unit cell. Gray indicates a site fully occupied by Zn; Mn/Zn mixed sites are red for majority Zn and blue for majority Mn. Lines emphasize the different polyhedral shells (see text) and do not necessarily identify atom pairs within bonding distances. Image was generated via the Diamond Software package. [4]

The atomic decoration of these clusters can lead to lattice symmetries of rhombohedral in the case of Mn_5Al_8, body-centered cubic as observed for Cu_5Al_8 and Ni_2Zn_{11} (Figure 3.1(b)), or primitive cubic such as Cu_9Al_4. [1, 5, 6, 7] For group II γ-brasses, a series of Zn-rich structures have been reported along with their associated prototypical coloring, without a detailed atomic description of any Mn–Zn γ-brass. Among the transition metals small differences in electronegativity play a role in the formation of Hume-Rothery phases such as γ-brasses with mixed site occupancy.

The complexity of γ-brasses provides an excellent situation to study factors governing stability of complex structures through experimental and theoretical means. Previous work in the Cu-Zn, Ni-Zn, Pd-Zn, Pt-Zn, Co-Zn and Fe-Zn systems have all yielded cubic γ-

brasses. [8-11] In the Pt-Zn and Ni-Zn cases the earlier transition metal primarily, if not exclusively, occupies the OT site and, in the Pt-Zn case, vacancies are observed on the Zn-occupied IT site. Pd-Zn γ-brasses show mixing between Pd and Zn on the OH site whereas in the Cu-Zn case Cu occupies the OT and OH sites. In Fe-Zn γ-brasses two separate decorations are found: Fe_2Zn_{11} in the lower end of the phase width only the IT site is occupied by Fe; and in Fe_3Zn_{10} the Fe rich end of the phase width the OH site begins to host a mix of Fe and Zn. [8] Concerning Mn-containing brasses, it has been previously shown to form a rhombohedral γ-brass structure Mn_5Al_8. The structural dependence of Hume-Rothery phases on VEC suggests that Mn–Zn γ-brasses may form after systematic substitution of Zn for Al in Mn_5Al_8, thereby lowering the VEC from 24/13 e$^-$/f.u toward 21/13 e$^-$/f.u.

Research performed by Liang et al. while exploring the Mn-Ni-Zn ternary system via Powder X-Ray Diffraction (PXRD) and electron microscopy indicated the existence of a possible γ-brass with approximate composition Mn_5Zn_{21}. [9] It was posited that the atomic decoration would classify it as a $Fe_2(Fe_{0.5}Zn_{0.5})_2Zn_9$-type γ-brass based solely on PXRD refinements. In this aristotype the earlier transition metal (Fe) is located on the IT and OT shells of the 26-atom cluster. Data from Liang et al. shows space group I$\overline{4}$3m with 19.0 atomic % Mn, 81.0 atomic % Zn and a lattice parameter of 9.1605(9) Å. The bulk sample was analyzed by Energy Dispersive Spectroscopy (EDS), which determined significant $MnZn_3$ was also present in the product, although, when annealed for an additional 5 days at 350°C, the $MnZn_3$ phase disappeared. [9] In the following discussion, a more appropriate aristotype designation will be justified by Single Crystal X-Ray Diffraction (SCXRD).

The most recently published experimental phase diagram for the binary Mn–Zn system does not report this Mn_5Zn_{21} phase, although a $MnZn_4$ phase is included. In 1927, a

$MnZn_4$ phase with a transition at 292 °C was identified without any crystallographic data, and in 1971 the $MnZn_4$ phase was identified as a γ-brass type. The current experimental phase diagram provided by Okamoto shows a phase transition at 180° C and a second transition at 420 ° C, with both higher temperature phases described as γ-brasses. [13-18] The composition and temperature ranges of Okamato's diagram support the annealing temperature used by Liang et al. so that it can be surmised that the Mn_5Zn_{21} γ-brass is the $MnZn_4$ "ht1" phase referenced in Okamoto's phase diagram. The questions left after previous work are how does this phase fit into the series of Zn-rich γ-brasses, and what can be understood about local atomic environments. To answer these questions, SCXRD, EDXS, magnetic measurements, and first-principles electronic structure calculations are required.

Experimental Methods

Synthesis.

Mn chunks (99.99% Mn, 99.99% Zn teardrop, MPC, Ames Laboratory) were individually weighed for sample sizes of ca. 0.5 g, sealed under an Ar atmosphere in Ta ampoules, and encapsulated under vacuum in fused silica jackets. Samples with 15-30 atomic % Mn were loaded. All samples were heated at a rate of 1 °C per minute to a maximum temperature of 750 °C, cooled at approximately 0.1 - 0.3°C/min, then annealed at 350°C or 400°C for 2-8 days, followed by natural cooling to room temperature inside the furnace.

Phase analysis.

Once removed from the Ta ampoules, the samples were crushed into powder to be characterized by PXRD, and single crystals were selected to be analyzed by SCXRD. All SCXRD data were collected at room temperature, and any dependence of atomic site occupation on temperature was not investigated. Chunks from pure phase samples were

analyzed by EDS. For phase purity verification, all samples were characterized by PXRD using a Stoe Stadii P diffractometer utilizing transmission geometry and Cu $K_{\alpha 1}$ radiation. GSASII was employed for refinement of PXRD data from a sample loaded as $Mn_{2.33}Zn_{10.67}$ [19].

Structure determination.

Numerous single crystals selected from different loading compositions were studied using a Bruker Apex II CCD diffractometer equipped with graphite monochromatized Mo K_{α} radiation. The 2θ range collected extended from 3° to approximately 62°. All structural models discussed below were obtained from direct methods and refined by full matrix, least squares refinement on F^2 using the ShelXTL package. [20]

Scanning electron microscopy.

Energy Dispersive X-ray Spectroscopy was performed on chunks of material from a pure phase sample as determined by PXRD using an Oxford Aztec EDXS, to make an additional comparison of refined composition of SCXRD with the bulk sample.

Electronic structure calculations

The Tight-Binding Linear Muffin-Tin Orbital method using the Atomic Sphere Approximation

(TB-LMTO-ASA) The Stuttgart Tight-Binding Linear Muffin-Tin Orbital program using the Atomic Spheres Approximation (TB-LMTO-ASA) is a first principles computational method which was used to compute the electronic structures of two models from the experimentally determined structures of these Mn–Zn γ-brasses, "Mn_2Zn_{11}" and "Mn_3Zn_{10}" [21] This computational approach uses overlapping Wigner-seitz (WS) spheres surrounding each atom so that spherical basis functions, i.e., atomic orbital (AO)-like wavefunctions, are used to fill real space of the structure and keeping the WS sphere overlap

to be less than 16 percent. If necessary, any remaining space is accounted for by empty WS spheres, which was the case for the "Mn_2Zn_{11}" calculations. The percent overlap for "Mn_2Zn_{11}" was 9.113%, the Mn WS radius was 1.590 Å with a basis set which consisted of $4s/4p/3d$, and the Zn WS radius range was 1.464−1.545 Å with a basis set which consisted of $4s/4p/3d$. The percent overlap in "Mn_3Zn_{10}" was 9.118 %, the Mn WS radius was 1.550 Å and the Zn WS radius range was 1.50−1.56 Å and used the same basis set as "Mn_2Zn_{11}." A mesh of 91 k-points in the irreducible wedge of the first Brillouin zone was used to obtain all integrated values, including Density of States (DOS) and Crystal Orbital Hamiltonian Population (COHP) curves.

Additional calculations treating the Zn $3d$ orbitals as filled core orbitals were also attempted to examine the influence of these states on the electronic structure and bonding analysis. In these cases, the corresponding percent overlaps remain the same and the Zn basis set was $4s/4p/(3d)$; also, the "Mn_3Zn_{10}" WS radii remain the same but for "Mn_2Zn_{11}" the Mn WS radius became 1.584 Å and the Zn WS range became 1.462−1.542 Å. Experimental atomic positions derived from SCXRD were used as structural input to produce the electronic density of states (DOS) and crystal orbital Hamilton population (COHP) curves, and total energies

Results and Discussion

The sample used for the PXRD pattern shown in Figure 3.2 was loaded as "$Mn_{2.33}Zn_{10.67}$" and underwent an extended annealing treatment of 198 hrs at 400°C to minimize the presence of $MnZn_3$ and $Mn_{0.52}Zn_{0.48}$ [11]. The theoretical PXRD pattern peak intensities derived from single crystal refinement are consistent with those of the bulk sample. The experimental PXRD data shown in Figure 3.2 were refined in comparison to the

range of SCXRD refinements from the same sample using GSASII [19]. Refinement of thermal parameter, lattice constant, and site occupation factors from the PXRD pattern showed a larger lattice parameter than from SCXRD, insignificant differences in the thermal parameters, and a strong preference for Zn on the OH and Mn on the OT sites. See Supporting Information for more information. Although the PXRD yields good agreement between the γ-brass structure of the bulk sample and individual single crystals picked for SCXRD refinement, the question of phase width and site occupancy must be investigated using electronic structure calculations.
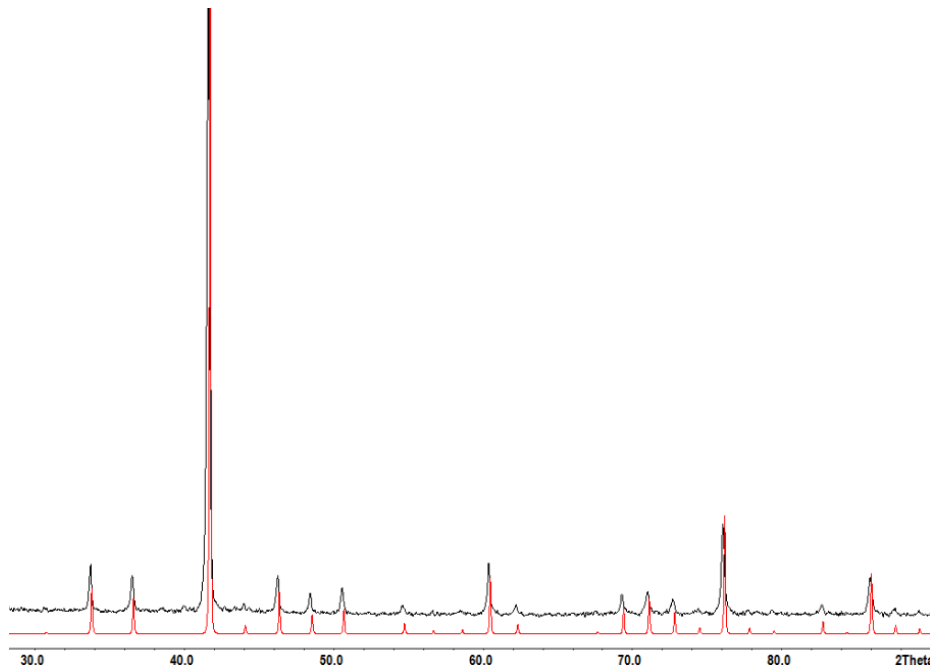
Figure 3.2: Theoretical ($Mn_{2.50}Zn_{10.50}$) and experimental ($Mn_{2.33}Zn_{10.67}$) PXRD patterns. Red shows the theoretical pattern derived from single crystal refinement $Mn_{2.50}Zn_{10.50}$ and generated using WinXPOW software package from the bulk sample loaded as $Mn_{2.33}Zn_{10.67}$ represented by the black PXRD pattern. [22]

The individual compositions found in other elemental mixtures with alternative heating schemes (50 hrs at 400°C, or two-step cooling for 48 hours at 400°C then annealed for 150 hr at 350°C) are listed in Table 3.2.3, as well as any secondary phases indicated by PXRD analysis.

Table 3.1: Compositions of $Mn_{2+x}Zn_{11-x}$ (SCXRD & PXRD)

Refined comp.	Loaded comp.	Refined e/a	Lattice parameters Å	S.G.	Secondary phases in PXRD
$Mn_{2.06(3)}Zn_{10.94}$	$Mn_{3.00}Zn_{10.00}$	1.683	a= 9.172(4)	$I\bar{4}3m$	β-Mn
$Mn_{2.20(1)}Zn_{10.80}$	$Mn_{2.33}Zn_{10.67}$	1.662	a= 9.161(7)	$I\bar{4}3m$	$Mn_{0.52}Zn_{0.48}$, Mn_2Ta
$Mn_{2.33(1)}Zn_{10.67}$	$Mn_{2.33}Zn_{10.67}$	1.642	a= 9.155(2)	$I\bar{4}3m$	$Mn_{0.52}Zn_{0.48}$
$Mn_{2.50(2)}Zn_{10.50}$	$Mn_{3.00}Zn_{10.00}$	1.615	a=9.177(2)	$I\bar{4}3m$	Mn_2Ta (trace)
$Mn_{2.54(1)}Zn_{10.46}$	$Mn_{3.00}Zn_{10.00}$	1.609	a =9.16(2)	$I\bar{4}3m$	β-Mn
$Mn_{2.60(7)}Zn_{10.4}$	$Mn_{3.00}Zn_{2.00}$	1.600	a=9.172(2)	$I\bar{4}3m$	$Mn_{0.52}Zn_{0.48}$ (majority)

*The refined composition is given by SCXRD, as are the lattice parameters. Samples from row 1 and 5 were picked from the same bulk material. Samples from rows 2 and 3 were picked from the same bulk material. The Mn_2Ta was manually separated from the bulk $Mn_{2.50}Zn_{10.50}$ by visually inspecting the macroscopic morphology of chunks under microscope.

Mn_2Ta was found in varying quantities in samples where some crystals were found growing on the sides of the Ta ampoule. The SCXRD refinement shown in Table 3.1 indicates a phase width of 15.8-20.0 atomic % Mn, which is in agreement with the suggested $MnZn_4$ phase width in Okamoto's phase diagram. [10]

Table 3.2: Site composition by polyhedral shell

Composition	IT		OT		OH		CO	
	%Mn	%Zn	%Mn	%Zn	%Mn	%Zn	%Mn	%Zn
$Mn_{2.06(3)}Zn_{10.94}$	0	100	72.0(3)	28.0	21.0(3)	79.0	0	100
$Mn_{2.20(1)}Zn_{10.80}$	0	100	78.8(2)	21.2	20.8(2)	79.2	0	100
$Mn_{2.33(2)}Zn_{10.67}$	0	100	82.0(5)	18.0	23.0(5)	77.0	0	100
$Mn_{2.50(1)}Zn_{10.50}$	0	100	81.68(5)	18.3	28.67(4)	71.3	0	100
$Mn_{2.54(1)}Zn_{10.46}$	0	100	85.0(3)	15.0	28.0(3)	72.0	0	100
$Mn_{2.60(2)}Zn_{10.40}$	0	100	83.9(2)	16.1	31.0(2)	69.0	0	100

*Compositions of Mn and Zn were determined by SCXRD

The body-centered unit cell of γ-brass can be broken down into two identical 26-atom clusters and further understood by examining the composition of the cluster's four concentric

shells (see Figure 3). The coloring or arrangement of each element on these shells determines the type of γ-brass. Table 3.2 shows the IT shell is solely occupied by Zn, whereas the OT shell is mixed occupied with majority Mn for all single crystals examined. The OH shell also shows mixed occupation between Mn and Zn, but with Mn as the minority component. The fourth shell, the CO, is fully occupied by Zn.

Structural trends and valence electron counting

By taking a closer look at trends in connectivity across $3d$ metal-containing γ-brasses, this system can be more accurately described. Other γ-brasses with similar atomic arrangements favor the lower valence electron metal to be located on the OT sites, whereas some show mixing on the OH sites, although $Mn_{2+x}Zn_{11-x}$ shows both with uneven mixing of the OT and OH sites between the lower valence electron metal (Mn) and the higher valence electron metal (Zn). Many, like Cu_5Zn_8, show the OT and OH sites fully occupied at stoichiometric refinements by the lower valence electron element. [1] For Cu_5Zn_8-types that show mixing, it is generally reported as uniform mixing on those sites, such as the Li-Ag system where 80-93% of the mixed sites are occupied by Li throughout its phase range.[23] Figure 3.3 depicts differences in coloring schemes of the Li-Ag γ-brass 26-atom cluster shown in Figure 3(a) and the 26-atom cluster of $Mn_{2+x}Zn_{11-x}$ shown in 3(b).

(a)   (b)
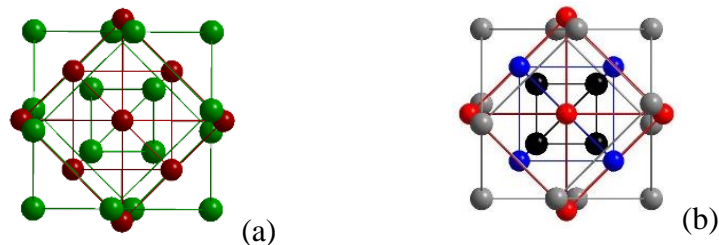
Figure 3.3: (a) $Li_{18}Ag_8$ 26-atom cluster where green indicates Ag and red indicates Li (b) $Mn_{2+x}Zn_{11-x}$ 26-atom cluster, where shades of grey indicates Zn, and red indicates a majority Zn occupied mixed site while darker blue indicates a majority Mn mixed site.

For γ-brasses containing one or more 3d metals, the general convention for determining the number of valence electrons is to count s and p electrons but not valence d electrons. For metals such as Cu, Ag, Au, Zn, and Cd the valence d orbitals are filled. In general, this convention leads to Ni and earlier transition metals contributing zero electrons to the e/a ratio. Although this convention works well for late transition and post transition metals, intermetallic compounds such as CrGa and MnGa at $e/a = 1.5$ do not fit well into the ideal e/a ratio for rhombohedral γ-brasses. [23, 24]

Table 3.3: Structural Trends Across the γ-Brasses

	$Mn_{2+x}Zn_{11-x}$	Cu_9Al_4	Cu_5Zn_8	Ni_2Zn_{11}	$CoPdZn_{11}$	Fe_3Zn_{10}	Mn_5Al_8
S.G.	$I\bar{4}3m$	$P\bar{4}3m$	$I\bar{4}3m$	$I\bar{4}3m$	$I\bar{4}3m$	$I\bar{4}3m$	R3m
Type	Ni_2Zn_{11}	Cu_9Al_4	Cu_5Zn_8	Ni_2Zn_{11}	Ni_2Zn_{11}	$Fe_2(Fe_{0.5}Zn_{0.5})_2Zn_9$	Cr_5Al_8
Phase Width	14-23 % Mn	65-68 % Cu	30-42 % Cu	16-27 % Ni	16-27 % Co/Pd	24-32 % Fe	33-50 % Mn
VEC*	1.611	1.615	1.615	1.692	1.692	1.538	1.846
ref.		[7]	[1]	[6]	[11]	[6, 8]	[25]

*The VEC is calculated based on stoichiometric compositions of the prototypical colorings shown in row 2.

I-centered, P-centered, and F-centered γ-brasses will have a closer to ideal e/a ratio of 1.63 as seen in Table 3 than those with rhombohedral packings, which tend to see e/a ratios closer to 1.8 than 1.6. [24] For stoichiometric "Mn_2Zn_{11}" and "Mn_3Zn_{10}", the e/a ratios are 1.69 and 1.53, respectively. The range of compositions observed, $Mn_{2.06}Zn_{10.94}$–$Mn_{2.60}Zn_{10.40}$, has an e/a ratio range of 1.60–1.68, which is in line with the 21/13 ideal ratio for I-centered γ-brasses. The composition range for Mn in $Mn_{2+x}Zn_{11-x}$ extends from approximately 15.8 to 20.0 %, which is most similar to Ni_2Zn_{11} and $CoPdZn_{11}$. On the other hand, the Fe_3Zn_{10} aristotype proposed by Liang et al. has a considerably higher content of the minority component (Mn) concentrated on the IT and OT shells. [6]

And, although the space group, minority component locations, and e/a ratios of $Mn_{2+x}Zn_{11-x}$ are similar to the Cu_5Zn_8 γ-brass, the composition ranges are drastically different with Cu comprising 30-42% of phase, further Supporting the Ni_2Zn_{11} coloring prototype discussed above. [1]

Previous work in the Co-Pd-Zn γ-brasses has shown that systematic vacancies occur for $Co_{2+x}Zn_{11-y}\square_{y-x}$; the data presented in this body of work indicates no vacancies in the Mn–Zn γ-brass system. Multiple attempts to refine single crystal data by incorporating vacancies were undertaken, but this strategy produced either instabilities for Zn-rich refinements and no observable vacancies (within standard error) for Mn-rich refinements. EDS was performed on a specimen determined to be phase pure by PXRD after manual separation of Mn_2Ta from the bulk powder. This chunk was isolated from a single crystal, which was refined by SCXRD to $Mn_{2.50(1)}Zn_{10.50}$. The refined composition by SCXRD matches well with that of EDS, 18.4-19.3 atomic % Mn from EDS and 19.2 atomic % Mn from refinement by SCXRD. The comparison of EDS and SCXRD support the compositions determined by SCXRD refinements and reinforces the conclusion that electron density assigned to a mixed Mn/Zn site is not Zn atoms with vacancies, as is seen in other ternary transition metal γ-brasses such as $CoPdZn_{11}$. [11]

In comparison to stoichiometric Co_2Zn_{11}, atomic distributions in the structures of $Mn_{2+x}Zn_{11-x}$ are similar because Zn occupies the IT and CO sites and is the majority component of the OH sites. [11] However, in $Co_{2+x}Zn_{11-y}\square_{y-x}$ vacancies appear on the IT site, whereas in $Mn_{2+x}Zn_{11-x}$ all SCXRD refinements indicate 100% occupancy of Zn at the IT site. When Pd is incorporated into Co_2Zn_{11}, a similar site occupation scheme to what is observed in $Mn_{2+x}Zn_{11-x}$ occurs. In $Co_2Pd_2Zn_9$ the lower valence metal Co preferentially

occupies the OT shell while the slightly higher valence metal Pd preferentially occupies the OH site and the highest valence[1] electron metal, Zn, fully occupies the IT and CO sites. The results of electronic structure calculations of $Co_2Pd_2Zn_9$ show marked similarities to $Mn_{2+x}Zn_{11-x}$ as well regarding the location of pseudogaps near E_F and distribution of the minority component's valence d electrons. Dilute ferrimagnetism was discovered in the Co-Pd-Zn γ-brasses and similarities in structure and composition range warrant an investigation into magnetic behavior, however results on the sample "$Mn_{2.50(1)}Zn_{10.50}$" remain inconclusive at this time. [11]

Due to the presence of Mn on both the OT and OH sites in $Mn_{2+x}Zn_{11-x}$, the Cu_5Zn_8-type γ-brass with major Mn deficiencies is a possible classification of these phases, although the composition and solubility of Mn into Ni_2Zn_{11} shown by Liang et al. make Ni_2Zn_{11} a better aristotype. [1, 9] Therefore, Mn–Zn γ-brasses can be written as a Ni_2Zn_{11}-type with additional mixing on the OH sites to accommodate the Mn-rich region of the phase width.

Electronic structure of $Mn_{2+x}Zn_{11-x}$

Complex intermetallic systems with mixed site occupation and experimentally determined phase widths present interesting challenges when investigating local atomic interactions using electronic structure calculations. One of the computational challenges includes choosing an appropriate coloring model. By combining the results of XRD, EDS, and appropriate models to generate computational data, a greater depth of knowledge is attained regarding the factors governing stability and local connectivity of complex compounds. Coloring models based on $Fe_2(Fe_{0.5}Zn_{0.5})_2Zn_9$ as suggested by Liang et al. would have more through-space Mn–Mn interactions than observed experimentally in $Mn_{2+x}Zn_{11-x}$ due to IT–IT connections and the probability of Mn–Mn contacts through IT and

mixed OT site interactions. [9] Due to the refined Mn/Zn mixing on the OT and OH sites,

two models were chosen to investigate using electronic structure calculations: "Mn_2Zn_{11}" has

OT positions exclusively occupied by Mn and no Mn–Mn orbital overlap; and "Mn_3Zn_{10}"

has OH sites occupied by Mn with Mn–Mn contacts. The lattice parameters for "Mn_2Zn_{11}"

were chosen from the $Mn_{2.06}Zn_{10.94}$ refinement and "Mn_3Zn_{10}" used the lattice parameters

from $Mn_{2.60}Zn_{10.40}$, as listed in Table 3.2.

In the following discussion all VECs are calculated using conventional methods

assigning zero valence *s* and *p* electrons to Mn and two valence *s* an *p* electrons to Zn.

Electron counts shown on the DOS and COHP curves include all valence electrons. In the

DOS and COHP curves of both "Mn_2Zn_{11}" and "Mn_3Zn_{10}", Mn 3*d*-bands display

prominently just above and just below the respective Fermi energies. In the DOS curve for

"Mn_2Zn_{11}" the Fermi energy (set to 0eV) falls on the upward slope of states that largely arise

from the Mn 3*d* orbitals. Just below the calculated Fermi energy of "Mn_2Zn_{11}", there is a

deep pseudogap.

Applying the rigid band model to the DOS and COHP curves allows an estimation of

electronic structure features at different electron counts, although, it is best applied to the

nearly-free electron portion and not the *d*-band because the full structures are subject to

considerable changes with composition (compare the DOS curves "Mn_2Zn_{11}" and Mn_3Zn_{10}"

in Figures 4 and 5). According to the RBM, the pseudogap extends from 145.5 e^-,

corresponding to "$Mn_{2.10}Zn_{10.89}$" and a VEC of 1.67 *e/a* to 144.7 e^-, corresponding to

"$Mn_{2.27}Zn_{10.73}$" and 1.65 *e/a*. The corresponding Mn–Zn and Zn–Zn COHP curves in Figure

3.4(b) indicate that Mn(OT)–Zn interactions become antibonding above the Fermi level for

"Mn_2Zn_{11}", whereas both are essentially nonbonding throughout the pseudogap region of the

DOS. Lowering the valence electron count below the pseudogap and VEC lower than 1.65

e/a would deplete significant Mn−Zn bonding states. Therefore, the combination of DOS

and COHP curves for "Mn$_2$Zn$_{11}$" indicates enhanced stability for Mn concentration

exceeding "Mn$_2$Zn$_{11}$", i.e., Mn$_{2+x}$Zn$_{11-x}$, but with an upper bound of x ~ 0.3 set by depleting

heteroatomic Mn−Zn bonding states in the DOS.
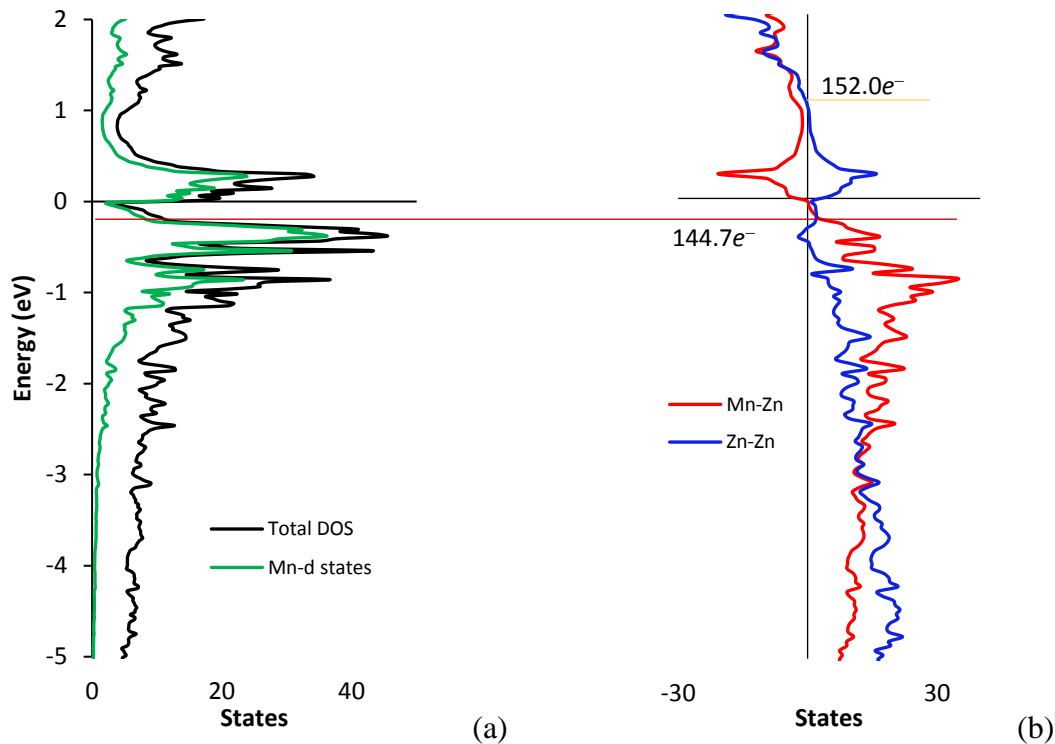
Figure 3.4: (a) Density of States "Mn$_2$Zn$_{11}$" (b) Crystal Orbital Hamilton Population curves of "Mn$_2$Zn$_{11}$". The gray line indicating 152.0 e^- shows the point at which Zn−Zn interactions become antibonding when the Zn3d − band is formally filled at 130e$^-$ leaving 22e$^-$ remaining.

On the other hand, the DOS curve for "Mn$_3$Zn$_{10}$" in Figure 3.5(a) shows multiple

narrow pseudogaps within a few tenths of eVs from the calculated Fermi level arising from

ligand field splitting of the Mn 3*d* orbitals from through-space Mn−Mn contacts, and a broad

(~0.6 eV wide) pseudogap near +1eV relative to E_F for "Mn$_3$Zn$_{10}$". In this broad pseudogap,

the Mn−Mn, Mn−Zn, and Zn−Zn COHP curves in Figure 3.5(b) show nonbonding

interactions. Above this broad pseudogap at 151.8 e^-, or "Mn$_{0.85}$Zn$_{12.15}$" and a VEC of 1.87

e/a, Zn−Zn interactions become strongly antibonding. The Mn−Zn interactions are antibonding above 141.8 e⁻ (indicated by the yellow line in Figure 3.5b) which corresponds to the composition of "$Mn_{2.65}Zn_{10.65}$" and a VEC of 1.64 *e/a*. and can be assigned as the theoretical upper bound for Mn of these binary Mn−Zn γ-brasses. As a result of the DOS and COHP analyses for "Mn_2Zn_{11}" (Mn on OT sites) and "Mn_3Zn_{10}" (Mn on OH sites), optimized metal-metal bonding occurs for a range of compositions $Mn_{2+x}Zn_{11−x}$.
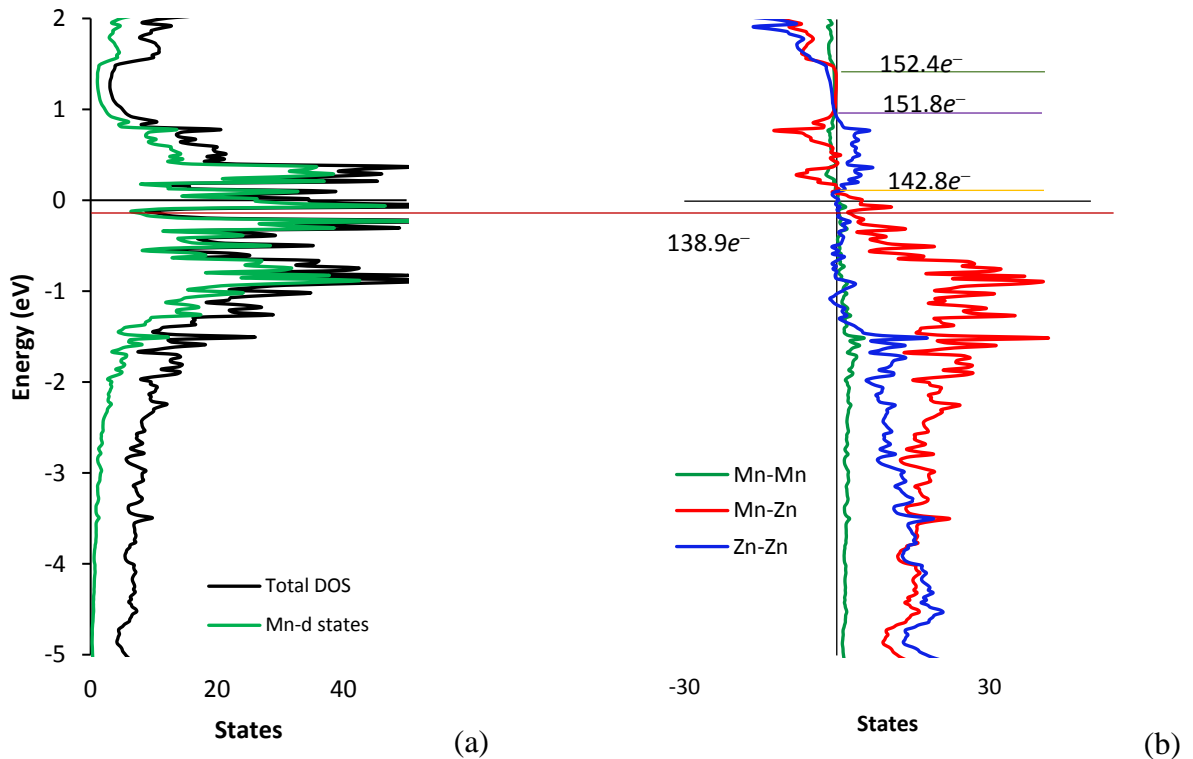
Figure 3.5: (a) Density of States of "Mn_3Zn_{10}" (b) Crystal Orbital Hamilton Population curves for "Mn_3Zn_{10}". The dark red line indicates the minima of a pseudo gap occurring at 138.9 e^- which corresponds to $Mn_{3.42}Zn_{9.58}$ which corresponds to a VEC of 1.47 *e/a*. The yellow line indicates the point at which Mn−Zn interactions become antibonding and corresponds to a composition of $Mn_{2.65}Zn_{10.35}$. For electron counts near 152.0 e^-, all interactions are nonbonding.

The experimental result gives 0.06(3) ≤ *x* ≤ 0.60(1); and the computational predictions are 0.10 ≤ *x* ≤ 0.27 from "Mn_2Zn_{11}" and 0.65 ≤ *x* ≤ 1.00 from "Mn_3Zn_{10}". The Mn_2Zn_{11} model was constructed to treat Zn rich side of phase width and the Mn_3Zn_{10} model

was constructed to highlight the Mn rich end of the phase width. Taking these computational results together a reasonable predicted phase width would be $0.1 \leq x \leq 0.65$ as the "Mn_3Zn_{10}" model shows strongly antibonding Mn−Zn and Mn−Mn interactions as number of Mn interactions increase.

To determine differences in the capacity of an individual crystallographic site to accommodate more or less electrons, the integrated density of states was evaluated for each site using "Mn_2Zn_{11}" and "Mn_3Zn_{10}" in Table 3.4.

Table 3.4: Integrated Density of States for each crystallographic site in "Mn_2Zn_{11}" (Mn on OT sites) and "Mn_3Zn_{10}" (Mn on OH sites)

	"Mn_2Zn_{11}"		"Mn_3Zn_{10}"	
	ΔNo. e^-	Element	ΔNo. e^-	Element
IT	+0.0282	Zn	+0.0447	Zn
OT	−0.1159	Mn	−0.0193	Zn
OH	−0.0223	Zn	+0.0130	Mn
CO	+0.0279	Zn	−0.0150	Zn
Comp. at E_F	$Mn_{2.02}Zn_{10.98}$		$Mn_{3.02}Zn_{9.98}$	

In each case, we focus on the Zn sites to identify likely substitution patterns of Mn for Zn. Since Mn has fewer $3d$ valence electrons than Zn, then Mn will preferentially substitute for Zn atoms in the site(s) that achieve(s) the lowest integrated DOS. For "Mn_2Zn_{11}" with Zn atoms in IT, OH, and CO sites, the lowest population occurs at the OH sites; for "Mn_3Zn_{10}" with Zn atoms in IT, OT, and CO sites, the lowest population occurs at the OT sites. Thus, the optimum site energies for $Mn_{2+x}Zn_{11-x}$ $(0.06(3) \leq x \leq 0.60(1))$ occur for Mn and Zn atoms sharing the OT and OH sites, with more Mn on the OT sites than OH sites, in agreement with experiment.

The metallic radii of Mn and Zn are respectively 1.27 Å and 1.34 Å, so interatomic distances between 2.5 Å and 3.0 Å are considered potential Mn−Mn, Mn−Zn, and Zn−Zn

bonding interactions. To assess the relative strengths of polar-covalency of the metal-metal

bonds in $Mn_{2+x}Zn_{11-x}$, integrated COHP values for states populated up to the Fermi energy

are utilized for the following bonding analysis.

Detailed description of individual environments and connectivity can be found in the

Supporting Information. Tables 3.5 and 3.6 show that the strongest bonding interactions for

the 26-atom clusters involve heteroatomic Mn−Zn contacts except for the OH−OH contact in

"Mn_3Zn_{10}", which is a Mn−Mn interaction through the faces and edges of the unit cell.

Table 3.5: Mn_2Zn_{11} Bonding Analysis

Bond Type	Element Type	Distance Å	Mult.	ICOHP (eV) / Contact	ICOHP (eV) / Contact *
IT−IT	Zn−Zn	2.84	12	0.360	0.554
IT−OT	Zn−Mn	2.70	24	0.472	1.078
IT−OH	Zn−Zn	2.66	24	−0.267	0.964
IT−CO	Zn−Zn	2.70	24	0.138	0.856
OT−OH	Mn−Zn	2.79	24	0.556	1.033
OT−CO	Mn−Zn	2.63	24	0.905	1.448
OT−CO	Mn−Zn	2.68	24		
OH−OH	Zn−Zn	2.66	6	−0.088	1.235
OH−CO	Zn−Zn	2.64	24	0.083	1.079
OH−CO	Zn−Zn	2.90	48	0.210	0.514
OH−CO	Zn−Zn	2.96	24		
CO−CO	Zn−Zn	2.73	48	0.304	0.719

* (Zn $3d$ orbitals excluded)

Table 3.5 shows the IT−OH and OH−OH interactions are antibonding in "Mn_2Zn_{11}"

and the 48 OT−CO connections exhibit the strongest polar-covalency. OT sites make no

contacts with other OT sites so that there are no through-space Mn−Mn contacts in

"Mn_2Zn_{11}," whereas in the refined $Mn_{2.06}Zn_{10.94}$, the probability of Mn−Mn contacts would

be closer to 1.2% of all contacts, or 3.6 potential Mn−Mn interactions for OT−OH contacts.

In $Mn_{2.60}Zn_{10.40}$ the probability of Mn−Mn contacts would be 2.2% with 6.8 potential

contacts per unit cell, although "Mn_3Zn_{10}" shows only six Mn−Mn contacts, representing

3.1% of all bonding interactions. On scaling the number of interactions from $Mn_{2.60}Zn_{10.40}$ to

$Mn_{3.00}Zn_{10.00}$, there would be far more than 6 potential Mn−Mn contacts per unit cell in

"Mn_3Zn_{10}". Therefore, the Mn−Mn contacts shown in Figure 3.5(b) may be

underrepresenting their role in the physical system.

Table 3.6: Mn_3Zn_{10} Bonding Analysis

Bond Type	Elements	Distance (Å)	Mult.	ICOHP (eV) / Contact	ICOHP (eV) / Contact*
IT –IT	Zn–Zn	2.85	12	0.021	0.554
IT –OT	Zn–Zn	2.71	24	−0.237	0.834
IT –OH	Zn–Mn	2.66	24	0.477	1.155
IT –CO	Zn–Zn	2.70	24	0.061	0.934
OT –OH	Zn–Mn	2.79	24	0.472	0.899
OT –CO	Zn–Zn	2.63	24	−0.174	0.999
OT –CO	Zn–Zn	2.68	24		
OH –OH	Mn–Mn	2.67	6	1.146	2.201
OH –CO	Mn–Zn	2.65	24	0.787	1.472
OH –CO	Mn–Zn	2.90	48	0.663	0.841
OH –CO	Mn–Zn	2.97	24		
CO –CO	Zn–Zn	2.74	48	0.251	0.880

*(Zn 3d orbitals excluded)

Table 3.6 shows the IT−OT and OT−CO interactions are antibonding in "Mn_3Zn_{10}"

and the six Mn−Mn OH−OH connections are the strongest individual bonds. For a

comparison to experimental bonding schemes by element see Supporting Information. The

3d orbitals of Zn, which appear in the DOS approximately 7 eV below the Fermi energy, are

formally filled. In this region the COHP is strongly affected by the 3d-3d repulsions. When

Zn 3d orbitals are treated as core orbitals, all "Mn_2Zn_{11}" and "Mn_3Zn_{10}" contacts are

evaluated as bonding by ICOHP. Table 3.5 shows that for "Mn_2Zn_{11}" the Mn−Zn

interactions increased the most drastically from 0.64 to 1.19 eV per bond on average and the Zn−Zn bonds became more positive by an average of 0.74 eV per bond. The 48 OT−CO bonds remain the strongest individual interactions. As seen in Table 5, excluding the Zn 3d orbitals drastically increased the ICOHP for Mn−Zn interactions in "Mn_3Zn_{10}" from 0.60 to 1.09 eV per bond on average with the OT−CO interactions increasing the most significantly. Zn−Zn interactions also became more bonding by an average of 0.86 eV per bond when Zn 3d orbitals were excluded.

Conclusion.

Computation and experiment work synergistically to reveal details previously unreported in the γ-brasses of the Mn−Zn system. The Mn−Zn γ-brasses are observed to have a phase width of $Mn_{2+x}Zn_{11-x}$ (x = 0.06-0.60) and the distribution of Mn and Zn atoms most similarly mimics $CoPdZn_{11}$ with a composition range most like Ni_2Zn_{11}. Site energy analysis, electronic structure, and SCXRD support mixed occupation of the OT and OH sites with Zn preferentially occupying the OH and Mn preferentially occupying the OT sites. Results show that minimizing Zn−Zn homoatomic interactions has a stabilizing effect on the structure below the Fermi energy, although the first states populated above the Fermi energy are Mn−Zn antibonding and Zn−Zn bonding states which suggests that a phase width of $Mn_{2.06}Zn_{10.94}$-$Mn_{2.65}Zn_{10.35}$ may be possible before Mn−Zn interactions become strongly antibonding. This suggested phase width matches closely to the phase width observed experimentally. The role of Zn 3d orbitals is most felt in the Zn−Zn OH−OH interactions in "Mn_2Zn_{11}" and the Zn−Zn connections involving the OT sites in "Mn_3Zn_{10}". The observed mixed occupation on OT and OH sites dampens the intensity of the Zn−Zn 3d−3d interactions while promoting strong Mn−Mn and Mn−Zn bonds.

References

[1] A. F. Phragmen and G. Westgren, "X-Ray Studies on Alloys," *Metallwirtschaft,* pp. 380-385, 1929.

[2] U. Mizutani, Hume-Rothery Rules for Structurally Complex Alloy Phases, Boca Raton: CRC Press, 2011.

[3] H.-G. von Schnering and R. Nesper, "Li21Si5 Hume Rothery and Zintl," *Journal of Solid State Chemistry,* pp. 47-52, 1987.

[4] K. Brandenburg, "Diamond version 3.2k," Crystal Impact GbR, Bonn Germany, 2015.

[5] M. Ellner, "The Structure of the High-Temperature Phase MnAl(h) and the Displacive Transformation from MnAl(h) into Mn5Al8," *Metall. Trans. A,* vol. 21, pp. 1669-1672, 1990.

[6] A. Johansson, H. Ljung and S. Westman, "X-Ray and Neutron Diffraction Studies on gamma-Ni, Zn and gamma-Fe. Zn," *Acta Chemica Scandinavica,* vol. 22, pp. 2743-2753, 1968.

[7] L. Arnberg and S. Westman, "Crystal perfection in a non-centrosymmetric alloy. Refinement and test of twinning of the gamma-Cu9 Al4 structure," *Acta Crystallographica A (1978), 34, 399-404,* vol. 34, pp. 399-404, 1974.

[8] X. Weiwe, L. Jing, V. Pecharsky and G. J. Miller, "Gamma brasses with spontaneous Magnetization: Atom site preferences and Magnetism in the Fe-Zn and Fe-Pd-Zn Phase Spaces," *Zeitschrift fuer Anorganische und Allgemeine Chemie,* vol. 641, no. 2, pp. 270-278, 2015.

[9] J. Liang, Y. Du, C. Liao, Y. yuan Tang, L. qin Nong, F. Zheng and H. Xu, "Experimental investigation on the phase equilibria of the Mn-Ni-Zn System at 400C," *Journal of Alloys and Compounds,* vol. 489, no. 2, pp. 362-368, 2010.

[10] H. Okamoto, L. Tanner and T. E. Massalski, "Mn–Zn (Manganese-Zinc)," *Binary Alloy Phase Diagrams, II Ed,* vol. 3, pp. 2625-2629, 1990.

[11] W. Xie and G. J. Miller, "New Co-Pd-Zn γ-Brasses with Dilute Ferrimagnetism and Co2Zn11 Revisited: Establishing the Synergism between Theory and Experiment.," *Chemistry of Materials Volume,* vol. 26, no. 8, pp. 2624-2634, 2014.

[12] O. Gourdon and G. J. Miller, "Intergrowth compounds in the Zn-rich Zn-Pd system toward 1D quasicrystal aproximants," *Chemistry of Materials,* vol. 18, no. 7, pp. 1848-1856, 2006.

[13] B. Harbrecht, S. Thimmaiah, M. Armbruster, C. Pietzonka and S. Lee, "Structure and properties of gamma-brass-type Pt2 Zn11-delta (0.2<delta<0.3)," *Zeitschrift fuer Anorganische und Allgemeine Chemie ,* no. 628, pp. 2744-2749, 2002.

[14] C. L. Ackerman, "Über das Zweistoffsystem Mangan-Zink," *Z. Metallkd.,* vol. 19, pp. 200-204, 1927.

[15] J. Schram, "Das System Mngan-Zink von 0 bis 50% Mn," *Z. Metallkd,* vol. 32, pp. 399-407, 1940.

[16] E. Wachtel and K. Tsuiplakis, "Mgnetische Eigenschaften zinkreicher Zink Mangan-Legierungen im festen und geschmolzenen Zustand," *Z. Metallkd.,* vol. 58, pp. 41-45, 1967.

[17] O. Romer and E. Wachtel, "Zum Aufbau der Systeme Zink-Mangan und Zink-Mangan-Aluminium," *Z. Metallkd,* vol. 62, pp. 820-825, 1971.

[18] Y. Nakagawa and T. Hori, "Phase diagrams of the Manganese-Zinc System," *Trans. Jpn Inst Met.,* vol. 13, pp. 167-170, 1972.

[19] SHELXTL, version 6.10, Madison, WI: Bruker AXS INC, 2000.

[20] WinXPOW, "version 3.0.0.11," Darmstadt Germany, 2010.

[21] T. Noritake, M. Aoki, S. Towata, T. Takeuchi and U. Mizutini, "Structre determination of structurally complex Ag36 Li64 gamma-brass," *Acta Crstallographica B,* vol. 63, no. 5, pp. 726-734, 2007.

[22] O. Gourdon and G. Miller, "Reinvestigation of the Ga Mn structure and theoretical studies of its electronic and magnetic properties," *Journal of Solid State Chemistry,* vol. 173, pp. 137-147, 2003.

[23] S. Thimmaiah, Z. Tener, T. N. Lamichhane, P. C. Canfield and G. J. Miller, "Crystal structure, homogeniety range and electronic structure of rhombohedral gamma-Mn5Al8," *Zeitschrift fuer Kristallographie-Crystalline Materials,* vol. 232, no. 7-9, pp. 601-610, 2017.

[24] J. B. Mann, T. L. Meek, E. T. Knight, J. F. Capitani and L. C. Allen, "Configuration Energies of the d-Block Elements," *J Am. Chem Soc.,* vol. 122, no. 21, pp. 5132-5137, 200

Appendix A: Charge Density Analysis

Introduction

There is a subtle difference in electronegativities between Mn and Zn based on the Pauling and Mulliken scales. Mn (1.55; 1.26) is slightly less electronegative than Zn (1.65; 1.51) and this suggests that small differences in charge should be investigated, however, according to Allen, the involvement of the d orbitals in Mn bonding produce a larger configuration energy than seen in Zn. [1]   Nevertheless, this intermetallic compound's metallic character should trump any significant charge transfer between Mn and Zn. Therefore, only differences in charge density between like atoms will be discussed.

Experimental Methods

The Vienna Ab-initio Simulation Package. [2-5]

VASP is a first-principles calculation method used in the following discussion. VASP uses pseudopotentials or projector augmented wave methods and a plane wave basis set to build the electronic structure. Electron densities are independent of crystallographic positions making it an ideal option for performing total energy calculations, structural optimizations, and charge density analyses. The Bloch description of PAW potentials is a more accurate method to describe the behavior of the valence electron waveforms allowing analysis based on an orbital description. Experimental atomic positions derived from SCXRD were used as input in determining the electron localization through charge analysis.

Discussion

Table A-1 shows the average charge for the IT, OT, OH and CO sites of "Mn_2Zn_{11}" and "Mn_3Zn_{10}." In "Mn_2Zn_{11}" the IT, OH, and CO sites could take more electronegative elements, however the draw for the OH site is approximately $1/10^{th}$ that of the other Zn occupied sites which supports the notion that Mn would be more likely to dope on the OH

site than the IT or CO sites. In "Mn$_3$Zn$_{10}$" the OT and CO sites could carry a less

electronegative element and the OH and IT sites could carry a more electronegative element.

Mn is more likely to dope into the OT site than the CO site in "Mn$_3$Zn$_{10}$."

Table A.1: Bader Analysis of local atomic charges of "Mn$_2$Zn$_{11}$" and "Mn$_3$Zn$_{10}$"

Model	Valence e$^-$/f.u.	IT	OT	OH	CO
Mn$_2$Zn$_{11}$	22	Zn: (+0.0282)	Mn: (-0.1159)	Zn: (+0.0028)	Zn: (+0.0279)
Mn$_3$Zn$_{10}$	20	Zn: (+0.0447)	Zn: (-0.0193)	Mn: (+0.0130)	Zn: (-0.0150)

Conclusion

A mixed site occupation on the OH site is supported in both charge density

calculations represented in Table A.1 as well as a preference for the IT site to be occupied by

the electron poor element.

References

[1] J. B. Mann, T. L. Meek, E. T. Knight, J. F. Capitani and L. C. Allen, "Configuration Energies of the d-Block Elements," *J Am. Chem Soc.,* vol. 122, no. 21, pp. 5132-5137, 2000.

[2] (a) Kresse, G.; Hafner, J. Phys. Rev. B1993, 47, 558. (b) Kresse, G.; Hafner, J. Phys. Rev. B1994, 49, 14251

[3] Kresse, G.; Furthmüller, J.Comput. Mat. Sci.1996, 6, 15.

[4] Kresse, G.; Furthmüller, J. Phys. Rev. B1996, 54, 11169.

[5] Kresse, G.; Joubert, D. Phys. Rev. B.1999, 59, 1758.

Appendix B: Magnetic Susceptibility Measurements

Introduction

Γ-brasses with transitions metals without full 3d bands have been shown to exhibit various types of magnetic ordering. The intrinsic magnetic properties of the five 3d electrons in Mn suggest that compounds with certain structures, and bonding relationships between constituent elements may show a range of magnetic behavior [1-5]. The γ-brasses of the MnGa system, computationally and experimentally indicate Mn sites dominate the magnetic behavior [2]. The structure of $CoPdZn_{11}$ is similar to the experimentally determined structure of $Mn_{2+x}Zn_{11-x}$.

In $CoPd\,Zn_{11}$ the unpaired electrons on the Co sites contribute to the magnetic moment resulting in paramagnetic and ferromagnetic moments. The similarity in DOS between $CoPdZn_{11}$ and $Mn_{2+x}Zn_{11-x}$ regarding the 3d states near the fermi energy suggest the Mn sites may behave in a similar manner as the Co sites [3]. In Fe_2Zn_{11} the Fe sites show ferromagnetism and ferrimagnetism as do many other group II γ-brasses, and as before the more electropositive element's 3d states are observed near the Fermi energy [4]. In the work performed by Thimmaiah et. al $Mn_{4.92}Al_{8.08(2)}$ showed evidence of a low temperature spin glass state, and the Mn 3d bands took 3p electrons from Al avoiding systematic vacancies [5]. All the previous work suggests that Mn sites in γ-brasses can exhibit some degree of magnetic ordering. Because of these trends a basic investigation of magnetic behavior is warranted.

Experimental methods

A magnetic Susceptibility measurement was performed on a pure phase powder sample loaded as $Mn_{3.00(1)}Zn_{10.00}$. The sample was analyzed using the Quantum Design VSM detection module for a temperature range of 2.00-350.41 K and at room temperature for an applied field of 0-5 KOe.

Discussion

The magnetization plot shows regions of linear relation between M and H with small regions of hysteresis between those linear regions. The average slope of the linear regions is the approximate magnetic susceptibility, $\chi_p = 1.125$ cm^3/g. The linear trend indicates paramagnetism or diamagnetism. The temperature dependent Magnetization indicates a possible magnetostructural transition approx. 200K and 50K.
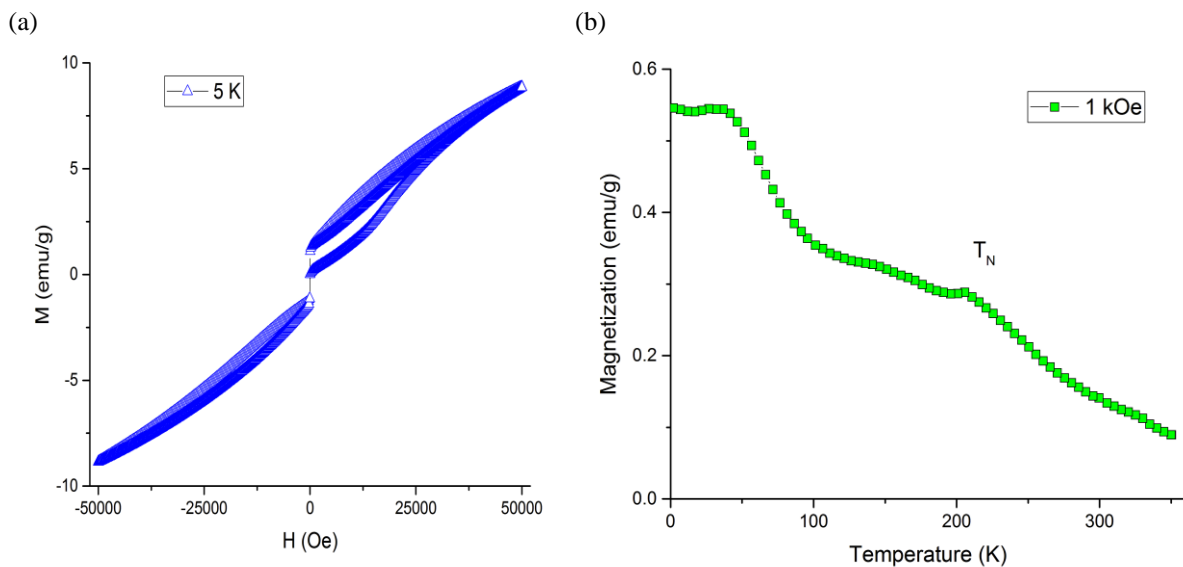
Figure B.1: Magnetic susceptibility of pure phase sample loaded as $Mn_{3.00(1)}Zn_{10.00}$ (a) The magnetization plot shows regions of linear relation between M and H. (b) Temperature dependent Magnetization.

Conclusion

Magnetic susceptibility measurements did not provide clear support of magnetic behavior for the $Mn_{3.00(1)}Zn_{10.00}$ sample. Further investigation of pure phase samples should be performed; however, no samples meet the phase purity standards required for such experimental measurement.

Acknowledgements

References

[1] O. Gourdon, S. Bud'ko, D. Williams and G. Miller, "Crystallographic, electronic and magnetic studies of zeta2-(Ga M) (M= Cr, Mn or Fe): trends in itinerant magnetism," *Inorganic Chemistry,* vol. 43, pp. 3210-3218, 2004.

[2] O. Gourdon and G. Miller, "Reinvestigation of the Ga Mn structure and theoretical studies of its electronic and magnetic properties," *Journal of Solid State Chemistry,* vol. 173, pp. 137-147, 2003.

[3] W. Xie and G. J. Miller, "New Co-Pd-Zn γ-Brasses with Dilute Ferrimagnetism and Co2Zn11 Revisited: Establishing the Synergism between Theory and Experiment.," *Chemistry of Materials Volume,* vol. 26, no. 8, pp. 2624-2634, 2014.

[4] S. Thimmaiah, Z. Tener, T. N. Lamichhane, P. C. Canfield and G. J. Miller, "Crystal structure, homogeniety range and electronic structure of rhombohedral gamma-Mn5Al8," *Zeitschrift fuer Kristallographie-Crystalline Materials,* vol. 232, no. 7-9, pp. 601-610, 2017.

[5] X. Weiwe, L. Jing, V. Pecharsky and G. J. Miller, "Gamma brasses with spontaneous Magnetization: Atom site preferences and Magnetism in the Fe-Zn and Fe-Pd-Zn Phase Spaces," *Zeitschrift fuer Anorganische und Allgemeine Chemie,* vol. 641, no. 2, pp. 270-278, 2015.

Supporting Information

Table SI1.1: $Mn_{2.06}Zn_{10.94}$ Crystallographic Data

Chemical formula	$Mn_{2.06}Zn_{10.94}$	
Formula weight	828.35	
Temperature	296(2) K	
Wavelength	0.71073 Å	
Crystal system	cubic	
Space group	I -4 3 m	
Unit cell dimensions	a = 9.172(4) Å	α = 90°
Volume	771.6(6) Å^3	
Z	4	
Density (calculated)	7.131 g/cm^3	
Absorption coefficient	36.463 mm^{-1}	
F(000)	1519	

Table SI1.2. Data collection and structure refinement for $Mn_{2.06}Zn_{10.94}$

Theta range for data collection	3.14 to 27.50°	
Index ranges	-11<=h<=11, -11<=k<=11, -11<=l<=11	
Reflections collected	3346	
Independent reflections	190 [R(int) = 0.0597]	
Coverage of independent reflections	100.0%	
Absorption correction	multi-scan	
Structure solution technique	direct methods	
Structure solution program	SHELXS-97 (Sheldrick, 2008)	
Refinement method	Full-matrix least-squares on F^2	
Refinement program	SHELXL-97 (Sheldrick, 2008)	
Function minimized	Σ w(F$_o^2$ - F$_c^2$)^2	
Data / restraints / parameters	190 / 0 / 20	
Goodness-of-fit on F^2	1.164	
Final R indices	177 data; I>2σ(I)	R1 = 0.0223, wR2 = 0.0492
	all data	R1 = 0.0252, wR2 = 0.0498
Weighting scheme	w=1/[σ^2(F$_o^2$)+(0.0227P)^2+1.1725P] where P=(F$_o^2$+2F$_c^2$)/3	
Absolute structure parameter	0.1(2)	
Largest diff. peak and hole	0.528 and -0.628 eÅ^{-3}	
R.M.S. deviation from mean	0.142 eÅ^{-3}	

Table SI1.3. Atomic coordinates and equivalent isotropic atomic displacement parameters (Å^2) for $Mn_{2.06}Zn_{10.94}$

U(eq) is defined as one third of the trace of the orthogonalized U$_{ij}$ tensor.				
	x/a	y/b	z/c	U(eq)
Zn1	0.89025(12)	0.8903(12)	0.8903(1)	0.0194(5)
Zn2	0.67267(13)	0.6727(1)	0.6727(1)	0.0127(8)
Mn2	0.67267(13)	0.6727(1)	0.6727(1)	0.0127(8)
Zn3	0.64586(14)	0.0	0.0	0.0151(6)
Mn3	0.64586(14)	0.0	0.0	0.0151(6)
Zn4	0.68860(10)	0.6886(1)	0.9631(1)	0.0207(3)

Table SI-4: $Mn_{2.20}Zn_{10.8}$ Crystallographic Data

Chemical formula	$Mn_{2.20}Zn_{10.8}$	
Formula weight	1653.73	
Temperature	296(2) K	
Wavelength	0.71073 Å	
Crystal system	cubic	
Space group	I -4 3 m	
Unit cell dimensions	a = 9.161(7) Å	α = 90°
Z	4	
Density (calculated)	7.143 g/cm3	
Absorption coefficient	36.381 mm-1	
F(000)	1516	

Table SI-5. Data collection and structure refinement for $Mn_{2.20}Zn_{10.8}$

Theta range for data collection	3.14 to 27.53°	
Index ranges	-11<=h<=11, -11<=k<=11, -11<=l<=11	
Reflections collected	4956	
Independent reflections	190 [R(int) = 0.0531]	
Coverage of independent reflections	100.0%	
Absorption correction	multi-scan	
Structure solution technique	direct methods	
Structure solution program	SHELXS-97 (Sheldrick, 2008)	
Refinement method	Full-matrix least-squares on F^2	
Refinement program	SHELXL-97 (Sheldrick, 2008)	
Function minimized	$\Sigma\ w(F_o^2 - F_c^2)^2$	
Data / restraints / parameters	190 / 0 / 20	
Goodness-of-fit on F^2	1.236	
Δ/σ_{max}	0.002	
Final R indices	184 data; I>2σ(I)	R1 = 0.0227, wR2 = 0.0546
	all data	R1 = 0.0241, wR2 = 0.0549
Weighting scheme	$w=1/[\sigma^2(F_o^2)+(0.0279P)^2+3.4262P]$where $P=(F_o^2+2F_c^2)/3$	
Absolute structure parameter	0.5(1)	
Largest diff. peak and hole	0.606 and -1.098 eÅ-3	
R.M.S. deviation from mean	0.194 eÅ-3	

Table SI-6. Atomic coordinates and equivalent isotropic atomic displacement parameters (Å²) for $Mn_{2.20}Zn_{10.8}$

U(eq) is defined as one third of the trace of the orthogonalized U_{ij} tensor.				
	x/a	y/b	z/c	U(eq)
Zn1	0.82805(5)	0.17195(5)	0.17195(5)	0.0095(2)
Mn1	0.82805(5)	0.17195(5)	0.17195(5)	0.0095(2)
Mn2	0	0.35463(7)	0	0.0145(2)
Zn2	0	0.35463(7)	0	0.0145(2)
Mn3	0.10968(5)	0.10968(5)	0.10968(5)	0.0189(2)
Mn4	0.68879(4)	0.31121(4)	0.96328(5)	0.0203(1)

Table SI-7: $Mn_{2.33}Zn_{10.67}$ Crystallographic Data

Chemical formula	$Mn_{2.33}Zn_{10.67}$	
Formula weight	825.53	
Temperature	296(2) K	
Wavelength	0.71073 Å	
Crystal system	cubic	
Space group	I -4 3 m	
Unit cell dimensions	a = 9.155(2) Å	$\alpha = 90°$
Volume	767.4(2) Å^3	
Z	4	
Density (calculated)	7.145 g/cm^3	
Absorption coefficient	36.263 mm^{-1}	
F(000)	1513	

Table SI-8. Data collection and structure refinement for $Mn_{2.33}Zn_{10.67}$

Theta range for data collection	3.15 to 27.34°	
Index ranges	-11<=h<=11, -11<=k<=11, -11<=l<=11	
Reflections collected	3736	
Independent reflections	188 [R(int) = 0.0901]	
Coverage of independent reflections	100.00%	
Absorption correction	multi-scan	
Structure solution technique	direct methods	
Structure solution program	SHELXS-97 (Sheldrick, 2008)	
Refinement method	Full-matrix least-squares on F^2	
Refinement program	SHELXL-97 (Sheldrick, 2008)	
Function minimized	$\Sigma\ w(F_o^2 - F_c^2)^2$	
Data / restraints / parameters	188 / 0 / 20	
Goodness-of-fit on F^2	1.187	
Final R indices	174 data; I>2σ(I)	R1 = 0.0296, wR2 = 0.0603
	all data	R1 = 0.0336, wR2 = 0.0620
Weighting scheme	w=1/[σ^2(F$_o^2$)+(0.0114P)^2+8.7244P] where P=(F$_o^2$+2F$_c^2$)/3	
Absolute structure parameter	0.3(2)	
Largest diff. peak and hole	0.729 and -1.245 eÅ^{-3}	
R.M.S. deviation from mean	0.237 eÅ^{-3}	

Table SI-9. Atomic coordinates and equivalent isotropic atomic displacement parameters (Å^2) for $Mn_{2.33}Zn_{10.67}$.

U(eq) is defined as one third of the trace of the orthogonalized U$_{ij}$ tensor.				
	x/a	y/b	z/c	U(eq)
Zn1	0.1097(2)	0.1097(2)	0.1097(2)	0.0192(6)
Zn2	0.8274(2)	0.1726(2)	0.1726(2)	0.010(1)
Mn2	0.8274(2)	0.1726(2)	0.1726(2)	0.010(1)
Zn3	0	0.3541(2)	0	0.0150(8)
Mn3	0	0.3541(2)	0	0.0150(8)
Zn4	0.6889(1)	0.3111(1)	0.96319(16)	0.0205(4)

Table SI-10: $Mn_{2.50}Zn_{10.50}$ Crystallographic Data

Chemical formula	$Mn_{2.50}Zn_{10.50}$	
Formula weight	1647.57	
Temperature	296(2) K	
Wavelength	0.71073 Å	
Crystal system	cubic	
Space group	I -4 3 m	
Unit cell dimensions	a = 9.177(2) Å	α = 90°
Volume	772.9(3) Å^3	
Z	4	
Density (calculated)	7.080 g/cm^3	
Absorption coefficient	35.759 mm^{-1}	
F(000)	1510	

Table SI-11. Data collection and structure refinement for $Mn_{2.50}Zn_{10.50}$.

Theta range for data collection	3.14 to 31.30°	
Index ranges	-13<=h<=12, -13<=k<=13, -12<=l<=13	
Reflections collected	4530	
Independent reflections	264 [R(int) = 0.0412]	
Coverage of independent reflections	100.00%	
Absorption correction	multi-scan	
Structure solution technique	direct methods	
Structure solution program	SHELXS-97 (Sheldrick, 2008)	
Refinement method	Full-matrix least-squares on F^2	
Refinement program	SHELXL-97 (Sheldrick, 2008)	
Function minimized	Σ w(F$_o$^{2} - F$_c$^{2})^2	
Data / restraints / parameters	264 / 0 / 21	
Goodness-of-fit on F^2	1.12	
Δ/σ_{max}	0.003	
Final R indices	251 data; I>2σ(I)	R1 = 0.0184, wR2 = 0.0401
	all data	R1 = 0.0205, wR2 = 0.0406
Weighting scheme	w=1/[σ^2(F$_o$^{2})+(0.0235P)^2+0.1831P] where P=(F$_o$^{2}+2F$_c$^{2})/3	
Absolute structure parameter	0.5(0)	
Extinction coefficient	0.0004(0)	
Largest diff. peak and hole	0.518 and -0.830 eÅ^{-3}	
R.M.S. deviation from mean	0.151 eÅ^{-3}	

Table SI-12. Atomic coordinates and equivalent isotropic atomic displacement parameters (Å^2) for $Mn_{2.50}Zn_{10.50}$.
U(eq) is defined as one third of the trace of the orthogonalized U$_{ij}$ tensor.

	x/a	y/b	z/c	U(eq)
Zn1	0.82758(3)	0.17242(3)	0.17242(3)	0.0108(1)
Mn1	0.82758(3)	0.17242(3)	0.17242(3)	0.0108(1)
Mn2	0.68847(2)	0.31153(2)	0.96351(3)	0.02014(6)
Zn3	0	0.35386(4)	0	0.01486(9)
Mn3	0	0.35386(4)	0	0.01486(9)
Zn4	0.10966(3)	0.10966(3)	0.10966(3)	0.01955(8)

Table SI-13: $Mn_{2.54}Zn_{10.46}$ Crystallographic Data

Chemical formula	$Mn_{2.54}Zn_{10.46}$	
Formula weight	823.32	
Temperature	296(2) K	
Wavelength	0.71073 Å	
Crystal system	cubic	
Space group	I -4 3 m	
Unit cell dimensions	a = 9.16(2) Å	α = 90°
Volume	769.(3) Å^3	
Z	4	
Density (calculated)	7.119 g/cm^3	
Absorption coefficient	35.910 mm^{-1}	
F(000)	1509	

Table SI-14. Data collection and structure refinement for $Mn_{2.54}Zn_{10.46}$.

Theta range for data collection	3.15 to 27.33°	
Index ranges	-11<=h<=8, -11<=k<=11, -11<=l<=11	
Reflections collected	2116	
Independent reflections	187 [R(int) = 0.0529]	
Coverage of independent reflections	100.00%	
Absorption correction	multi-scan	
Structure solution technique	direct methods	
Structure solution program	SHELXS-97 (Sheldrick, 2008)	
Refinement method	Full-matrix least-squares on F^2	
Refinement program	SHELXL-97 (Sheldrick, 2008)	
Function minimized	Σ w(F$_o^2$ - F$_c^2$)^2	
Data / restraints / parameters	187 / 0 / 21	
Goodness-of-fit on F^2	1.223	
Final R indices	177 data; I>2σ(I)	R1 = 0.0232, wR2 = 0.0497
	all data	R1 = 0.0256, wR2 = 0.0502
Weighting scheme	w=1/[σ^2(F$_o^2$)+(0.0209P)^2+0.0000P] where P=(F$_o^2$+2F$_c^2$)/3	
Absolute structure parameter	0.2(2)	
Extinction coefficient	0.0006(1)	
Largest diff. peak and hole	0.573 and -0.692 eÅ^{-3}	
R.M.S. deviation from mean	0.155 eÅ^{-3}	

Table SI-15. Atomic coordinates and equivalent isotropic atomic displacement parameters (Å^2) for $Mn_{2.54}Zn_{10.46}$.
U(eq) is defined as one third of the trace of the orthogonalized U$_{ij}$ tensor.

	x/a	y/b	z/c	U(eq)
Zn1	0.89044(11)	0.89044(11)	0.8904(1)	0.0219(4)
Zn2	0.67263(11)	0.67263(11)	0.6726(1)	0.0107(7)
Mn2	0.67263(11)	0.67263(11)	0.6726(1)	0.0107(7)
Zn3	0.64585(13)	0	0	0.0157(5)
Mn3	0.64585(13)	0	0	0.0157(5)
Mn4	0.68870(9)	0.68870(9)	0.9630(1)	0.0226(3)

Table SI-16: $Mn_{2.60}Zn_{10.40}$ Crystallographic Data

Chemical formula	Mn$_{2.60}$Zn$_{10.40}$	
Formula weight	822.69	
Temperature	296(2) K	
Wavelength	0.71073 Å	
Crystal system	cubic	
Space group	I -4 3 m	
Unit cell dimensions	a = 9.1724(17) Å	α = 90°
Volume	771.7(2) Å^3	
Z	4	
Density (calculated)	7.081 g/cm^3	
Absorption coefficient	35.659 mm^{-1}	
F(000)	1508	

Table SI-17. Data collection and structure refinement for Mn$_{2.60}$Zn$_{10.40}$.

Theta range for data collection	3.14 to 30.93°	
Index ranges	-12<=h<=13, -13<=k<=13, -13<=l<=13	
Reflections collected	7468	
Independent reflections	258 [R(int) = 0.0477]	
Coverage of independent reflections	100.00%	
Absorption correction	multi-scan	
Structure solution technique	direct methods	
Structure solution program	SHELXS-97 (Sheldrick, 2008)	
Refinement method	Full-matrix least-squares on F^2	
Refinement program	SHELXL-97 (Sheldrick, 2008)	
Function minimized	Σ w(F$_o$^{2} - F$_c$^{2})^2	
Data / restraints / parameters	258 / 0 / 20	
Goodness-of-fit on F^2	1.118	
Δ/σ_{max}	0.001	
Final R indices	246 data; I>2σ(I)	R1 = 0.0199, wR2 = 0.0410
	all data	R1 = 0.0222, wR2 = 0.0414
Weighting scheme	w=1/[σ^2(F$_o$^{2})+(0.0226P)^2+0.9800P] where P=(F$_o$^{2}+2F$_c$^{2})/3	
Absolute structure parameter	0.5(1)	
Largest diff. peak and hole	0.729 and -1.330 eÅ^{-3}	
R.M.S. deviation from mean	0.197 eÅ^{-3}	

Table SI-18. Atomic coordinates and equivalent isotropic atomic displacement parameters (Å^2) for Mn$_{2.60}$Zn$_{10.40}$.

U(eq) is defined as one third of the trace of the orthogonalized U$_{ij}$ tensor.				
	x/a	y/b	z/c	U(eq)
Zn1	0.82765(6)	0.17235(6)	0.17235(6)	0.0097(4)
Mn1	0.82765(6)	0.17235(6)	0.17235(6)	0.0097(4)
Mn3	0.68851(5)	0.31149(5)	0.96356(7)	0.0193(2)
Zn2	0.10981(7)	0.10981(7)	0.10981(7)	0.0185(3)
Zn4	0	0.35384(8)	0	0.0134(3)
Mn4	0	0.35384(8)	0	0.0134(3)

SI.2 Powder X-ray Diffraction
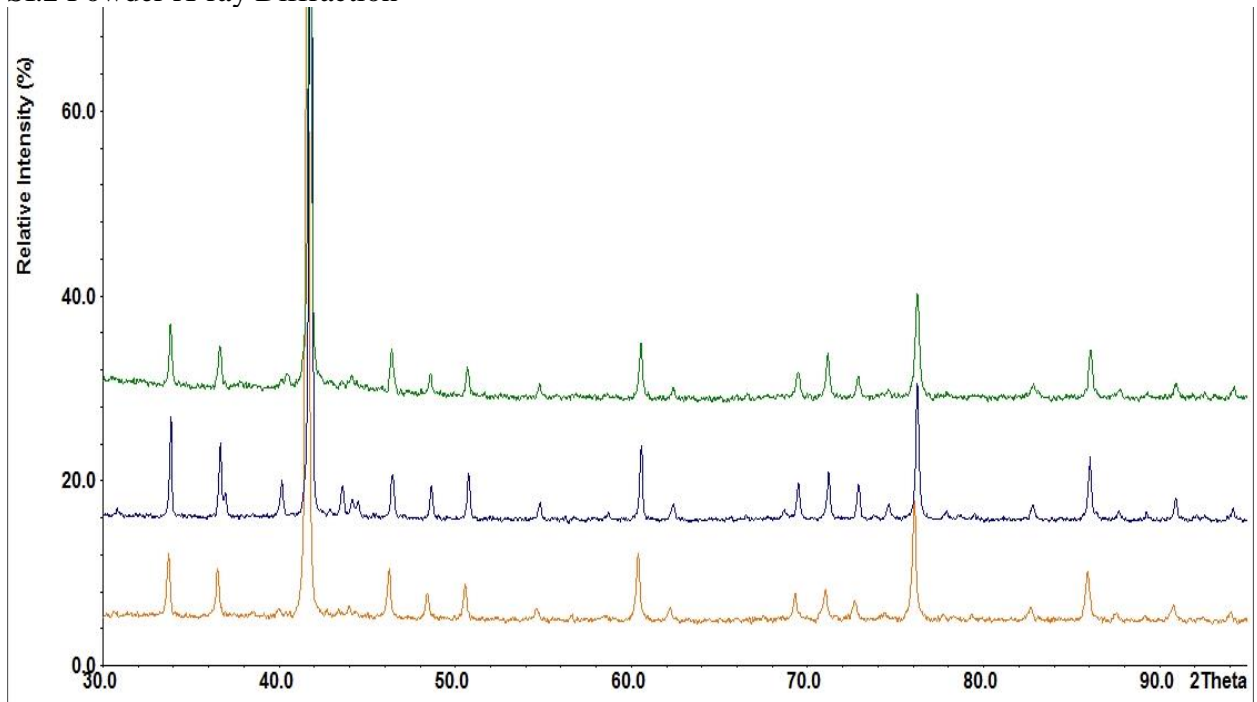
Figure SI2.1: All samples loaded $Mn_{3.00(1)}Zn_{10.00(1)}$) Green: annealed at 400 °C for 48hrs, Blue: annealed at 400 °C, Orange: annealed 198 hrs at 350 °C
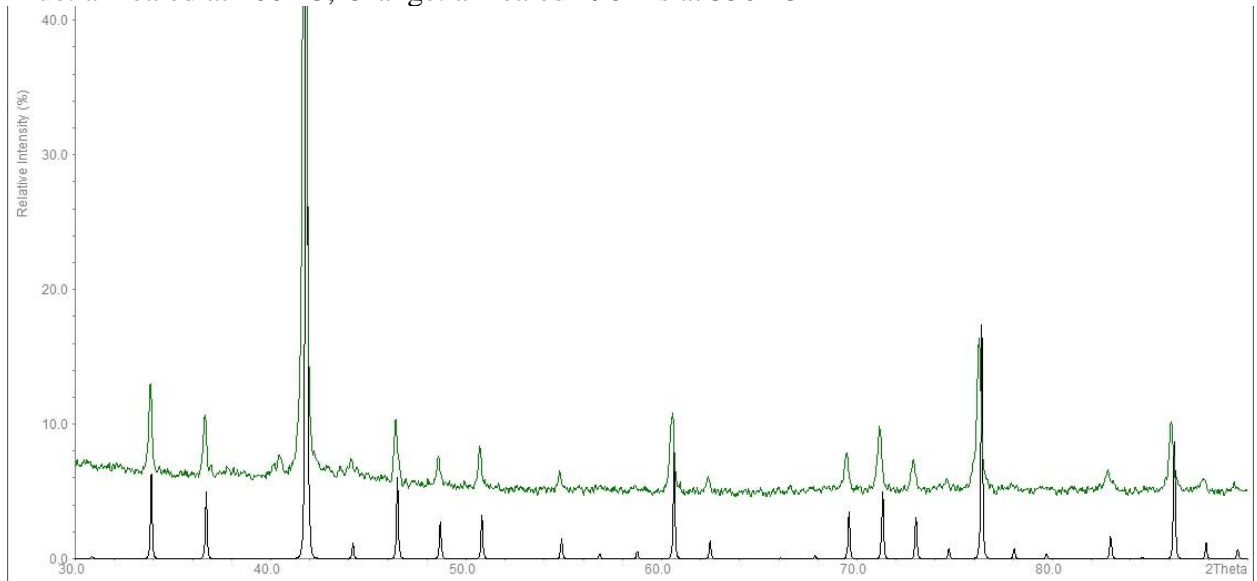
Figure SI2.2: Lattice parameter by SCXRD 9.177 Å Lattice parameters by PXRD: 9.1708(1) Å
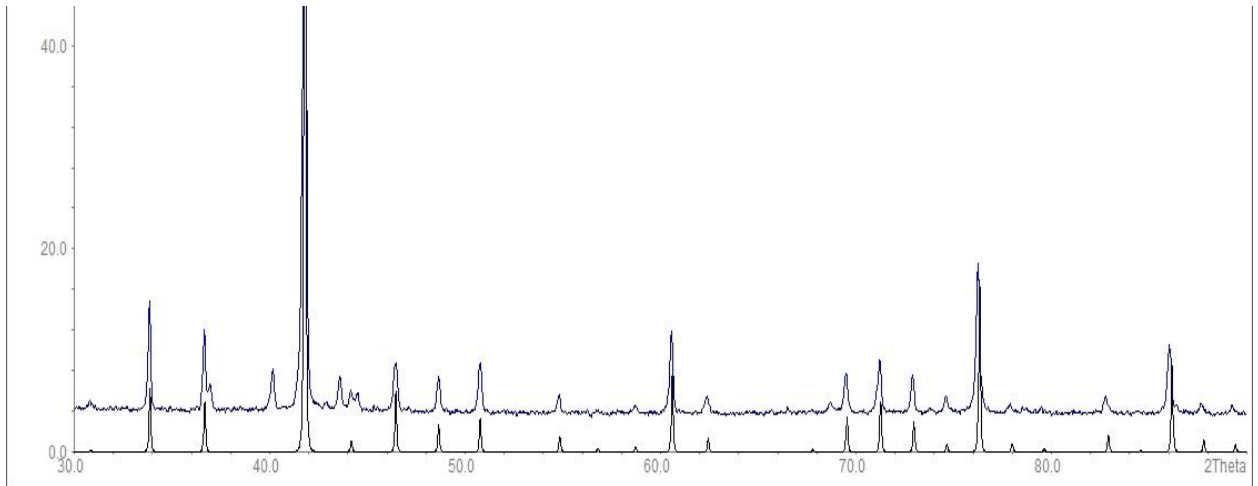
Figure SI2.3: Lattice Parameter by SCXRD: 9.161Å Lattice parameter by PXRD: 9.1655(1) Å
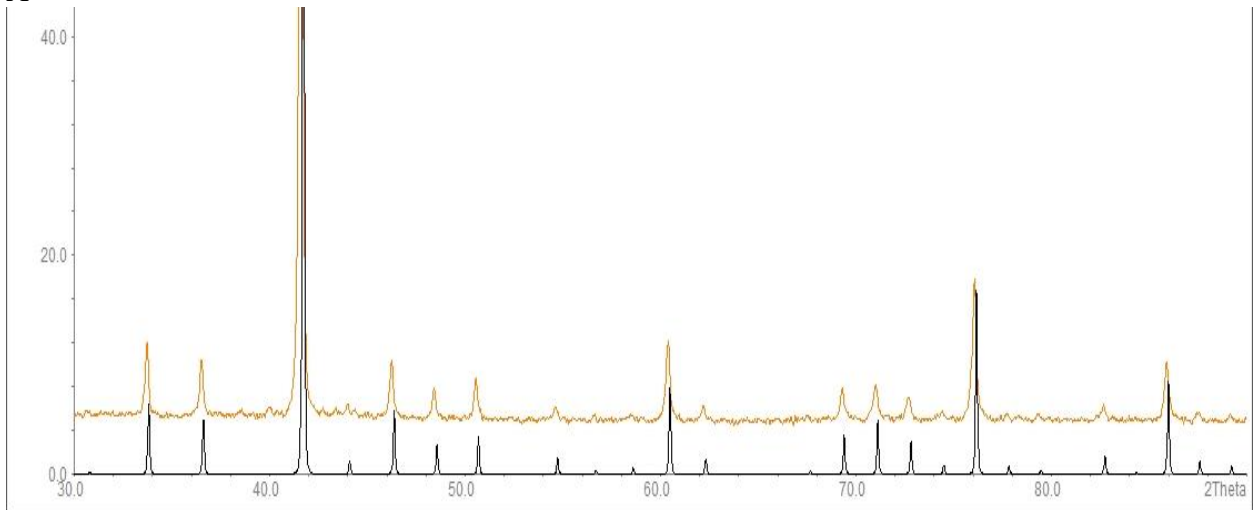
Figure SI2.4: SCXRD lattice parameters: 9.1771 Lattice parameters by PXRD: 9.1877(1) Å
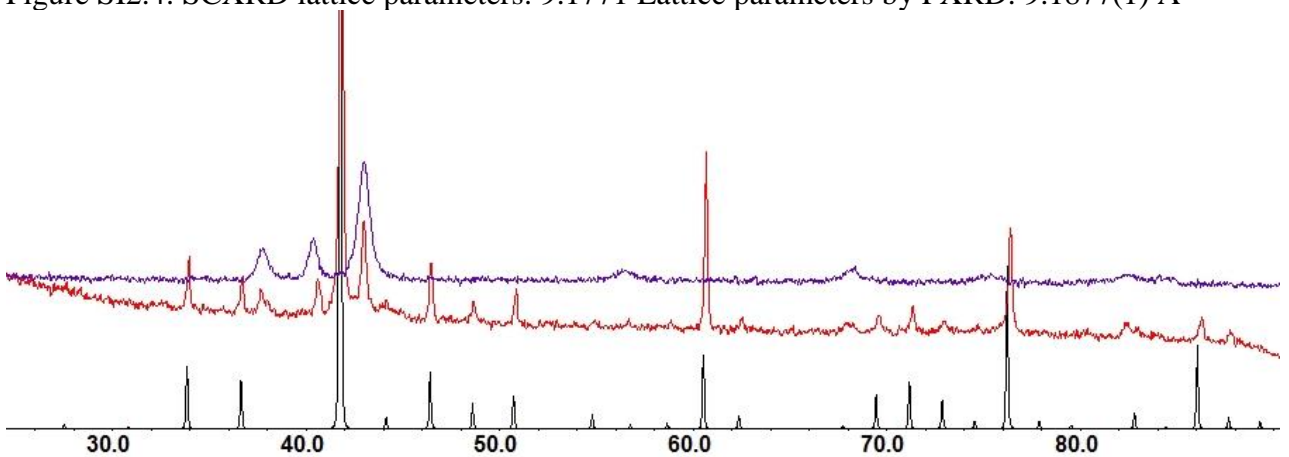
Figure SI2.5: M010L(red, loaded Mn_3Zn_{10}) and M007(purple, loaded Mn_2Zn_3) and $Mn_{2.60}Zn_{10.40}$ a=9.172(2) (black)

SI3: Additional Electronic Structures
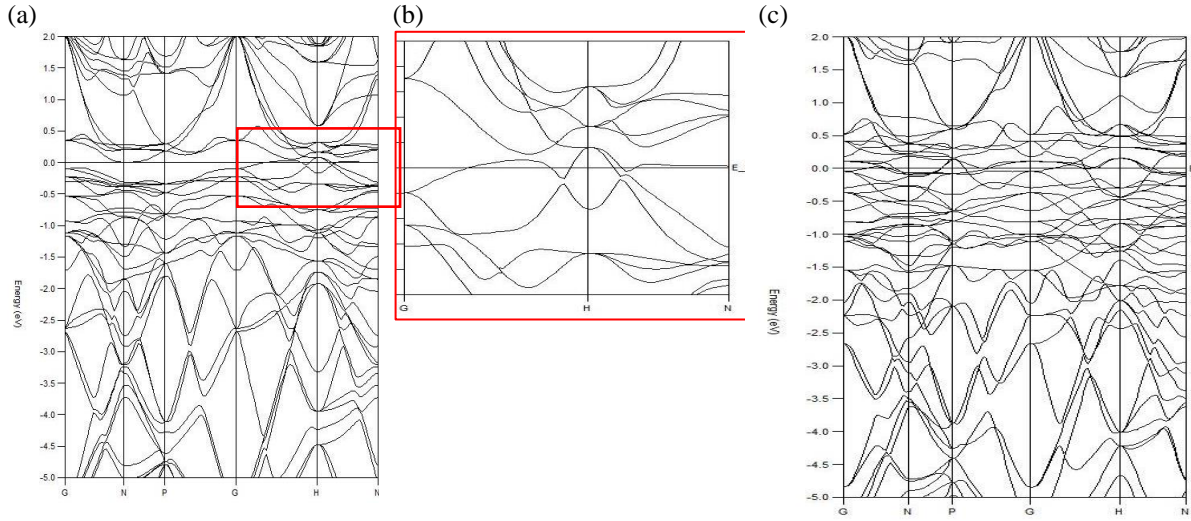
Figure SI3.1: (a)Band structure of Mn_2Zn_{11} from -5 to 2 eV inlay highlighting region where bands cross the Fermi energy (b) zoomed in on BAND structure (red inlay from -0.5 to 0.5 eV) (c) Band Structure of Mn_3Zn_{10}. The Mn_3Zn_{10} band structure shows more activity from the Mn $3d$ band near the Fermi level which arises from the Mn $3d$ band splits into multiple bands in the range of -0.5-1.0eV unlike in the Mn_2Zn_{11} model.
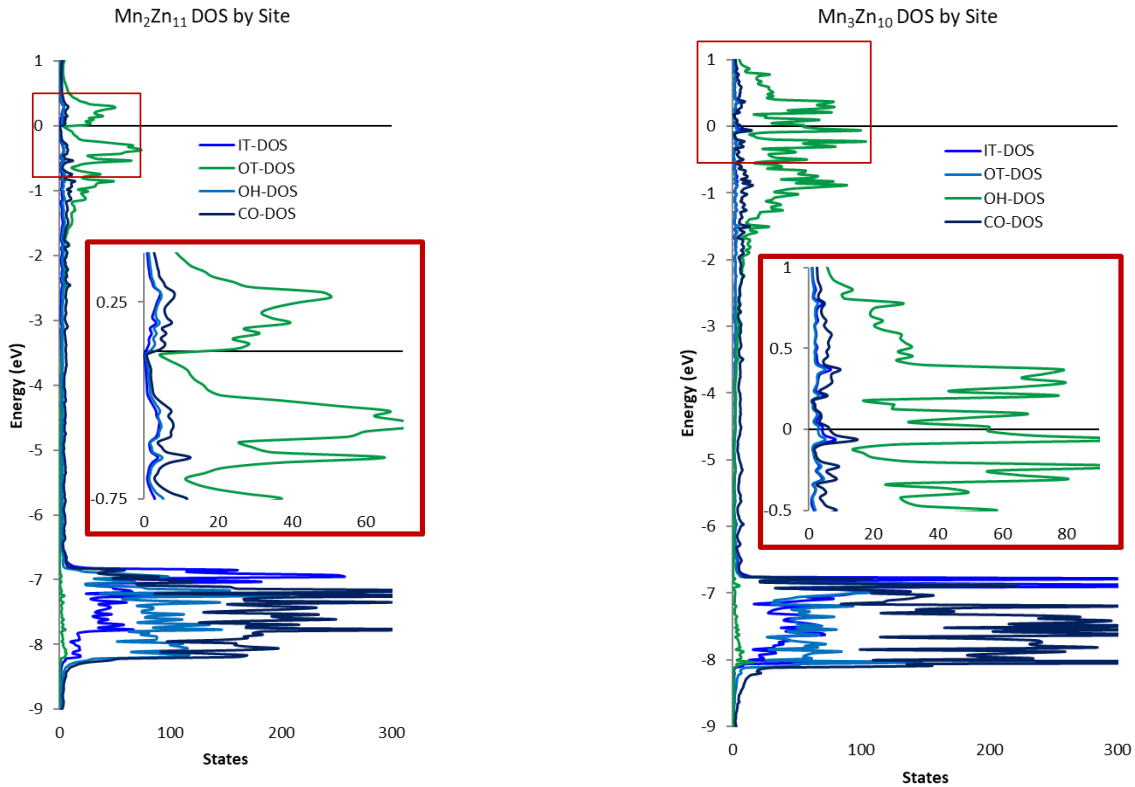
Figure SI3.2: Mn_2Zn_{11} DOS by site (left) and Mn_3Zn_{10} (right). Inset to the DOS is a region from -0.75 eV to 0.5 eV highlighting the pseudo gap formed by Mn atoms on the OT site. Inset to the Mn_3Zn_{10} DOS is the region from -0.5 eV to 1.0 eV highlighting the pseudo gap at $Mn_{2.85}Zn_{10.15}$.

Figure SI3.3(a) Inner Tetrahedron local overlap environment (b) Outer tetrahedron overlap environment (c) Octahedron overlap environment where CO(1) represents overlap distances less than 2.9 Å and CO(2) represents overlap distances of greater than 2.9 Å (d) Cuboctahedron local overlap environment where CO(1) represents overlap distances less than 2.9 Å and CO(2) represents overlap distances of greater than 2.9 Å

(a)

(b)

(c)

(d)

Figure SI3.4 (a) Local overlap environment of Mn_3Zn_{10} Inner Tetrahedron (b) local overlap environment of Outer Tetrahedron (c) Local overlap environment of Octahedron with CO(1) representing bonds that are less than 2.9 9 Å   (d) Cuboctahedron local overlap environment where CO(1) represents overlap distances less than 2.9 Å and CO(2) represents overlap distances of greater than 2.9 Å
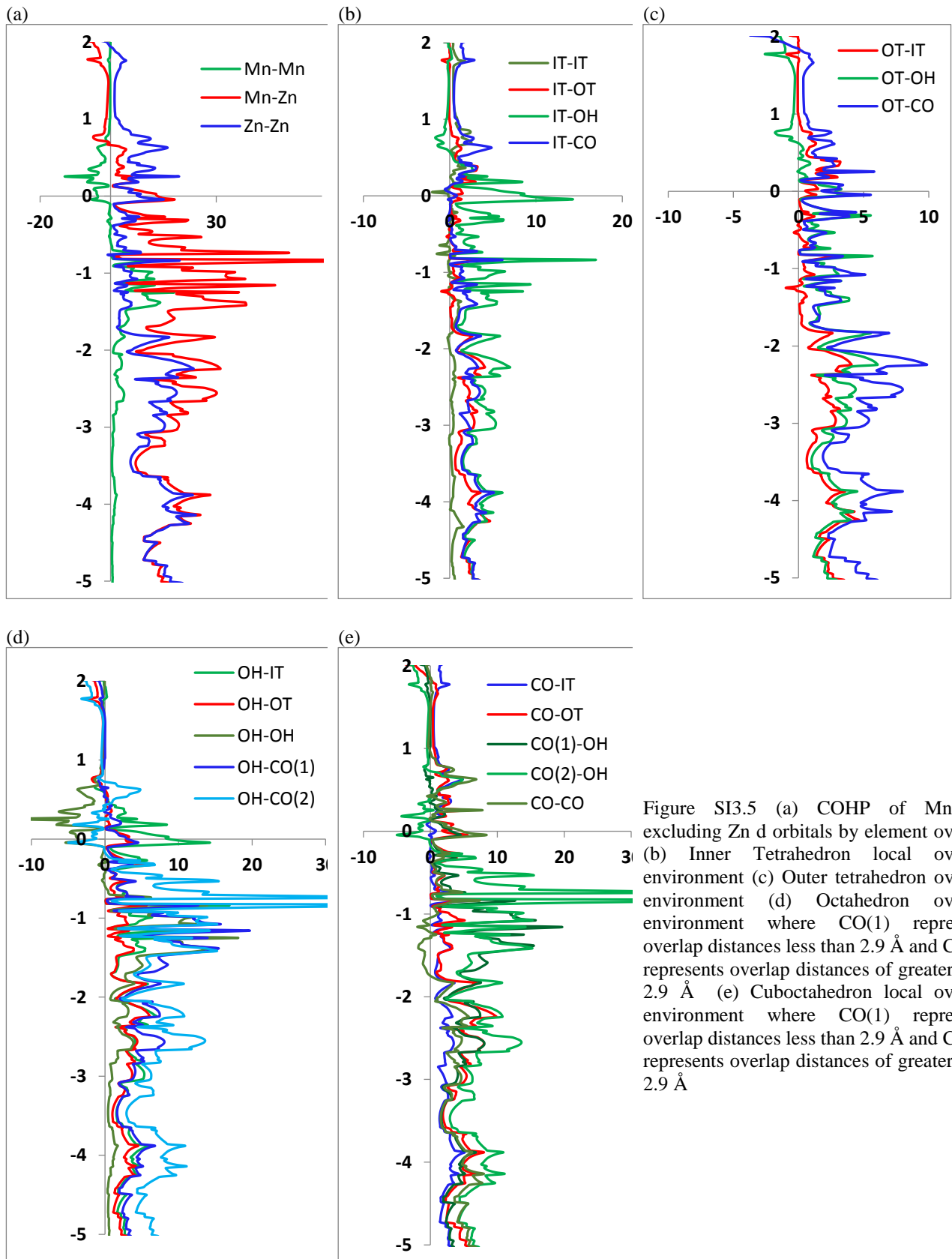
Figure SI3.5 (a) COHP of Mn_3Zn_{10} excluding Zn d orbitals by element overlap (b) Inner Tetrahedron local overlap environment (c) Outer tetrahedron overlap environment (d) Octahedron overlap environment where CO(1) represents overlap distances less than 2.9 Å and CO(2) represents overlap distances of greater than 2.9 Å (e) Cuboctahedron local overlap environment where CO(1) represents overlap distances less than 2.9 Å and CO(2) represents overlap distances of greater than 2.9 Å

Figure SI3.6 (a) COHP of Mn_2Zn_{11} excluding Zn d orbitals by element overlap (b) Inner Tetrahedron local overlap environment (c) Outer tetrahedron overlap environment (d) Octahedron overlap environment where CO(1) represents overlap distances less than 2.9 Å and CO(2) represents overlap distances of greater than 2.9 Å (e) Cuboctahedron local overlap environment where CO(1) represents overlap distances less than 2.9 Å and CO(2) represents overlap distances of greater than 2.9 Å
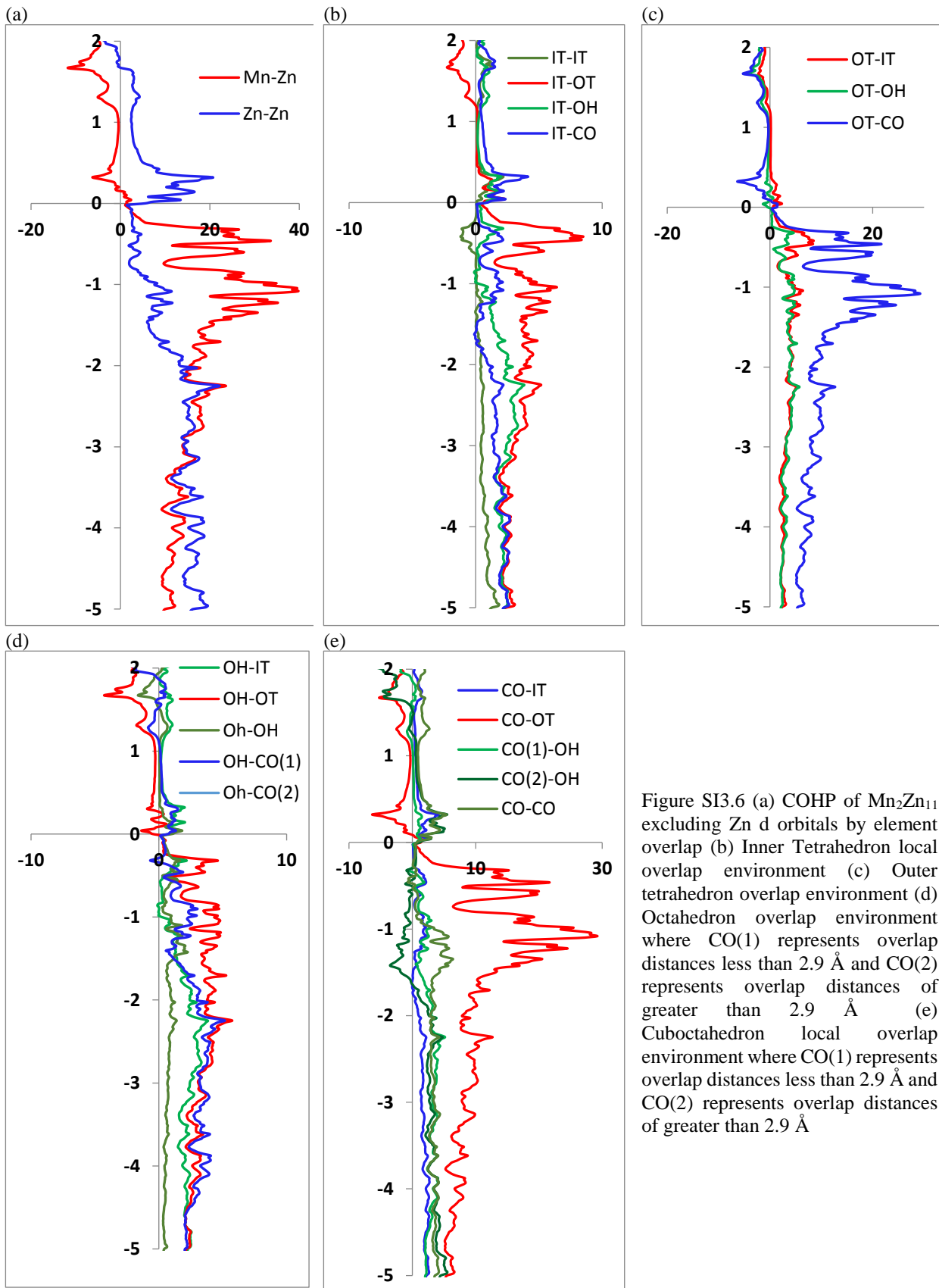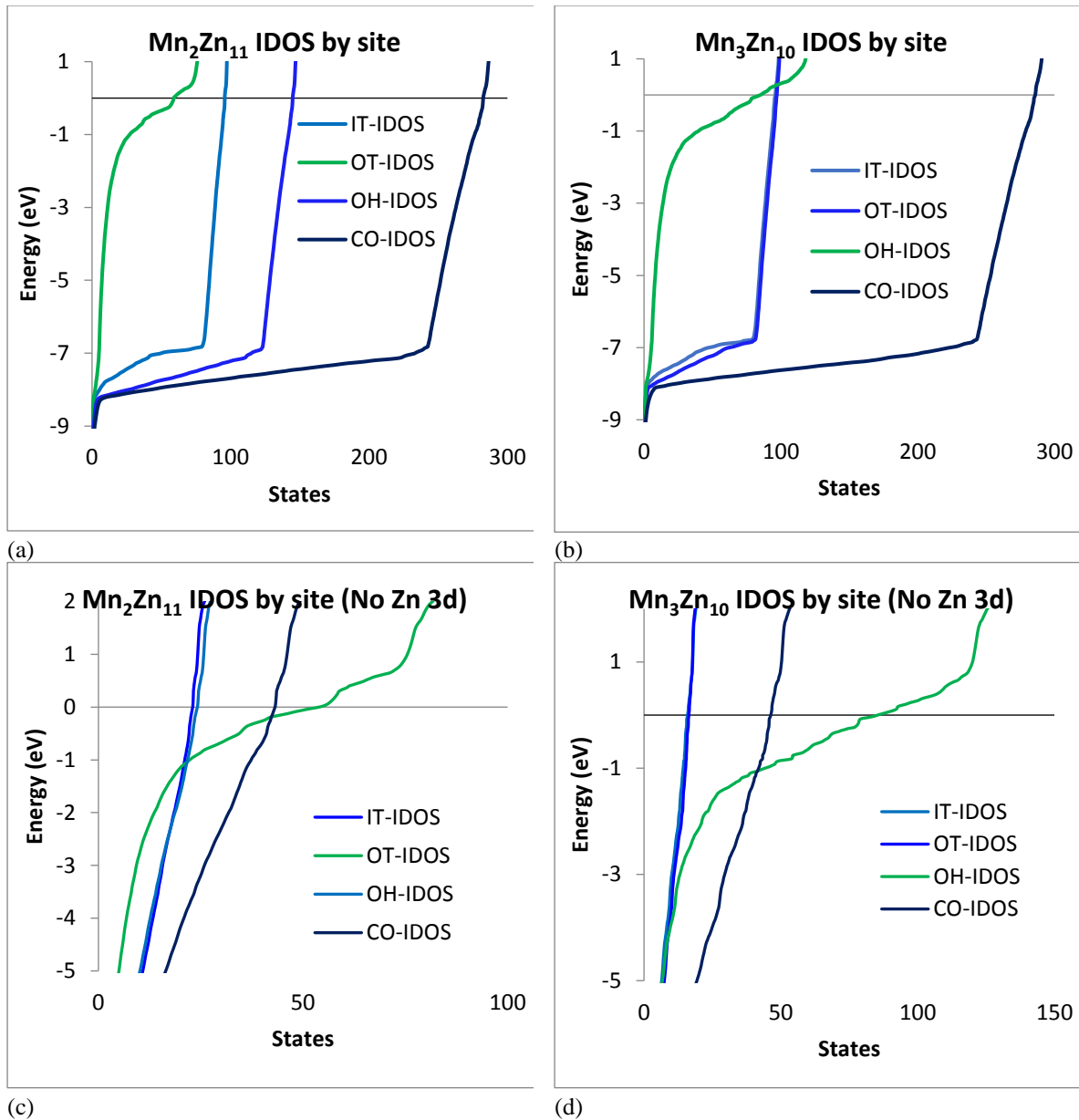
(a)

(b)

(c)

(d)

Figure SI3.7: IDOS for charge density analysis using TB-LMTO-ASA (a) Mn_2Zn_{11} with Zn 3d orbitals included (b) Mn_3Zn_{10} with Zn 3d orbitals included (c) Mn_2Zn_{11} without Zn $3d$ electrons (d)Mn_3Zn_{10} IDOS without Zn $3d$ electrons

SI4: Bonding
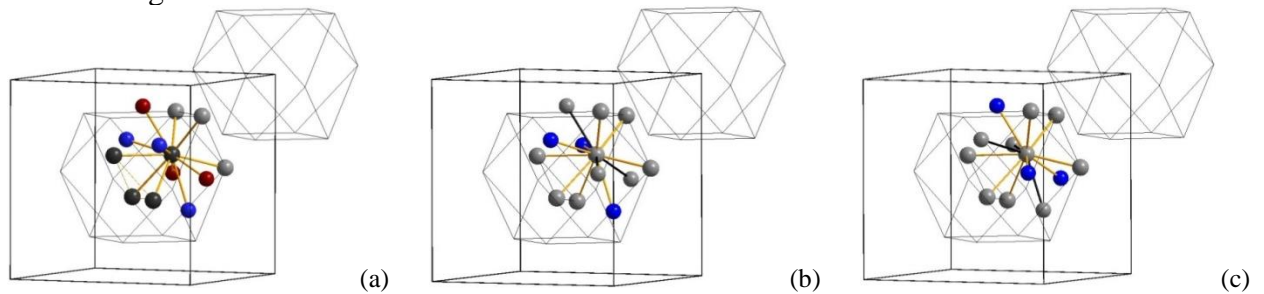
Figure SI4.1: Local Bonding Environment of IT site.
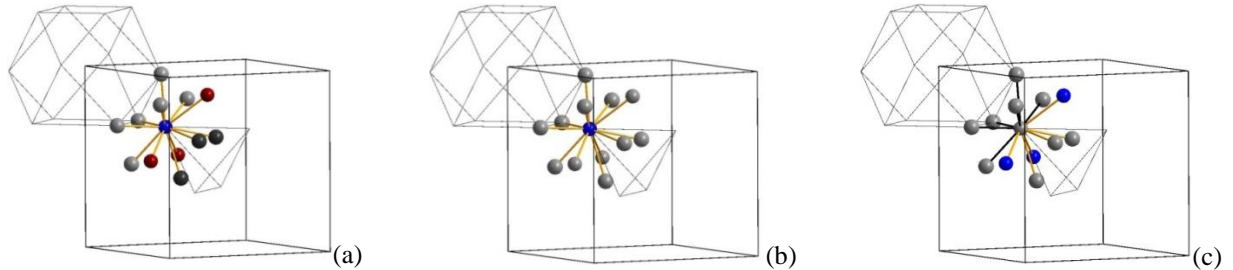
Figure SI4.2: Local Bonding Environments of the OT site
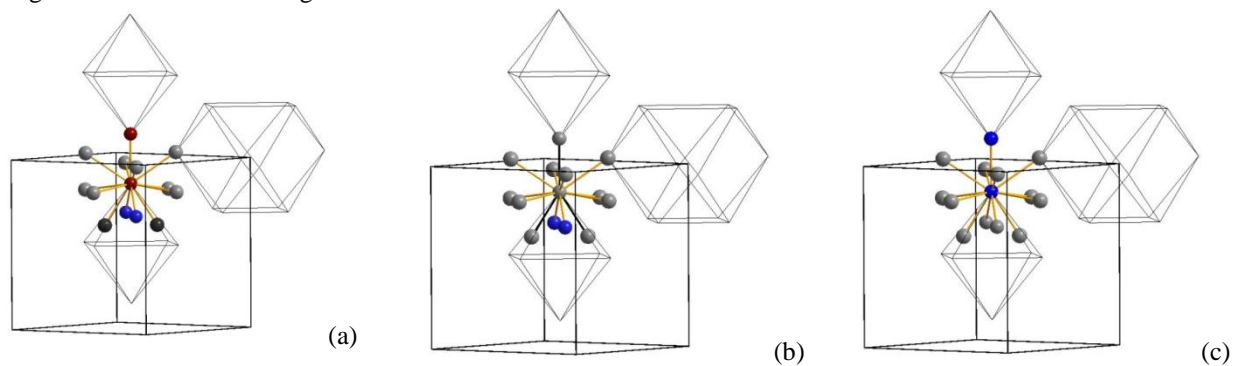
Figure SI4.3: Local Bonding Environments of the OH site
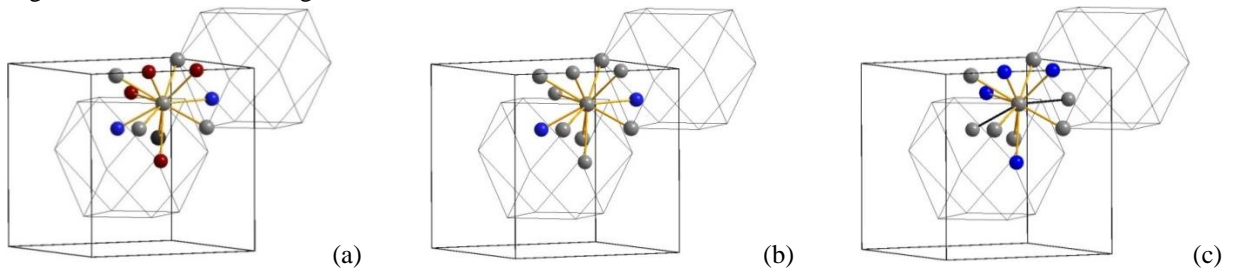
Figure SI4.4: Local Bonding Environment of the CO site

*Outlines of relevant shells are shown in thin black lines, bonding interactions are shown in thick gold lines, and antibonding interactions are shown in thick black lines. 1-4(a) shows the experimental compositions with no determination of bonding or antibonding majority Zn sites are shown in red and majority Mn sites are shown in blue, and Zn sites are shown in grays. 1-4(b) shows the Mn_2Zn_{11} composition with bonding and antibonding interactions Mn sites are shown in blue and Zn sites are shown in gray. 1-4(c) shows the Mn_3Zn_{10} composition with bonding and antibonding interactions Mn sites are shown in blue, Zn sites are shown in gray.

Table SI4.5: Elemental Bond Analysis

Elements		Distance Range Å	multiplicity	percent	Avg. ICOHP per Bond
Mn_2Zn_{11}					
Mn	Mn	N/A	0	0	-
Mn	Zn	2.6345(6)-2.7879(6)	96	61.6%	0.709
Zn	Zn	2.6456(5)-2.9681(6)	210	38.4%	0.202
Mn_3Zn_{10}					
Mn	Mn	2.686(1)	6	7.5%	1.582
Mn	Zn	2.6456(5)-2.9681(6)	144	70.6%	0.621
Zn	Zn	2.6345(6)-2.8415(8)	156	21.9%	0.178
Mn_2Zn_{11} (Zn d excluded)					
Mn	Mn	N/A	0	0	N/A
Mn	Zn	2.62867-2.78625	96	96	1.250
Zn	Zn	2.64067-2.96073	210	210	0.739
Mn_3Zn_{10} (Zn d excluded)					
Mn	Mn	N/A	6	5%	2.200
Mn	Zn	2.62867-2.78625	144	53%	1.009
Zn	Zn	2.64067-2.96073	156	51%	0.893

The percentages above are based on the absolute value of ICOHP for states filled below the Fermi Energy.

Table SI4.6: $Mn_{2.60}Zn_{10.40}$ element and bond analysis

Element Type		% total	Population
Mn	Mn	2.23%	6.8
Mn	Zn	37.7%	115.3
Zn	Zn	60.1%	183.9

Table SI-21: $Mn_{2.33}Zn_{10.67}$ Element and Bond population analysis

Element Type		% total	Population
Mn	Mn	2.02%	6.2
Mn	Zn	36.0%	110.3
Zn	Zn	61.9%	189.5

*refined composition from SCXRD closest to midpoint in estimated phase width using probability of contact between individual elements

Table SI4.7: Mn_2Zn_{11} Bond analysis (excluding Zn 3d orbitals)

Bond Type		Element Type	Distance Å	Mult.	% Total	ICOHP/ Bond
IT	IT	Zn 12	2.84142	12	2.42%	0.554
IT	OT	Zn 24	2.70285	24	9.40%	1.078
IT	OH	Zn 24	2.65615	24	8.41%	0.964
IT	CO	Zn 24	2.69517	24	7.47%	0.856
OT	OH	Mn 24	2.78625	24	9.01%	1.033
OT	CO	Mn 24	2.62867	24	25.2%	1.445
		24	2.67780	24		
OH	OH	Zn 6	2.66328	6	2.69%	1.235
OH	CO	Zn 24	2.64067	24	9.41%	1.079
		48	2.89815	48	13.4%	0.514
		24	2.96073	24		
CO	CO	Zn 48	2.73256	48	12.5%	0.719

Table SI4.8: Mn$_3$Zn10 Bond analysis (excluding Zn d orbitals)

Bond Type		Element Type		Distance Å	mult.	% total	ICOHP / Bond
IT	IT	Zn	Zn	2.84638	12	2.2%	0.554
IT	OT	Zn	Zn	2.70757	24	6.7%	0.834
IT	OH	Zn	Mn	2.66079	24	9.3%	1.158
IT	CO	Zn	Zn	2.69988	24	7.5%	0.934
OT	OH	Zn	Mn	2.79112	24	7.3%	0.900
OT	CO	Zn	Zn	2.63326	24	16.1%	0.999
		Zn	Zn	2.68248	24		
OH	OH	Mn	Mn	2.66974	6	4.4%	2.196
OH	CO	Mn	Zn	2.64529	24	11.9%	1.473
		Mn	Zn	2.90321	48	20.3%	0.841
		Mn	Zn	2.9659	24		
CO	CO	Zn	Zn	2.73733	48	14.2%	0.880

SI5 Phase Analysis and Physical Property measurement

Element	Weight%	Atomic%
Mn K	16.70	19.25
Zn K	83.30	80.75

Element	Weight%	Atomic%
Mn K	16.39	18.91
Zn K	83.61	81.09

Element	Weight%	Atomic%
Mn K	15.91	18.38
Zn K	84.09	81.62

Element	Weight %	Atomic %
Mn K	16.60	19.15
Zn K	83.40	80.85
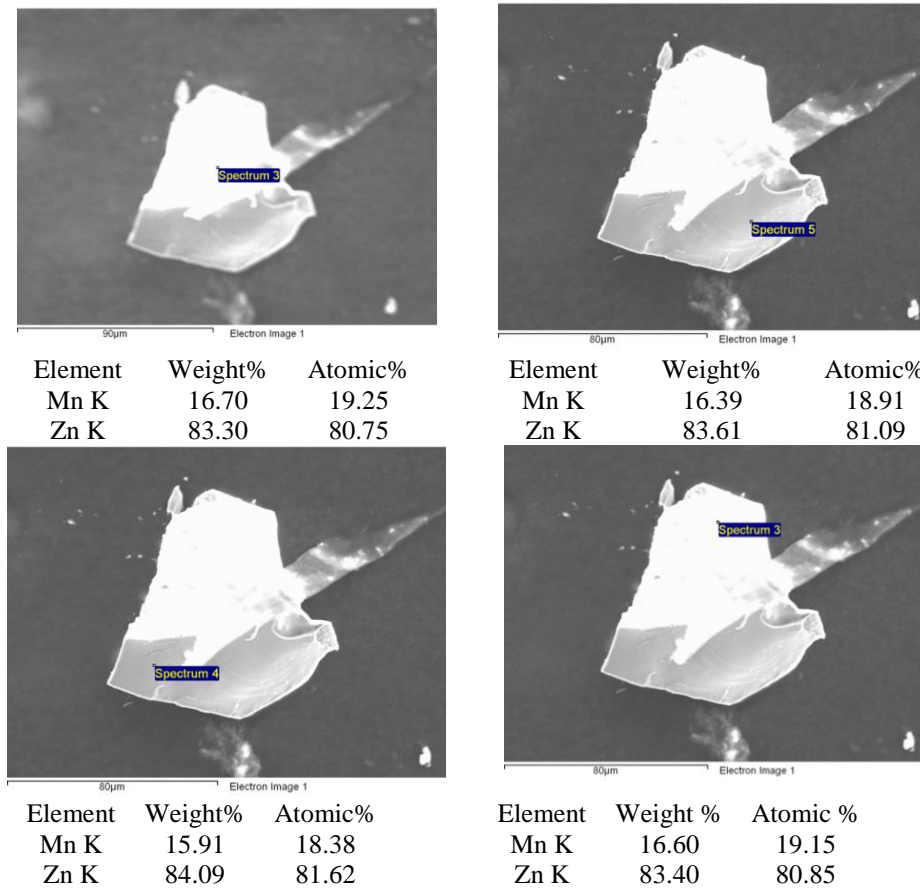
Figure SI5.1: (a-d) EDS images of chunk from pure phase Mn$_{2.5}$Zn$_{10.5}$

CHAPTER 4: VEC DRIVEN STRUCTURAL TRANSITION IN Mn$_{5-Y}$Al$_{8-X}$Zn$_{X+Y}$ Γ-BRASSES

S. Eveland, S. Thiminaiah, and G. Miller "Γ-brasses in the Mn-Zn-Al system:

Stephanie Eveland[a,b*], Srinivasa Thiminaiah[b], Gordon Miller[a,b]

[a] Department of Chemistry, Iowa State University Ames, IA, USA 50011

[b] Ames Laboratory Ames, IA, USA 50011

Abstract

The Mn$_{5-y}$Al$_{8-x}$Zn$_{x+y}$ γ-brass system was studied experimentally by systematic substitution of Zn for Al to investigate a proposed structural transition between cubic Mn$_{2+x}$Zn$_{11-x}$ (cI52[1]) and rhombohedral Mn$_5$Al$_8$ (hR78 a = 12.6548(3) Å c = 7.9457(2) Å [2]). From the results of single crystal x-ray diffraction (SCXRD), powder x-ray diffraction (PXRD), and scanning electron microscopy (SEM), Zn mixes with both Al and Mn throughout the composition range which increases the complexity of the systematic substitution. Zn shows preferential occupation for the inner tetrahedron (3a and 9b Wyckoff sites in hR78 unit cells and 8c Wyckoff sites in cI52 unit cells) and the octahedron (9b Wyckoff sites in the hR78 cell 12e Wyckoff sites in the cI52 cell) of the 26-atom γ-brass cluster [2]. First principles electronic structure calculations were used on stoichiometric crystalline models of Mn$_{5-y}$Al$_{8-x}$Zn$_{x+y}$ to evaluate interatomic interactions via Hamilton population and charge distribution to assess the observed phase width and atomic distribution of the crystal structure.

Introduction

Since the time of Hume-Rothery's study of the Cu-Zn system in the 1930's and his groundbreaking realization of the role of valence (*s* and *p*) electrons-to-atom (*e/a*) ratios for

the stability of intermetallic alloys of noble metals, much work has been done to expand the database of so-called Hume-Rothery phases [3]. These Hume-Rothery *e/a* ratios apply to such phases as α, β, and γ brasses as well as all other substitutional and interstitial solid solutions, although the rules are insufficient for most systems containing transition metals with partially filled valence *d*-bands. Γ-Brasses are a family of complex intermetallic compounds formed by bcc packings of 26-atom clusters which consist of four concentric shells of symmetry equivalent atoms. They are well described as Hume-Rothery phases, which means changes in valence electron concentration (VEC) of *s* and *p* electrons directly affect the structural arrangement of the 26-atom clusters, as well as the decoration of atoms in shells comprising the 26-atom clusters [3, 4]. When first studying the Cu_5Zn_8 γ-Brass (S.G I-43m) its *e/a* of 21/13 was considered to be 'ideal' for γ-brases and, in keeping with that electron counting convention developed by Hume-Rothery, certain metals such as Cr, Mn, Fe and Ni are assigned zero electrons to contribute to the *e/a* ratio.

The Mn–Zn–Al system was targeted to understand how local coordination environments, partially occupied 3*d* orbitals, and valence electron concentration (VEC) affect structural transformations between binary Mn–Zn and Mn–Al γ-brasses. Mn and Al form a rhombohedral γ-brass Mn_5Al_8. The 26-atom cluster in this case is composed of nine distinct groups of Wyckoff sites; two compose the inner tetrahedron, two compose the outer tetrahedron, two compose the octahedron, and three sites compose the cuboctohedron, [5]. By lowering the VEC through systematic substitution of Zn (2 valence electrons) for Al (3 valence electrons), a transformation of the cluster from nine atomic sites to four and rhombohedral to cubic symmetry occurs, which creates an opportunity to study site preference and atomic decoration, or coloring. This is accomplished while minimizing the

variable of chemical pressure by limiting the element for substitution to one, which would

vary the atomic radius by less than 15%, thereby adhering to Hume-Rothery's substitutional

solid solution rules [3], because Zn and Al have similar metallic radii 1.34 Å and 1.43 Å

respectively, for CN 12 [6].

Previous work with regards to the structural transition in the Zn–Cd system as well as

the spontaneous magnetizations and site preferences in the Fe-Zn, $T'_{1-x}T''_xSn_2$ (T', T'' = Ti,

V, Fe, Co, Ni) and Fe–Pd–Zn systems shows that by changing the *e/a* ratio, structural

transitions and atomic decoration changes are possible. [7-8]
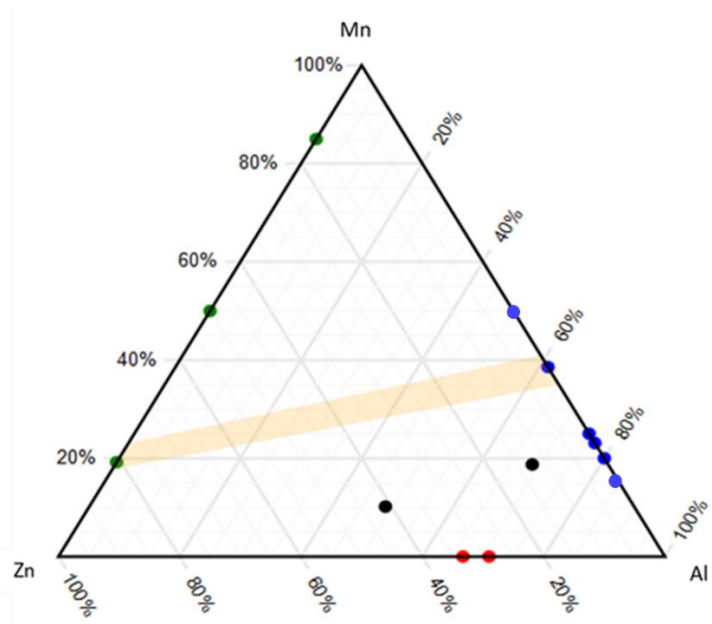
Figure 4.1: Existence diagram of Mn–Zn-Al system γ-brasses. In green, the $Mn_{2+x}Zn_{11-x}$ γ-brasses from previous work as well as the MnZn binary [1], and in blue the Mn_5Al_8 γ-brass produced by Thiminaiah et al, as well as other Al-rich Mn–Al binaries. In red two Zn-Al binaries are shown. The pink bar connecting the two green and single blue circles indicates the region where γ-brasses should form according to Hume-Rothery's experiments and observed phase widths in previous work as well as Thimmaiah et al [2].

Figure 4.1 shows the several compounds which have been identified in the Mn–Al–

Zn system; insufficient crystallographic has been reported to fully understand the rationale

for their atomic decoration and structure formation. According to the reported Mn–Zn, Mn–

Al, and Al–Zn phase diagrams, there is one rhombohedral γ-brass Mn_5Al_8 alongside other Al-rich Mn–Al binaries. A cluster of compounds forms near 80 at. % Al, (Mn_3Al_{10} hP26, $MnAl_4$ oP60, $MnAl_3$ cP*) [9-11] as well as the $MnAl_6$ QC at approximately 85% Al [12]. At 50% Al the tetragonal MnAl QC approximate forms [13]. A rhombohedral Zn-Al composite, which is not a γ-brass, demonstrates that Zn and Al can mix sites and achieve a nonstoichiometric composition [13, 14]. The stoichiometric and nonstoichiometric Zn-Al binaries are marked in red in Figure 4.2.1. Two ternary Mn–Zn-Al structures have been reported, without full crystallographic data available, the decagonal $Mn_3Zn_2Al_{11}$ (oS152) and icosahedral Mn_5ZnAl_{24} (oS*) which are two quasicrystalline compounds [15, 16, 17]. In the Mn−Zn system a cubic γ-brass has been proposed based on PXRD and EDS without any specific crystallographic or decoration information [18] and in previous work was shown to be Ni_2Zn_{11}-type [1]. The other Mn–Zn binaries shown in green, are MnZn and $Mn_{3.4}Zn_{0.6}$ [19, 20]. In Figure 4.1 the possible phase width, based on the observed phase widths of the endpoints, of a structural transition between the two known γ-brasses is highlighted in pink.

An investigation of the questions of where and to what extent Zn replaces Mn and Al, what effect these replacements have on electronic structure, and what role Zn plays in the bonding as the structure transforms from cubic to rhombohedral are discussed herein. We report the designed synthesis, structural characterization, and electronic structures highlighting the transition from the reported rhombohedral Mn_5Al_8 (hR78) γ-brass to the cubic $Mn_{2+x}Zn_{11-x}$ (cI52) γ-brass as a function of VEC [2, 9].

Experimental Methods

Synthesis

Elemental Mn (99.999% Mn, MPC), Zn (Ames Laboratory, 99.999%, Zn teardrop), and Al, (MPC, Ames Laboratory, Al teardrops 99.9999% MPC-Ames) were individually

weighed for a total mass of ~ 0.5g, sealed under argon in a Ta ampoule, and encapsulated under vacuum in fused silica jackets. The samples were heated at rates of 0.5-2 °C per minute to maximum temperatures of 800-850 °C, held for 12-24 hours at the maximum value then cooled at a rate of 0.1°C per minute to 400-500 °C to anneal for 7-10 days, from which samples could cool to room temperature naturally. For samples created using a Zn self-flux, 0.1 to 0.2 g excess Zn was added to the 0.5g of measured Mn, Zn, and Al and placed in a Canfield crucible with a frit and packed in an evacuated silica jacket using quartz-glass wool. The flux-grown samples followed the previously mentioned heating scheme except the ampoules were inverted and centrifuged at the annealing temperature allowing the excess Zn to be removed from the grown crystals. All products are visibly air stable and non-reactive to humidity.

To create the referenced binary Mn_5Al_8 γ-brasses, Thimmaiah et al. used a 4:1 Sn flux. The surface oxide layer on Mn was removed by etching with dilute HCl (5M) followed by drying with acetone. Alumina crucibles with stoichiometric loadings were sealed in evacuated silica tubes, which were heated continuously from ambient temperature to 800°C at a heating rate of 30°C/ hr and held there for 12 hours. The reaction mixtures were then cooled to 650°C at a cooling rate of 30°C/hr at which point the samples were equilibrated for 96 hours. The excess Sn (flux) was removed by centrifugation at 650°C [2]. This process created a phase width from $Mn_{4.6+x}Al_{8.4-x}$ (x = 0.0 − 2.9).

Phase Analysis.

Once samples were removed from their respective vessels, they were crushed into fine powders for characterization by PXRD and larger chunks were cracked to create crystals for analysis by SCXRD. For phase identification, all samples were characterized by PXRD using a Stoe Stadii P diffractometer using a transmission geometry with Cu $K_{\alpha 1}$ radiation (λ =

1.5406Å). The scattered intensity was recorded as a function of Bragg angle 2θ. Phase

identification was accomplished, and lattice parameters were determined using Werner's

algorithm in WinXPOW [21] on ground samples from peaks within the 2θ range of 10° - 90°.

Structure determination.

Several crystals selected from different loadings and heating schemes were studied

with a Bruker Apex CCD diffractometer equipped with graphite monochromatized Mo $K_{\alpha1}$

radiation. Individual crystals were mounted on the tips of glass fibers for room temperature

data collection. Data were collected over full spheres of reciprocal space by taking multiple

sets of 600 frames with 3.0° scans in ω and exposures of 10-20 seconds per frame. The

collected 2θ range extended from 3° to 62°. SMART software was used for data acquisition.

The structural models discussed below were obtained by direct methods and refined by full

matrix, least squares refinement on F^2 using the ShelX package [22]. All structural

depictions were created with the DIAMOND [23] software package.

Computational Methods

Tight-Binding Linear-Muffin-Tin Orbital with the Atomic Sphere Approximation

(TB-LMTO-ASA) [24] is a first principles calculation technique which was used to

compute the electronic structure of models of the experimentally determined atomic

structure. This computational approach uses an approximate set of wave functions based on

the linear superimposition of atomic orbital-like functions. Real space is divided into

overlapping Wigner Seitz (WS) spheres around each atomic site and sphere overlap is

prevented from exceeding 16 percent. If necessary, any remaining space is accounted for by

empty WS spheres. For calculations of ternary compositions, empty spheres were employed

including models with rhombohedral lattices and 26-atom clusters colored with I-43m

symmetry, as well as cubic lattices with 26-atom cluster decoration yielding R3m symmetry.

The percent overlap for rhombohedral structural models was restricted to 8.590-8.653 % and the percent overlap for cubic structural models was 8.944-9.169 % for ternary and binary models. For Mn a basis set *4s/4p/3d* was used and the WS radii were 1.482-1.524 Å; for Al a basis set of 3*s*/3*p* was used with WS radii of 1.473-1.563 Å; and for Zn basis sets of 4s or 4*s*/*3p/3d* were used depending on whether Zn 3*d* orbitals were included and the WS radii were 1.390-1.455 Å.

The cutoff for convergence was set to $1x10^{-4}$ eV. A mesh of 91 ***k***-points was used in the irreducible wedge of the first BZ to obtain all integrated outcomes. Experimental atomic positions derived from SCXRD were used to produce the Density of States (DOS), Crystal Orbital Hamilton Population (COHP), band diagrams, and total energy calculations. A comparison of the Integrated Density of States (IDOS) was employed to investigate trends in shifting electron density for different crystallographic sites.

Vienna Ab-initio Simulation Package [25-28]

Vienna Ab-initio Simulation Package is a first principles calculation method used to optimize structure, perform charge density calculations, and calculate total energies. VASP uses pseudopotentials or projector augmented wave methods and a plane wave basis set with the local density approximation to calculate electronic structure. The energy cut off was 500.00 eV. Reciprocal space integrations were performed over a 3x3x3 Monkhorst ***k***-points mesh [29]. The Blochl description of PAW potentials is a more accurate method for describing the behavior of valence electron waveforms allowing analysis based on an orbital description. Experimental atomic positions derived from SCXRD were used as input to perform structure relaxations.

Data and Results

The Mn_5Al_8 structure documented by Thimmaiah et al. can be described as a Cr_5Al_8-type γ-brass [2]. Variants of this structure form in the $Au_{5-x}Zn_{8+y}$ and $Cr_{1-x}Fe_xGa$ systems [30, 31]. The mixing schemes revealed in those systems show the versatility of the structure and the intricacies of potential bonding interactions to explore computationally. Where the $Au_{5-x}Zn_{8+y}$ and $Cr_{1-x}Fe_xGa$ systems adopt a rhombohedral lattice, the binary V_5Al_8 adopts a cubic decoration and lattice [32]. Using the conventional electron counting scheme discussed earlier Mn_5Al_8 and V_5Al_8 have the same *e/a* ratio because both Mn and V provide zero valence electrons. However, by considering the partially filled *d*-band, there is a lower total number of total *e/f.u.* associated with the cubic V_5Al_8 than the rhombohedral Mn_5Al_8 [32, 2]. As discussed in previous work, $Mn_{2+x}Zn_{11-x}$ γ-brasses exists with an observed phase width where x = 0.06 – 0.60 [1]. The OT and OH sites are mixed between Mn and Zn with the OT being majority Mn and the OH majority Zn. The remaining sites are 100% occupied by Zn. There is very little deviation in lattice parameters across this phase width due to similarities in atomic radii as well as small variation in the composition of each mixed site. The following discussion will show how the hR78 Mn_5Al_8 structure transforms under systematic substitution of Zn for Al to a ternary cI52 binary.

Single crystal x-ray diffraction results

Single crystal refinements of multiple crystals were taken from various compositions along the systematic doping of Mn_5Al_8 with Zn to create the series of compounds which are listed in Table 4.1. The ternary compounds were created using a Zn flux while controlling the Mn:Al molar ratio at stoichiometric values. The SCXRD refinements do not perfectly match the stoichiometric loading ratios of Mn to Al due to secondary phases forming with Zn and in some cases the Ta ampoule. As Zn was added, the ratio of lattice parameter a/c

increases only slightly, and due to the replacement of Mn and Al the refined *e/a* values

increase as Zn, with two valence electrons, replaces Mn which contributes zero valence

electrons. As a more significant fraction of Al is substituted by Zn, the *e/a* ratio decreases

until all Al has been replaced by Zn. In Table 4.1 the crystallographic data of select single

crystal and powder data are listed. SCXRD data refined from a sample determined to be

multiphase by PXRD are available in the Supporting Information.

Table 4.1: Compositions, phase analysis, lattice constants, and refined composition for γ-brasses in $Mn_{5-y}Al_{8-x}Zn_{x+y}$

Loading Composition	Phase(s) present (PXRD)	S.G.	Lattice parameters	Refined Composition	*e/a* **
$Mn_{4.55}Al_{8.45}$ *	γ-brass, Mn_4Al_{11}, Sn	R3m	a= 12.6740(4) Å c=7.9461(3) Å α= 90°, γ=120°	$Mn_{4.76(2)}Al_{8.24(2)}$	1.90
$Mn_{6.50}Al_{6.50}$ *	γ-brass, Sn	R3m	a= 12.6548(3) Å c=7.9457(2) Å α=β=90°, γ=120°	$Mn_{5.9(2)}Al_{7.1(2)}$	1.64
$Mn_{7.15}Al_{6.85}$ *	γ-brass, Sn	R3m	a= 12.6012(5) Å c=9311(3) Å α=β=90°, γ=120°	$Mn_{6.2(2)}Al_{6.8(2)}$	1.56
$Mn_5Al_7Zn_1$	γ-brass	R3m	a=12.731(7) Å c=7.927(5) Å α= 90°, γ=120°	$Mn_{4.51(1)}Al_{7.49}Zn_1$	1.88
$Mn_5Al_7Zn_1$	γ-brass	R3m	a=12.637(6) Å c=7.948(3) Å α= 90°, γ=120°	$Mn_{4.58(2)}Al_{7.65}Zn_{0.76}$	1.88
$Mn_5Al_5Zn_3$	γ-brass	I-43m	a=9.079(3) α= 90°	$Mn_{4.88(2)}Al_{4.80}Zn_{3.32}$	1.62

* Data provided by Thimmaiah et al. All lattice parameters were refined via SCXRD
** Refined *e/a*

Structure determination

The observed shift in lattice parameters from SCXRD refinements is also observed in the γ-brass component of the experimental PXRD patterns and can be seen in the theoretical PXRD patterns in Figure 4.2. As 1 atomic equivalent of Zn is incorporated into the R3m unit cell, peak splitting is less pronounced and the peak shifts support the doping of a larger element, Zn, into the structure, expanding the lattice parameters. At compositions loaded as $Mn_5Al_{8-x}Zn_x$ (x = 3 – 5), the PXRD pattern quality was limited by the simultaneous formation of rhombohedral and cubic crystals as well as secondary phases. Figure 4.3 shows the highest quality PXRD patterns from stoichiometrically loaded samples in the $Mn_5Al_{8-x}Zn_x$ (x = 1 – 7) systematic doping. In this range theoretical PXRD patterns were generated from the few quality crystals isolated from the bulk samples of $Mn_5Al_7Zn_1$ and $Mn_5Al_5Zn_3$ as well as the Mn–Al binary γ-brass (red) [2] and the Mn–Zn binary γ-brasses (blue) [1] in Figure 4.2.
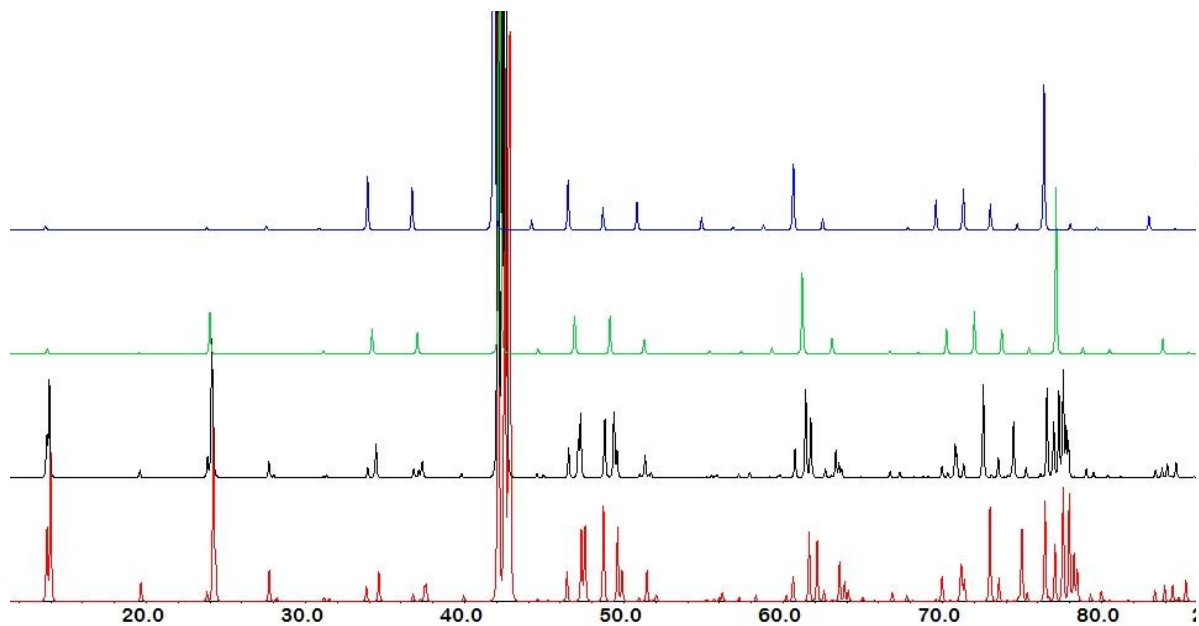
Figure 4.2: Theoretical PXRD patterns determined from SCXRD of mixed phase and pure phase samples (from top to bottom) with refined compositions $Mn_{2.33}Zn_{10.67}$(blue), $Mn_{4.96}Al_{4.82}Zn_{3.22}$ (green), $Mn_{4.51}Al_{7.49}Zn_{1.00}$(black), and $Mn_{5.1}Al_{7.9}$ (red)
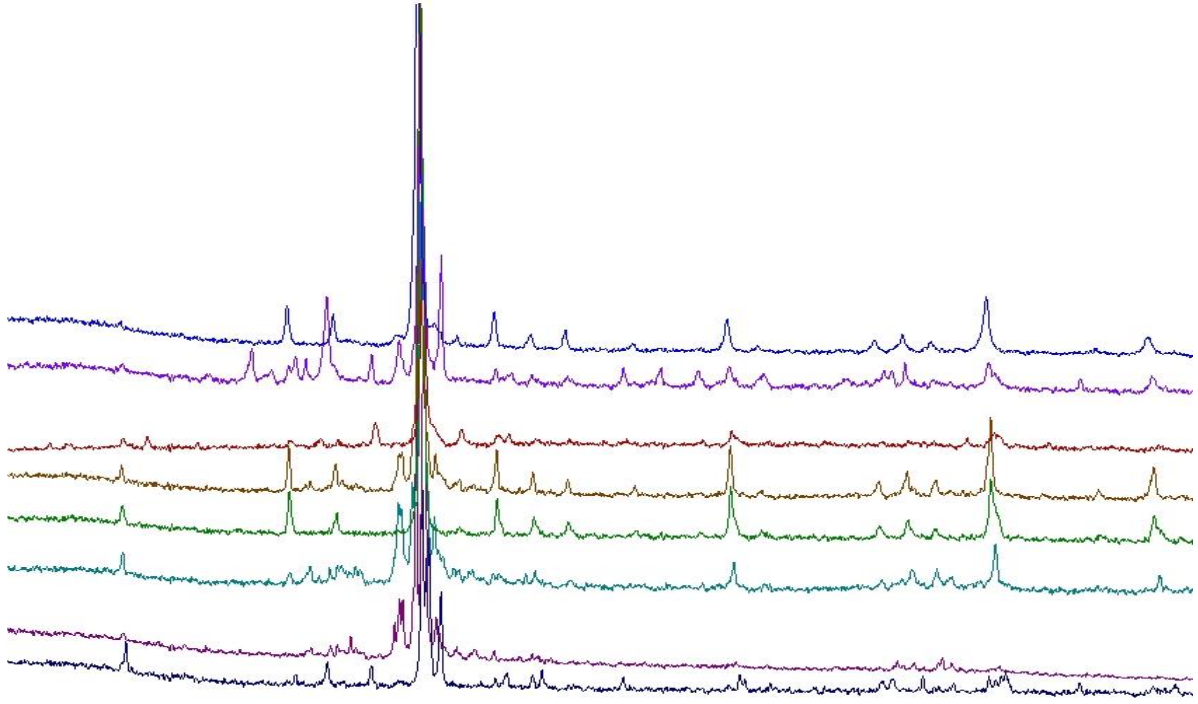
Figure 4.3: Experimental PXRD patterns from bulk samples (from bottom to top) loaded at compositions Mn_5Al_7Zn, $Mn_5Al_6Zn_2$, $Mn_5Al_5Zn_4$, $Mn_5Al_4Zn_4$, $Mn_5Al_3Zn_5$, $Mn_5Al_2Zn_6$, and Mn_5AlZn_7

Structural trends
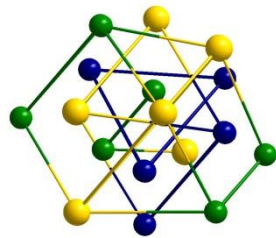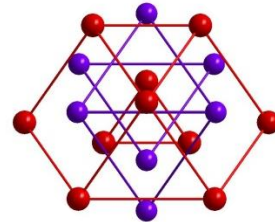
(a)   (b)

Figure 4.4: Representative 26-atom clusters of endpoints in the transition from (a) $Mn_{5-y}Al_{8-x}Zn_{x+y}$ to (b) $Mn_{2+x}Zn_{11-x}$. Where Al atoms are represented in yellow, Mn atoms in blue, Zn atoms in red, with green and purple consisting of mixed composition.

Breaking down complex intermetallic compounds into repeating structural units can make obvious their distinctive structural and bonding features. The 26-atom clusters at the endpoints of this transition can elucidate the distortion along the body diagonal observed experimentally. Shown in Figure 4.4(a), the top and bottom planes of each cuboctahedron

are non-parallel in the rhombohedral unit cell, 4.4(b), whereas, in the cubic unit cell, planes of the cuboctahedron, octahedron, and tetrahedra are parallel. The decoration of each 26-atom cluster, as well as the structural arrangement, is reflected in the space group of each unit cell. In the rhombohedral case, the inner and outer tetrahedra, as well as the octahedron, are split into two Wyckoff sites while the outermost cuboctahedron shell is split into three Wyckoff sites. For the cubic cases, all sites in each shell are constituents of the same Wyckoff site.

Elemental distribution across $Mn_{5-y}Al_{8-x}Zn_{x+y}$ γ-brasses

Thimmaiah et al reported a phase width for the Mn_5Al_8 γ-brasses. As shown in Table 4.2, the composition in the OT shell remains constant, and the OH and CO shells the minority component of Mn increased as overall Al content decreases.

Table 4.2: Elemental Distribution across $Mn_{5-y}Al_{8-x}Zn_{x+y}$ γ-Brasses

Refined Composition	Wyckoff sites								
	3a-IT(1)	9b-IT(3)	9b-OT(3)	3a-OT(1)	9b-OH(3a)	9b-OH(3b)	9b-CO(3a)	9b-CO(3b)	18c-CO(6)
$Mn_{4.76}Al_{8.24(2)}$	Al	0.51(2)Mn 0.49 Al	Mn	Mn	Mn	0.04(2)Mn 0.96Al	0.28(2)Mn 0.72 Al	Al	Al
$Mn_{5.10}Al_{7.90(2)}$	Al	0.59(2)Mn 40.8 Al	Mn	Mn	Mn	0.08(1)Mn 0.92 Al	0.39(2)Mn 0.61Al	Al	Al
$Mn_{6.32}Al_{6.68(2)}$	0.14(2) 0.86	0.87(2) Mn 0.13 Al	Mn	Mn	Mn	Al	0.67(2)Mn 0.33 Al	0.16(2)Mn 0.84 Al	0.07(2) Mn 0.93Al
$Mn_{4.51(1)}Al_{7.49}Zn_1$	Al	0.315(1) Al 0.685 Mn	Mn	Mn	Mn	0.715(1) Al 0.285 Zn	0.813(1) Al 0.187 Zn	0.819 (1)Al 0.181 Zn	Al
	8c-IT		8c-OT		12e-OH		24g-CO		
$Mn_{4.88(2)}Al_{4.80}Zn_{3.32}$	0.706(2) Al 0.294 Zn		Mn		0.997(2) Mn 0.003 Zn		0.575(2) Al 0.426 Zn		
$Mn_{2.33(1)}Zn_{10.67}$	Zn		0.79(1) Mn 0.21 Zn		0.21(1) Mn 0.79 Zn		Zn		

SOF uncertainties are included in SI tables

In the IT shell, 100% Al site is replaced with a minority Mn component and a Majority Mn site increases its majority. Mn is introduced to all polyhedral shells throughout the phase width. Table 4.2 also displays the elemental distribution from the substitution series according to crystallographic sites and shows the first sites that Zn occupies are the

majority Al OH(3b), CO(3a), and CO(3b) sites Once the lattice becomes cubic Zn incorporates into the OT and OH sites which are Mn majority sites and the last Al remains on the mixed Al/Mn sites of the IT shell. The OT positions are always 100% occupied by Mn atoms in the binary and ternary hR78 γ-brasses, which is also true for γ-Cr_5Al_8, in which Cr atoms occupy the OT positions [2]. Thimmaiah et al refined a γ-brass with composition $Mn_{6.32}Al_{6.68}$, however lowering the Al to that extent puts the *e/a* ratio near 1.54 which is below what is normally accepted for hR78 γ-brasses, therefore, the systematic substitution of Zn was started from a stoichiometric loading near the $Mn_{5.10}Al_{7.9(2)}$ refinement. The $Mn_{6.32}Al_{6.68(2)}$ composition would not provide significant insight into the observed structural transition $Mn_{5-y}Al_{8-x}Zn_{x+y}$ and will not be investigated computationally, as part of the binary Mn–Al γ-brasses.

Electronic structure

In cases such as the systematic doping of $Mn_{5-y}Al_{8-x}Zn_{x+y}$ (x = 0 − 8), the experimental results can be limited by poor quality PXRD and twinned SCXRD results. A computational investigation can shed a light on the hidden bonding interactions and provide context to multiphase PXRD patterns through analysis of multiple coloring models, total energy and structure optimization.

The Rigid Band Model

In order to utilize the COHP and DOS to investigate off-stoichiometric compositions, the Rigid Band Model (RBM) can be employed. RBM is often sufficient in explaining the alteration of *e/a* in electronic structure diagrams, however, in the following models, it does not fit perfectly. The basic assumption for RBM is that the shape of the DOS does not change drastically with small changes in composition. The general shapes of the "$Mn_{10}Al_{16}$" and "Mn_7Al_{19}" models in Figures 4.5.4.2.1 and 4.5.4.2.2 are significantly different, making

the application of RBM to binary Mn-Al γ-brasses limited. In the ternary models, an additional limitation is apparent. Depending on the nature of the Zn substitution, that is, either into the Mn or Al occupied sites, the basis sets used for the Mn and Al determine if the *d* orbitals of Zn are active at the site. The *e/a* will increase when a 12-electron Zn (4s/3d) replaces a 7-electron Mn (4s/3d) and will decrease when 2-electron Zn (4s) replaces 3-electron Al (3s/3p). Therefore, RBM must be applied with care in the analysis of all coloring models used in the $Mn_{5-y}Al_{8-x}Zn_{x+y}$ γ-brass investigation. In CMAs such as the γ-brasses, a pseudogap is often generated by the interaction of nearly free electron states at the Fermi surface. To create an energetic driving force for stability the phenomenon of a Fermi Surface Brillouin Zone induced pseudogap must be sufficiently deep [32]. The width and location of this pseudogap serves as a justification for an experimentally observed phase width in the following analyses.

Binary Mn–Al γ-brasses

In the binary rhombohedral refinements shown in Table 4.1, the multiple Mn–Al mixed sites create a need for computational models to understand the Mn_5Al_8 γ-brass and determine the most likely location for Zn to appear first. The three mixed 9b sites offer different local atomic environments to investigate the driving force in Zn substitution. The Mn-rich Mn_5Al_8 γ-brass can be modeled by a cluster with composition "$Mn_{10}Al_{16}$" and the Al-rich Mn–Al γ-brasses can be modeled by a cluster with the composition Mn_7Al_{19} based on the majority occupation of mixed sites in the $Mn_{4.76}Al_{8.24(2)}$ refinement.

The six models used to study the mixed sites of the Mn–Al γ-brasses are shown in Figure 4.5 which show energy relative to coloring "A", the lowest energy decoration for "$Mn_{10}Al_{16}$" and "D" the lowest energy coloring for "Mn_7Al_{19}". "A" is derived from the majority component of each mixed site as determined by SCXRD refinement. The CO shell

is comprised of only Al and the IT shell is comprised of three Mn atoms and one Al atom. In "B" and "C" the Mn is moved from the IT(3) site to either CO(3a) or CO(3b). Figure 4.5.4.1.1 shows 26-atom clusters, from possible Al-rich Mn–Al γ-brasses. Coloring "D" is the lowest in energy which indicates having the IT fully occupied by Al and the OH half occupied by Mn is stabilizing.

"A"	"B"	"C"
0.000 eV	+0.557 eV	+0.393 eV
"D"	"E"	"F"
0.00 eV	+5.13 eV	+7.18 eV
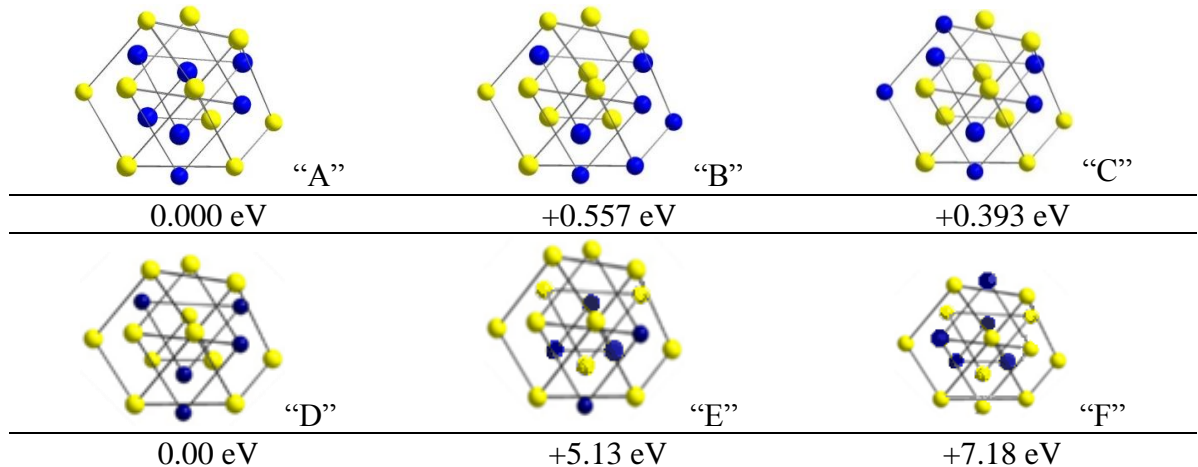
Figure 4.5: Lowest energy colorings for "$Mn_{10}Al_{16}$" and "Mn_7Al_{19}." Energies are per unit cell.

In Figure 4.6 the "$Mn_{10}Al_{16}$" DOS and COHP of coloring "A" shows an interesting feature, a narrow pseudogap at approximately 0.167 eV above the calculated Fermi level on the DOS. The composition at the line indicated in red, 0.167 eV is $Mn_{10}Al_{16}$ and at the calculated Fermi level, shown in black, the composition is $Mn_{10.60}Al_{15.40}$. In the COHP Mn–Mn contacts become antibonding at 0.60 eV below the Fermi level. The Al–Al contacts remain nonbonding from approximately 1.5 eV below the Fermi level as energy increases. Bond optimization for homoatomic interactions occurs at 104 electrons, just below E_F before Mn–Mn interactions become antibonding. Populating the Mn–Mn beyond that point, by increasing Mn content would disrupt positive, bonding interactions. "$Mn_{10}Al_{16}$" would be stabilized by decreasing Mn–Mn contact.
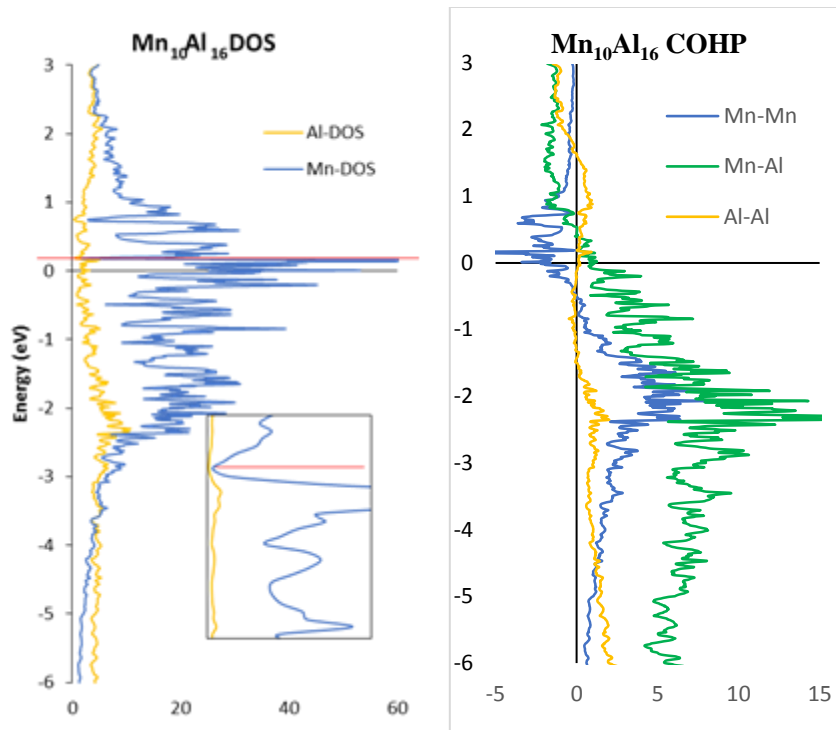
Figure 4.6: "Mn$_{10}$Al$_{16}$" DOS (left) and Mn$_{10}$Al$_{16}$ COHP (right) the black line at 0 eV indicates a composition of "Mn$_{10.60}$Al$_{15.40}$" and the red shows "Mn$_{10}$Al$_{16}$".

To model the Al-rich Mn$_7$Al$_{19}$ coloring "D" was used to generate the DOS and COHP shown in 4.7. By removing three Mn atoms from the IT(3) position in each 26-atom cluster and replacing them with Al, where the shortest bonding distances are located, a gap opens near the Fermi level significantly splitting the Mn d-band (seen in blue) at an electron count of 105 e/cluster.
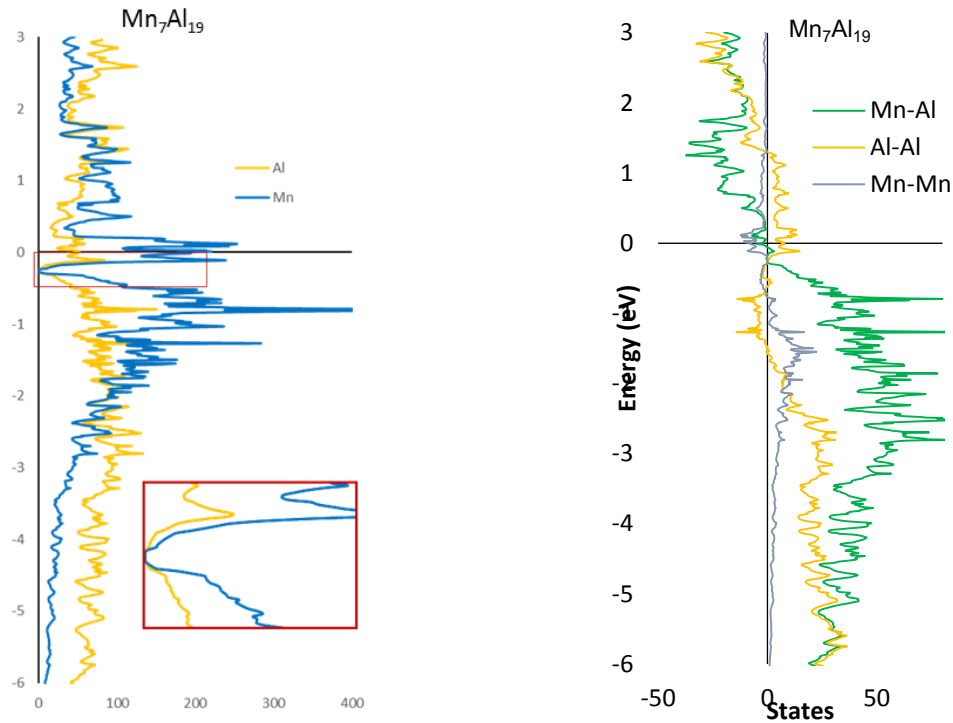
Figure 4.7: Mn_7Al_{19} DOS (left) and COHP (right)

Phase width of binary Mn–Al γ-brasses

Utilizing both the DOS and COHP curves from the "$Mn_{10}Al_{16}$" and "Mn_7Al_{19}" models the compositional phase width of Mn–Al γ-brasses can be studied. In other Group II γ-brasses such as Co_2Zn_{11}, the Fermi surface Brillouin zone interactions allow for the $3d$ band of Cobalt to be less populated near the Fermi level. In a similar way, the $3d$ electrons of Mn split near the Fermi level in the DOS forming the boundaries of the pseudogap observed [4, 32-34]. Both the DOS for "$Mn_{10}Al_{16}$" and the "Mn_7Al_{19}" are Figures 4.6 and 4.7 show pseudogaps, however, those shown in "Mn_7Al_{19}" is far more pronounced indicating there are fewer Mn–Mn (d–d) interactions. The decorations used in further computational models are arranged similarly to "Mn_7Al_{19}" [2]. The location of the gap in Figure 4.5.4.2.2 indicates that lowering the E_F to -0.24eV would reach an electron count of 105 e/cluster. The

COHP curves for "Mn_7Al_{19}" support an optimized bonding scheme at the same composition. Adding more Mn–Mn and Mn–Al interactions would cause antibonding overlap to increase and decrease the overall stability of the structure. A careful application of RBM indicates that 104 and 105 electrons per cluster is energetically favorable from the "$Mn_{10}Al_{16}$" and "Mn_7Al_{19}" models respectively. In both scenarios if a 2-electron Zn replaces a 3-electron Al, the Fermi level can shift lower by 13 electrons per formula unit in "$Mn_{10}Al_{16}$" to mark the bond optimization at "$Mn_{10}Zn_{13}Al_3$" and shift 1 electron per formula unit lower in "Mn_7Al_{19}" to the aforementioned gap and composition of "$Mn_7Zn_1Al_{18}$". This indicates that the 104 e/cluster is optimum electron count for the Mn–Al γ-brass.

Site energy and charge density

Assessing where the first Zn will go requires factoring electronegativity into the results of an IDOS/Atom calculation for individual Wyckoff sites. The differences in electronegativities between Mn, Al, and Zn based on the Pauling and Mulliken scales are subtle. Al (1.61; 1.79) is always more electronegative than Mn (1.55; 1.26) and Mn is slightly less electronegative than Zn (1.65; 1.51) [35]. Depending on the scale used Zn or Al can be the most electronegative. Because of the different basis set for each element established earlier, the following discussion will assume Mn is the least electronegative and any increase in charge can be attributed to Zn partially replacing Mn on Mn occupied sites. For Al occupied sites, a decrease in charge arises from Zn partially replacing Al.

In Table 4.3 the site energies for "Mn_7Al_{19}" and "$Mn_{10}Al_{16}$" are listed. In these calculations, Mn is considered to have seven electrons and Al is considered to have three electrons. Zn would be assigned two electrons when replacing an Al site and twelve electrons when doping into a Mn site. The IDOS values in Table 4.3 are calculated by finding the number of electrons a neutral atom at that site would contain minus the charge

calculated for that site by IDOS. Negative values indicate the site has an excess charge built up around the site and a driving force for a more electronegative, electron-rich element to occupy the site in question. Positive values show a site which has less charge relative to its neutral atom and mixing with a less electronegative element would be energetically favorable

.

Table 4.3: Charge Density Analysis of Binary Mn–Al γ-Brasses

"Mn7Al19"		"Mn10Al16"	
Location (multiplicity)	Δ IDOS/ atom	Location (multiplicity)	Δ IDOS/ atom
IT(1)	Al: (+0.206)	IT(1)	Al: (-0.244)
IT(3)	Al: (+0.219)	IT(3)	Mn: (+0.025)
OT(1)	Mn: (-0.108)	OT(1)	Mn: (-0.515)
OT(3)	Mn: (+0.008)	OT(3)	Mn: (+0.047)
OH(3a)	Mn: (-0.028)	OH(3a)	Mn: (0.008)
OH(3b)	Al: (+0.116)	OH(3b)	Al: (-0.189)
CO(3a)	Al: (+0.218)	CO(3a)	Al: (-0.194)
CO(6)	Al: (+0.150)	CO(6)	Al: (-0.204)
CO(3b)	Al: (+0.202)	CO(3b)	Al: (+ 0.633)

The Al occupied sites of "Mn7Al19" are all capable of mixing with a lower valence electron element. However, because they are the most electron-deficient, IT(3) and CO(3a) are most likely to mix with Zn, which agrees with SCXRD refinement results. Regarding Mn occupied sites, substitution is most likely to occur at OT(1). In the "Mn10Al16" model the Mn site that would be most receptive to mixing with Zn are the OT(1) and the Al site most likely to mix with Zn is the CO(3b) site. The remaining three Mn occupied sites show little variance and do not support doping with Zn or site mixing with Al. Both calculations for "Mn7Al19" and "Mn10Al16" support, in part, the refinements of Thimmaiah et al [2]. The IDOS/Atom values as well as the location of gaps and pseudogaps relative to the Fermi level in the DOS and COHP support Zn moving into the Aluminum rich CO sites and lowering the e/a from E_F to 104-105 electrons per cluster.

Bonding analysis

For the purposes of the following discussion, the maximum distance between two atoms to be considered for a bonding or antibonding interaction is 3.22 Å. The metallic radii for Mn, Zn, and Al are 1.27 Å, 1.34 Å and 1.43 Å respectively [6]. Allowing for a $\pm15\%$ range, the longest 12 CN metallic bond distance possible is 3.22 Å; only weak Al–Al contacts are found above 3.10 Å. Table 4.4 shows the breakdown of bonding interactions by element for "Mn$_{10}$Al$_{16}$" and "Mn$_7$Al$_{19}$". In both "Mn$_{10}$Al$_{16}$" and "Mn$_7$Al$_{19}$" there are no pairwise overlaps that have an overall negative ICOHP up to the Fermi level. In "Mn$_{10}$Al$_{16}$" the strongest bond type is between the Mn occupied OT(3) and the Al occupied CO(6). In "Mn$_7$Al$_{19}$" up to the Fermi level, the strongest interaction is between the Mn and Al of the OH(3a) and the CO(6). The significant decrease in Mn–Mn contact, 14.4 % to 3.2 % shows the effect of Mn 3d electron dilution and plays a role in the gap seen in the "Mn$_7$Al$_{19}$" DOS.

Table 4.4: Binary Mn–Al γ-brass Bonding by Element

Type	"Mn$_{10}$Al$_{16}$"	"Mn$_7$Al$_{19}$"
Mn–Mn	14.4 %	3.2 %
Mn–Al	68.6 %	58.5 %
Al–Al	17.0 %	38.3 %

At the opposite end of this transition, the binary Mn$_{2+x}$Zn$_{11-x}$ exists [1]. Two models "Mn$_3$Zn$_{10}$" and "Mn$_2$Zn$_{11}$" the bonding analysis for the "Mn$_2$Zn$_{11}$" and "Mn$_3$Zn$_{10}$" can be found in Chapter 3; limiting the Mn–Mn contacts, via mixed occupancy on the OT and OH sites, creates a more energetically favorable decoration [1].

Ternary Mn–Al–Zn γ-brasses

As previously discussed, the net change in *e/a* is a result of two competing processes; Zn replacing Al lowers the *e/a* while Zn replacing Mn increases the *e/a*. During Zn substitution, antibonding states are populated leading to greater electronic instability, and

eventually, a structural transition occurs. Experimentally, ternary compositions were observed in both rhombohedral and cubic lattices, and to gain insight into Zn's role in the stability or instability of each structure, multiple atomic decorations of each lattice were investigated computationally. Model "G" is built from the results of the IDOS/atom table for "$Mn_{10}Al_{16}$" where the first Zn atoms will inhabit the CO(3a) site, Al remains on the IT(3) site, and Mn occupies the entire OT and half of the OH and has cluster composition of "$Mn_7Al_{16}Zn_3$". "G" and "H" used the atomic coordinates and lattice parameters from the $Mn_{4.51(1)}Al_{7.49}Zn_1$ refinement as structural input. Models "H" and "I" represent a combination of the atomic distribution from hR78 $Mn_{4.51(1)}Al_{7.49}Zn$ and cI52 $Mn_{4.88(2)}Al_{4.80}Zn_{3.32}$, with both clusters having identical coloring distributed on different lattices. Zn occupies the IT, Mn occupies the OT and OH, and Al occupies the entire CO. "I" used atomic coordinates and lattice parameters from the $Mn_{4.88(2)}Al_{4.80}Zn_{3.32}$ refinement as structural input. The comparison of "G", "H", and "I" creates an avenue to investigate the role of Zn on the body-centered elongation near compositions where XRD data was limited. Figure 4.8 shows the relative total energy per formula unit of "$Mn_{10}Al_{12}Zn_4$" coloring applied to the rhombohedral lattice and the cubic lattice. The model with the lowest total energy per formula unit is "H" indicating that the hR78 lattice is preferred.
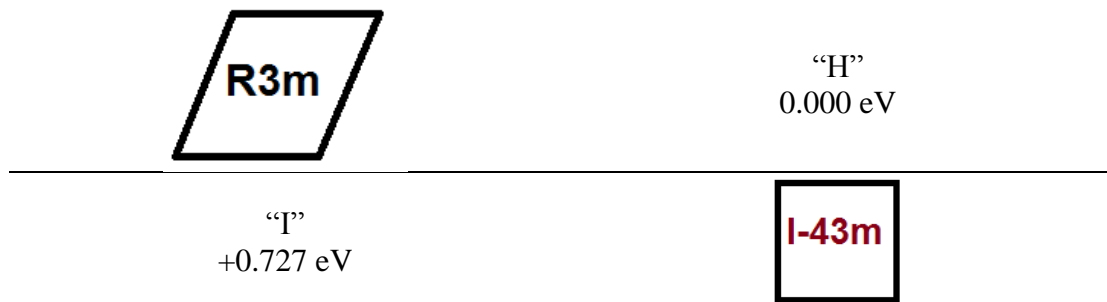
Figure 4.8: Two $Mn_{10}Al_{12}Zn_4$ models with total energies given per formula unit.
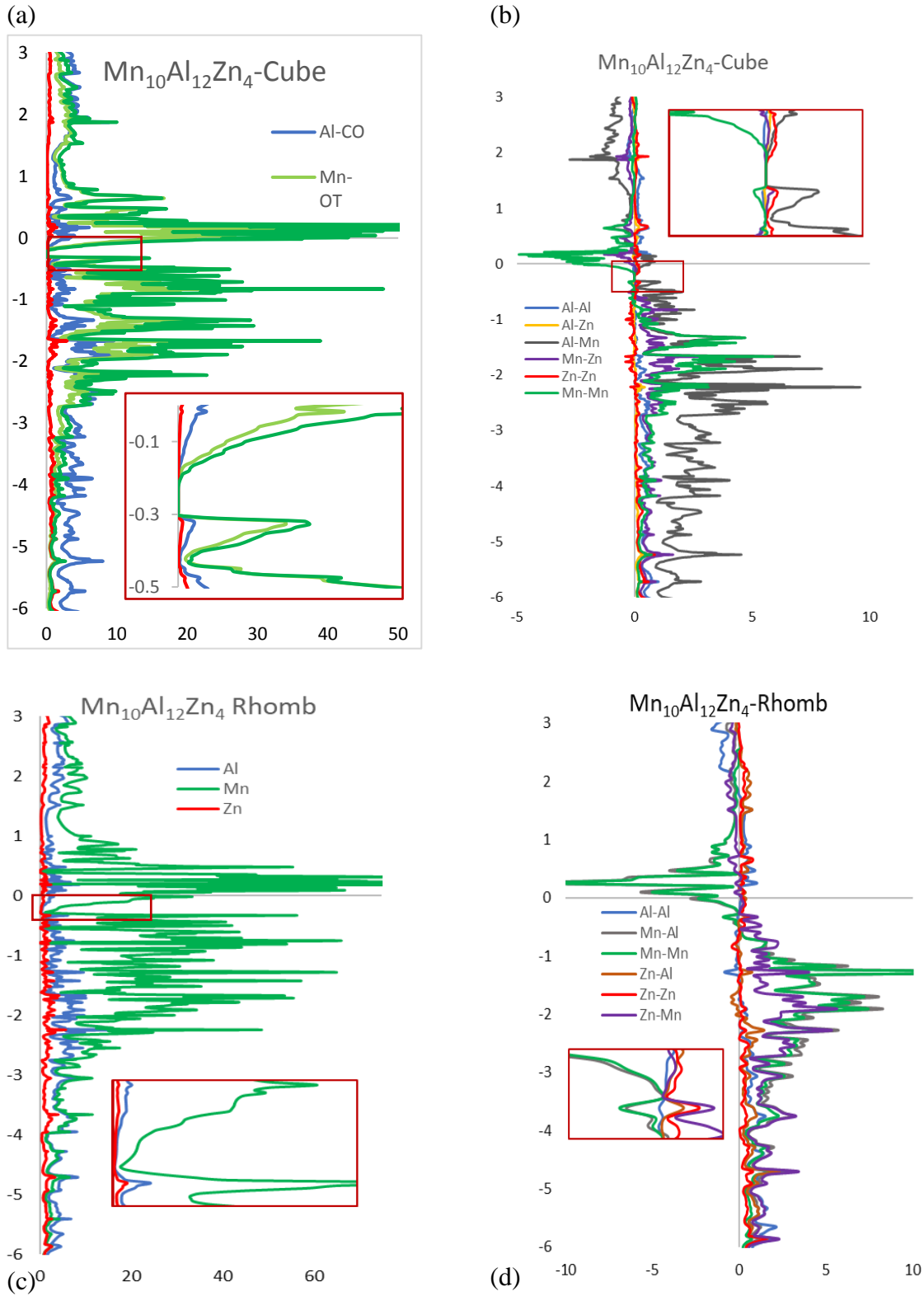
Figure 4.9: DOS and COHP for models "H" and "I (a)DOS of "I" (b) COHP of "I" (c) DOS of "H" (d) COHP of "H"

In both models "H" and "I" a gap is centered at approximately 0.28 eV below E_F. In model "H" a pseudogap is centered at 150 electrons, and in the cubic model "I" a full gap is formed at 150 electrons between -0.3 and -0.21 eV. The electronic band structure for "I" is available in Supporting information. The edges of the pseudogap in "H" are steep at the lower limit (~ -0.28 eV) and shallower approaching the upper limit (between -0.28 and -0.1 eV). In model "I" the Mn $3d$ band is pushed higher in energy to create the steep upper bounds of the gap in Figure 4.9(a). The COHP of "H" in Figure 4.9 (d) shows the Mn-Mn and Mn-Al interactions briefly become non-bonding at -0.28 eV and quickly shift antibonding, although, the Mn–Al bands in Figure 4.9 (b) do not. The edge of the Mn–Mn band shifts higher in energy to -0.2 eV before becoming antibonding and the Mn–Al COHP is positive on either side of the gap.

Table 4.5: Bonding analysis of $Mn_{10}Al12Zn4$ "H" and "I"

Type	$Mn_{10}Al_{12}Zn_4$ (hR78)	$Mn_{10}Al_{12}Zn_4$ (cI52)
Al-Al	14.14 %	14.99 %
Mn-Al	49.54 %	57.07 %
Al-Zn	6.25 %	2.25 %
Mn-Mn	16.37 %	15.21%
Mn-Zn	13.44 %	9.57 %
Zn-Zn	0.22 %	0.92%.

From Table 4.5 significant changes in bonding interactions in "H" and "I" are apparent in the Zn–Zn, Zn–Al, and the Al-Al interactions. The Zn – Zn orbital overlap increase by a factor of greater than 4.0 which suggests that IT-IT interactions are significantly affected by structural factors. The increased percent bonding attributed to Mn-Al interactions are a result of the positive interactions seen in Figure 4.9(b) compared to the negative interactions shown in Figure 4.9(d).

Table 4.6: Charge Density Analysis $Mn_{10}Al_{12}Zn_4$ (R78) and $Mn_{10}Al_{12}Zn_4$ (cI52)

$Mn_{10}Al_{12}Zn_4$ (hR78)		$Mn_{10}Al_{12}Zn_4$ (cI52)	
Location (multiplicity)	Element: (Δ IDOS/Atom)	Location (multiplicity)	Element: (Δ IDOS/Atom)
IT(1)	Zn: (+0.016)	IT(4)	Zn: (-0.202)
IT(3)	Zn: (+0.039)		
OT(1)	Mn: (-0.300)	OT(4)	Mn: (-0.174)
OT(3)	Mn: (-0.206)		
OH(3a)	Mn: (-0.300)	OH(6)	Mn: (-0.202)
OH(3b)	Mn: (-0.163)		
CO(3a)	Al: (+0.174)	CO(12)	Al: (+0.228)
CO(6)	Al: (+0.162)		
CO(3b)	Al: (+0.223)		

Table 4.6 shows the IDOS of models "H" and "I" from the calculated E_F. In the hR78 model the sites which are more likely to take additional Zn are the OT(1), OH(3a), and CO(3b). In the cI52 model the CO(12) site can mix with Zn to lower the accumulated charge and the OH(6) site can increase the charge density by mixing with Zn. The IDOS/Atom value in the Mn occupied OT site remains negative indicating a possible site for Zn to dope further. The Zn occupied IT sites are positive in the rhombohedral lattice and negative in the cubic lattice. This suggests that the bonding geometry of the IT shell is a factor in its ability to mix. The IDOS supports mixing observed in the SCXRD refinements discussed above. The charge density of the binary cubic $Mn_{2+x}Zn_{11-x}$ can be found in previous work [1]. The comparison of Zn occupied sites indicated that the OT and OH sites were most compatible with mixing [1].

Structural transition and relaxation

Because the rhombohedral unit cell of $Mn_{5-y}Al_{8-x}Zn_{x+y}$ γ-brasses can be thought of as a distortion along the body diagonal of the I-43m unit cell, one can redraw the cubic unit cell within the rhombohedral cell by placing the center of a 26-atom cluster at the corners of a

'pseudo-cubic' body-centered unit cell. In $Mn_{5.1(1)}Al_{7.9}$ the angles of this "pseudo-cube" are 89.03° and, as the structural transition proceeds, the angle shifts closer to 90°. This angle serves to quantitatively show the structural transition from rhombohedral to cubic. Table 4.7 lists the 'pseudo-cube' angle of select colorings.   All angles except those marked as relaxed come from SCXRD refinement.

Table 4.7: 'Pseudo-cube' Angle Across Structure Variation

$Mn_{5.1(1)}Al_{7.9}$	89.03
$Mn_{4.51(1)}Al_{7.49}Zn$	89.36°
$Mn_7Al_{16}Zn_3$ "G" – Relaxed	89.28°
$Mn_{10}Al_{12}Zn_4$ "H" – Relaxed	89.10°
$Mn_{10}Al_{12}Zn_4$ "I" – Relaxed	90°
$Mn_{4.88(2)}Al_{4.80}Zn_{3.32}$	90°
$Mn_{2.33(2)}Zn_{10.67}$	90°

When given the opportunity to change atomic position, lattice shape, and volume by employing VASP, the cubic model "I" adopted a cubic lattice, with a decreased volume (-14.7 %) and the total energy decreased by 4.76 eV/f.u.. The atomic positions relaxed, although, the movement was not significant enough to disrupt the geometry of individual shells in the 26-atom cluster. Under the same conditions model "H" maintained a rhombohedral lattice. The volume decreased by 13.1 % and the atomic coordinates moved only slightly. Most notably the pseudo-cube angle increased from 89.03° to 89.10° over the course of this structure optimization. Model "I" has a total energy per cluster 0.110 eV lower than model "H". Even with small amounts of Zn incorporating into the structure the cubic lattice is preferred. Model "G" started with the same atomic coordinates and lattice parameters as "H" and relaxed from 89.03° to 89.28° with a increase in volume of 1.21%. The incorporation of Zn anywhere in the lattice of the rhombohedral unit cell causes a

structural shift toward a cubic lattice, however placing Zn on the CO(3a) site had a more pronounced effect on the 'pseudo-cube' angle.

Conclusions

The relationship between valence electron concentration and structure has been shown both experimentally and computationally in the γ-brass $Mn_{5-y}Al_{8-x}Zn_{x+y}$ system. Lowering the valence electron concentration by substituting Zn for Al in loading compositions yields a structural transition as expected in a Hume-Rothery phase, however, competing processes allow Zn to mix into Mn occupied sites and Al occupied sites. Zn moving into Al occupied sites lowers the VEC and using the convention that Mn has zero valence electrons Zn moving into Mn occupied site increases the VEC. The net effect is a decrease in the *e/a* ratio and change in lattice and decoration near $Mn_{5-y}Al_{8-x}Zn_{x+y}$ (x = 3, 4). Structural optimizations of two identical cluster models show that small amounts of Zn promote the transformation from rhombohedral to cubic lattices. The electronic structure shows that the splitting of the Mn *d* band near the Fermi energy widens as more Zn is added to the structure diluting the Mn *d* band. This splitting also significantly increases when the structure transitions to cubic at low Zn concentrations resulting in a 0.1 eV wide gap due to pushing the Mn band higher in energy. The heteroatomic bonding which contributes heavily in both the Mn–Al binary γ-brasses as well as the Mn–Zn γ-brasses plays a prominent role in the bonding scheme of all ternary Mn–Zn-Al γ-brasses.

Acknowledgements

References

[1] S. Eveland, S. Thiminaiah, M. G. Marshall and G. Miller "Γ-brasses in the Mn-Zn system: An experimental and computational study" Journal of Solid State Chemistry, 2019, 269, 297. DOI 10.1016/j.jssc.2018.09.045 IS-J 9784

[2] Srinivasa Thimmaiah, Zachary Tener, Tej N. Lamichhane, Paul C. Canfield and Gordon J. Miller Zeitschrift für Kristallographie - Crystalline Materials, Volume 232, Issue 7-9, Pages 601–610, ISSN (Online) 2196-7105, ISSN (Print) 2194-4946

[3] U. Mizutani, Hume-Rothery Rules for Structurally Complex Alloy Phases, Boca Raton: CRC Press, 2011.

[4] A. F. Phragmen and G. Westgren, "X-Ray Studies on Alloys," *Metallwirtschaft,* pp. 380-385, 1929.

[5] M. Ellner, "The structure of the high-temperature phase MnAl(h) and the displacive transformation from MnAl(h) into Mn5Al8," *MTA,* vol. 21, no. 6, pp. 1669-1672, June 1990

[6] N. N. Greenwood and A. Earnshaw, Chemistry of the Elements, 2nd ed., Elsevier Science & Technology Books, 1997.

[7] U. Haeussermann, S. I. Simak, I. A. Abrikosov, B. Johansson and S. Lidin, "Electronically Induced Phase Transitions in Ternary Transition Metal Distannide Systems," *Journal of the American Chemical Society,* vol. 120, no. 39, pp. 10136-10146, 1998.

[8] X. Weiwe, L. Jing, V. Pecharsky and M. G. J., "Gamma brasses with spontaneous Magnetization: Atom site preferences and Magnetism in the Fe-Zn and Fe-Pd-Zn Phase Spaces," *Zeitschrift fuer Anorganische und Allgemeine Chemie,* vol. 641, no. 2, pp. 270-278, 2015.

[9] Mn_3Al_{10}: Taylor M.A., The Crystal Structure of Mn_3Al_{10}, Acta Crystallogr., Vol. 12, 1959, p 393-396

[10] $MnAl_4$: Onishi T., and Nakatani Y., Crystal structures of MnAl6 and MnAl4, Keikinzoku, Vol. 25, 1975, p 253-258

[11] $MnAl_3$: Gorichok B.O., and Vengrenovich R.D., Characteristics of the non-equilibrium crystallisation of intermediate compounds in the Al-Mn system, Sov. Non-Ferrous Met. Res., Vol. 5, 1977, p 149-152

[12] Shechtman, D. and Blech, I. and Gratias, D. and Cahn, J. W., Metallic Phase with Long-Range Orientational Order and No Translational Symmetry, Phys. Rev. Lett., 53, 20, 1894, 1951-1953 10.1103/PhysRevLett.53.1951

[13] Hansen V., and Gjonnes J., Approximants and Intermediate Stages during Transformation from a Quasicrystalline to a Crystalline Phase in an Al-Mn-Si Alloy, Acta Crystallogr. A, Vol. 52, 1996, p 125-132

[14] Rao K.K., Herman H., and Parthé E., ", The Structure of a Metastable, Trigonal Transition Phase in Quenched Aluminum-29 at.% Zinc," *Mater. Sci. Eng.,* vol. Vol. 1, pp. p 162-166, 1966,.

[15] $ZnAl_2$: Jin Y., Li C., and Yan M., The crystal structure of the X phase in the Al–Zn-Mg alloy, Mater. Lett., Vol. 13, 1992, p 115-118

[16] Singh, Alok & Ranganathan, Srinivasa & Bendersky, Leonid. (1997). Quasicrystalline phases and their approximants in Al Mn Zn alloys. Acta Materialia - ACTA MATER. 45. 5327-5336. 10.1016/S1359-6454(97)00103-1,

[17] Kontio A., and Coppens P., New Study of the Structure of $MnAl_6$, Acta Crystallogr. B, Vol. 37, 1981, p 433-435

[17] Robinson K., The Unit Cell and Brillouin Zones of $Ni_4Mn_{11}Al_{60}$ and Related Compounds, Philos. Mag., Vol. 43, 1952, p 775-782

[19] Liang J.L., Du Y., Liao C.Z., Tang Y.Y., Nong L.Q., Zheng F., and Xu H.H., Experimental investigation on the phase equilibria of the Mn-Ni-Zn system at 400 °C, J. Alloys Compd., Vol. 489, 2010, p 362-368

[20] MnZn: Nakagawa Y., and Hori T., Phase Diagram of Manganese-Zinc System, Trans. Jpn. Inst. Met., Vol. 13, 1972, p 167-170

[20] Mn3.4Zn0.6: Uchishiba H., Antiferromagnetism of γ-Phase Manganese Alloys Containing Ni, Zn, Ga and Ge, J. Phys. Soc. Jpn., Vol. 31, 1971, p 436-440

[22] WinXPOW, "version 3.0.0.11," Darmstadt Germany, 2010.

[23] SHELXTL, version 6.10, Madison, WI: Bruker AXS INC, 2000

[24] K. Brandenburg, "Diamond version 3.2k," Crystal Impact GbR, Bonn Germany, 2015.

[25] Jepsen, O.; Andersen, O.K. TB-LMTO, version 47; Max-Planck-Institut für Festkörperforschung: Stuttgart, Germany, 2000.

[26] Kresse, G.; Hafner J. Phys. Rev. B. 1993, 47, 558

[27] Kresse, G.; Hafner J. Phys. Rev. B. 1994, 49, 14251

[28] Kresse, G.;Furthmüller, J. Comput. Mater. Sci.1996, 6, 15

[29] Kresse, G.; Furthmüller, J. Phys. Rev. B1996, 54, 11169

[30] Monkhorst, H.j.; Pack, J.D. Phys. Rev. B 1976, 13, 5188

[31] K. Hyunjin, O. Gourdon, D. Gout, M. Eun-Deok, S. Thimmaiah and G. Miller, "Rhombohedrally distorted gamma brasses Cr(1-x) Fe(x) Ga," *Inorganic Chemistr,* vol. 49, no. 24, pp. 11505-10515, 2010.

[32] S. Thimmaiah and G. J. Miller, "Rhombohedrally distorted gamma-Au5-x Zn8+y phases in the Au - Zn system," *Inorganic Chemistry,* vol. 52, no. 3, pp. 1328-1337, 2013.

[33] J. Brandon, W. B. Pearson and P. W. Riley, *Acta Cryst.,* no. B33, pp. 1088-1095, 1977.

[34] Mizutani, U.; Inukai, M.; Sato, H., Philos. Mag. 2011, 91, 2536.

[36] Sato, H.; Takeuchi, T.; Mizutani, U.,Phys. Rev.B 2001, 64, 094207.

[37] J. B. Mann, T. L. Meek, E. T. Knight, J. F. Capitani and L. C. Allen, "Configuration Energies of the d-Block Elements," *J Am. Chem Soc.,* vol. 122, no. 21, pp. 5132-5137, 2000.

Supporting Information

Bonding Analysis for $Mn_{21}Al_{57}$					
Location		Elements	ICOHP	ICOHP/Contact	% bonding
IT(1)	IT(3)	Al–Al	3.30	1.10	3.94%
	OT(3)	Al-Mn	3.72	1.24	4.44%
	OH(3a)	Al-Mn	3.60	1.20	4.29%
	CO(3a)	Al–Al	3.16	1.05	3.77%
IT(3)	IT(3)	Al–Al	1.37	0.46	1.63%
	OT(1)	Al-Mn	1.53	1.53	1.82%
	OT(3)	Al-Mn	2.91	0.97	3.47%
	OH(3a)	Al-Mn	1.11	0.37	1.32%
	OH(3b)	Al–Al	2.30	0.77	2.74%
	CO(3b)	Al–Al	3.16	1.05	3.77%
	CO(6)	Al–Al	2.41	0.40	2.87%
OT(1)	OH(3b)	Mn–Al	4.36	1.45	5.20%
	CO(3b)	Mn–Al	4.76	1.59	5.68%
	CO(6)	Mn–Al	4.39	1.46	5.23%
OT(3)	OH(3a)	Mn–Mn	2.67	0.89	3.18%
	OH(3b)	Mn–Al	1.20	0.40	1.43%
	CO(3a)	Mn–Al	1.14	0.38	1.36%
	CO(3b)	Mn–Al	1.99	0.66	2.37%
	CO(6)	Mn–Al	6.15	1.03	7.33%
OH(3a)	OH(3b)	Mn–Al	1.95	0.65	2.33%
	CO(3a)	Mn–Al	2.95	0.98	3.52%
	CO(3b)	Mn–Al	1.14	0.38	1.36%
	CO(6)	Mn–Al	6.17	1.03	7.36%
OH(3b)	CO(3a)	Al–Al	1.03	0.34	1.23%
	CO(3b)	Al–Al	2.99	1.00	3.57%
	CO(6)	Al–Al	2.15	0.36	2.56%
CO(3a)	CO(3a)	Al–Al	1.27	0.42	1.51%
	CO(3b)	Al–Al	2.20	0.73	2.62%
	CO(6)	Al–Al	2.44	0.41	2.91%
CO(3b)	CO(6)	Al–Al	2.14	0.36	2.55%
CO(6)	CO(6)	Al–Al	2.20	0.37	2.62%

Table 4.5.4.2.1: Bonding Analysis for $Mn_{30}Al_{48}$					
Location		Elements	ICOHP	ICOHP/Contact	% bonding
IT(1)	IT(3)	Al–Mn	3.698954	1.23	4.6%
	OT(3)	Al–Mn	3.428662	1.14	4.2%
	OH(3a)	Al–Mn	3.609265	1.20	4.5%
	CO(3a)	Al–Al	3.182125	1.06	3.9%
IT(3)	IT(3)	Mn–Mn	2.457412	0.82	3.0%
	OT(1)	Mn–Mn	1.719773	0.57	2.1%
	OT(3)	Mn–Mn	3.571033	1.19	4.4%
	OH(3a)	Mn–Mn	1.407112	0.47	1.7%
	OH(3b)	Mn–Al	2.71999	0.91	3.4%
	CO(3b)	Mn–Al	1.255992	0.42	1.6%
	CO(6)	Mn–Al	2.749732	0.46	3.4%
OT(1)	OH(3b)	Mn–Al	4.006133	1.34	5.0%
	CO(3b)	Mn–Al	4.934824	1.64	6.1%
	CO(6)	Mn–Al	4.302834	0.72	5.3%
OT(3)	OH(3a)	Mn–Mn	2.45499	0.82	3.0%
	OH(3b)	Mn–Al	1.053198	0.35	1.3%
	CO(3a)	Mn–Al	1.173963	0.39	1.5%
	CO(3b)	Mn–Al	1.972705	0.66	2.4%
	CO(6)	Mn–Al	6.089684	1.01	7.5%
OH(3a)	OH(3b)	Mn–Al	1.606981	0.54	2.0%
	CO(3a)	Mn–Al	2.843258	0.95	3.5%
	CO(3b)	Mn–Al	1.13222	0.38	1.4%
	CO(6)	Mn–Al	5.578705	0.93	6.9%
OH(3b)	CO(3a)	Al–Al	0.659174	0.22	0.8%
	CO(3b)	Al–Al	2.669131	0.89	3.3%
	CO(6)	Al–Al	1.815803	0.30	2.3%
CO(3a)	CO(3a)	Al–Al	1.316797	0.44	1.6%
	CO(3b)	Al–Al	1.842443	0.61	2.3%
	CO(6)	Al–Al	2.018516	0.34	2.5%
CO(3b)	CO(6)	Al–Al	1.587334	0.26	2.0%
CO(6)	CO(6)	Al–Al	1.821545	0.30	2.3%

Phase data	
Formula sum	Al9.60 Mn9.77 Zn6.63
Formula weight	1229.64 g/mol
Crystal system	cubic
Space-group	I -4 3 m (217)
Cell parameters	a=9.079(3) Å
Cell ratio	a/b=1.0000 b/c=1.0000 c/a=1.0000
Cell volume	748.37(74) Å^3
Z	2
RAll	0.0097
Pearson code	cI52
Wyckoff sequence	gec2

Atomic parameters						
Atom	Wyck.	Site	S.O.F.	x/a	y/b	z/c
Al1	8c	.3m	0.7061(10)	-0.10610(3)	0.10610(3)	0.10610(3)
Zn1	8c	.3m	0.2939(10)	-0.10610(3)	0.10610(3)	0.10610(3)
Mn2	8c	.3m		0.17154(2)	0.17154(2)	0.17154(2)
Zn3	12e	2.mm	0.003(2)	0	0.35448(2)	0
Mn3	12e	2.mm	0.997(2)	0	0.35448(2)	0
Al4	24g	..m	0.5745(6)	0.03784(2)	0.30962(2)	-0.30962(2)
Zn4	24g	..m	0.4255(6)	0.03784(2)	0.30962(2)	-0.30962(2)

Phase data	
Formula sum	Al46.071 Zn4.14 Mn27.789
Formula weight	3040.45 g/mol
Crystal system	trigonal
Space-group	R 3 m (160)
Cell parameters	a=12.637(6) Å c=7.948(3) Å
Cell ratio	a/b=1.0000 b/c=1.5900 c/a=0.6289
Cell volume	1099.20(112) Å^3
Z	
Pearson code	hR26
Formula type	N5O8
Wyckoff sequence	cb6a2

Atomic parameters						
Atom	Wyck.	Site	S.O.F.	x/a	y/b	z/c
Al1	3a	3m	0.966	0	0	0.1734(10)
Zn1	3a	3m	0.034	0	0	0.1734(10)
Mn2	9b	.m	0.447	0.73932(4)	0.26068(4)	0.26085(8)
Al2	9b	.m	0.553	0.73932(4)	0.26068(4)	0.26085(8)
Zn3	3a	3m	0.005	0	0	0.6779(7)
Mn3	3a	3m	0.995	0	0	0.6779(7)
Mn4	9b	.m		0.55019(3)	0.44981(3)	0.44027(7)
Mn5	9b	.m		0.11747(3)	0.88253(3)	0.24599(7)
Al6	9b	.m	0.822	0.54966(6)	0.45034(6)	0.08670(16)
Mn6	9b	.m	0.178	0.54966(6)	0.45034(6)	0.08670(16)
Al7	9b	.m	0.422	0.25978(4)	0.74022(4)	0.09362(9)
Mn7	9b	.m	0.578	0.25978(4)	0.74022(4)	0.09362(9)
Al8	9b	.m		0.45037(7)	0.54963(7)	0.27136(18)
Al9	18c	1		0.33569(12)	0.04551(7)	0.3395(4)

Phase data	
Formula sum	Al14.98 Mn9.03 Zn1.99
Formula weight	1030.35 g/mol
Crystal system	trigonal
Space-group	R 3 m (160)
Cell parameters	a=12.731(7) Å c=7.927(5) Å
Cell ratio	a/b=1.0000 b/c=1.6060 c/a=0.6227
Cell volume	1112.67(140) Å^3
Z	3
RAll	0.043
Pearson code	hR33
Formula type	N7O10P16
Wyckoff sequence	c2b6a3

Atomic parameters						
Atom	Wyck.	Site	S.O.F.	x/a	y/b	z/c
Zn1	9b	.m	0.285(14)	0.8824(1)	0.1176(1)	0.7023(4)
Al1	9b	.m	0.715(14)	0.8824(1)	0.1176(1)	0.7023(4)
Mn2	9b	.m		0.7837(1)	0.2163(1)	0.5260(2)
Mn3	3a	3m		1	0	0.6281(6)
Mn4	9b	.m		0.8833(1)	0.1167(1)	1.0612(2)
Al5	9b	.m	0.813(10)	0.9230(1)	0.0771(1)	0.3792(3)
Zn5	9b	.m	0.187(10)	0.9230(1)	0.0771(1)	0.3792(3)
Al7	9b	.m	0.315(15)	1.0751(1)	0.1502(2)	0.8766(3)
Mn7	9b	.m	0.685(15)	1.0751(1)	0.1502(2)	0.8766(3)
Al8	18c	1		1.0375(2)	0.3303(3)	0.9586(6)
Al9	9b	.m	0.819(13)	0.7841(2)	0.2159(2)	0.8870(5)
Zn9	9b	.m	0.181(13)	0.7841(2)	0.2159(2)	0.8870(5)
Al110	3a	3m		1	0	0.1335(11)

Transition composition Total Energies	
Composition	Delta E rhomb – cubic eV
Mn12Al6Zn8	-5.17
Mn8Al12Zn6	-3.23
Mn8Al6Zn12	-0.71
Mn16Al4Zn6	-0.48
Mn10 Al12Zn4	0.012
Mn4Al12Zn10	0.27
Mn4Al10Zn6	0.41
Mn12Al4Zn10	0.57
Mn16Al6Zn4	0.77
Mn6Al12Zn8	0.92
Mn10Al4Zn12	0.98
Mn4Al6Zn16	1.04
Transition composition total energies cont.	

Mn6Al4Zn16	1.58
Mn12Al8Zn6	2.59
Mn6Al16Zn4	3.16
Mn6Al8Zn12	3.59

| Including 3d-band		Excluding the 3d-band	
$Mn_{5-y}Al_{8-x}Zn_{x+y}$ ($Mn_{5-x}Zn_x$)($Al_{8-y}Zn_y$)			
Mn 7 e	#e = 7(5-x)+12x +3(8-y) +2y	Mn 0 e	#e = 0(5-x) +2x +3(8-y) +2y
Al 3 e	#e = 35 -7x +12x+24-3y+2y	Al 3 e	#e = 2x+24-3y+2y
Zn 12 e & 2 e	#e = 59 + 5x – y	Zn 2 e	#e = 24+ 2x – y
	Eqn 1: y = 5x + (59 - #e)		Eqn 2: y = 2x + (24 - #e)
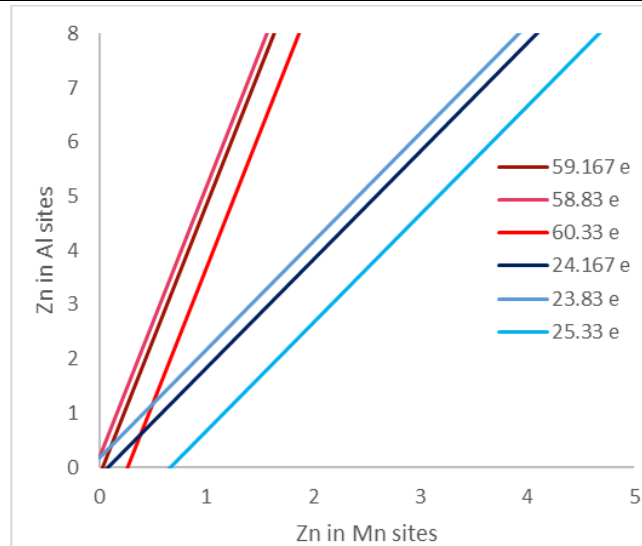
Description of the nature of Zn substitution in ternary γ-brasses. Lines in red show the plot of number of electrons which include 3d electrons in Mn sites. Lines in blue show the plots which have excluded all Mn electrons and Zn's 3d electrons. All electron counts are per formula unit.

The phase width of these ternary compositions can be plotted according to EQN 1 and

EQN 2. For the "$Mn_9Al_{15}Zn_2$" rhombohedral structure indicates 147.9-148.5 electrons could

readily form with this decoration yielding plots of y=2x-62.0 and y=5x-44.5 through y=2x-

62.3 and y=5x-44.8. The phase width suggested by the DOS and COHP of the "$Mn_8Al_{12}Zn_6$"

cubic structure suggests a stability ranges are possible in 156.1-158.4 electrons as well as

164.9-165.1 electrons (at E_F) which correlates to y=5x-48.6 and y=2x-67.2 through y=2x-66.0

and y=5x-49.7 as possible stability regions.
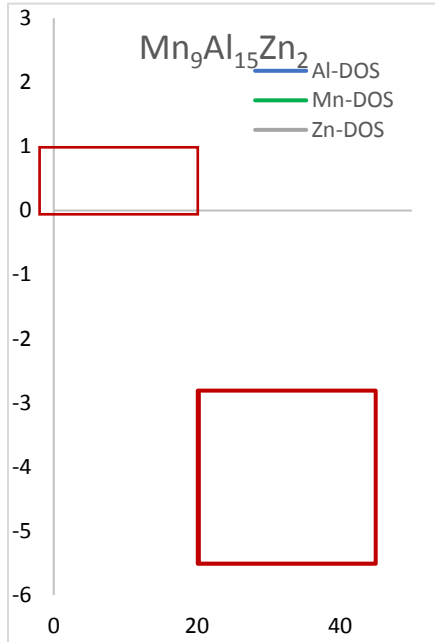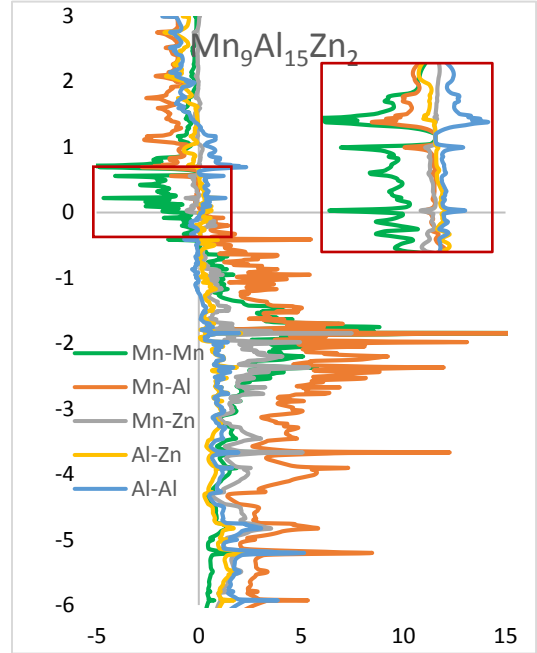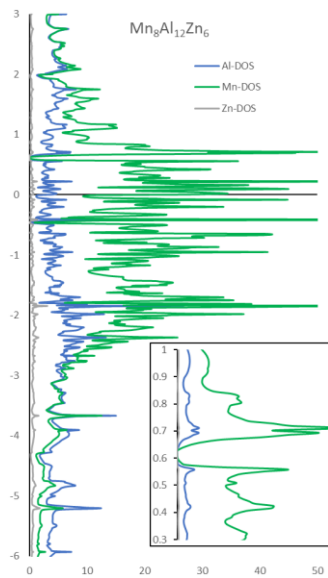
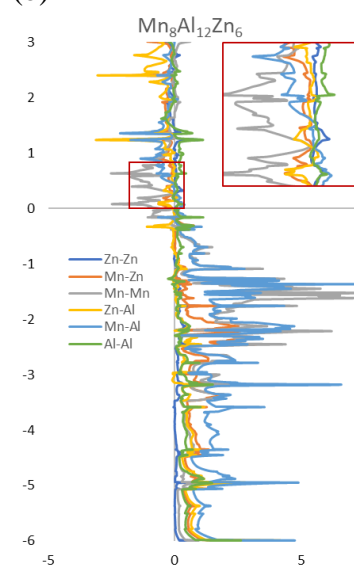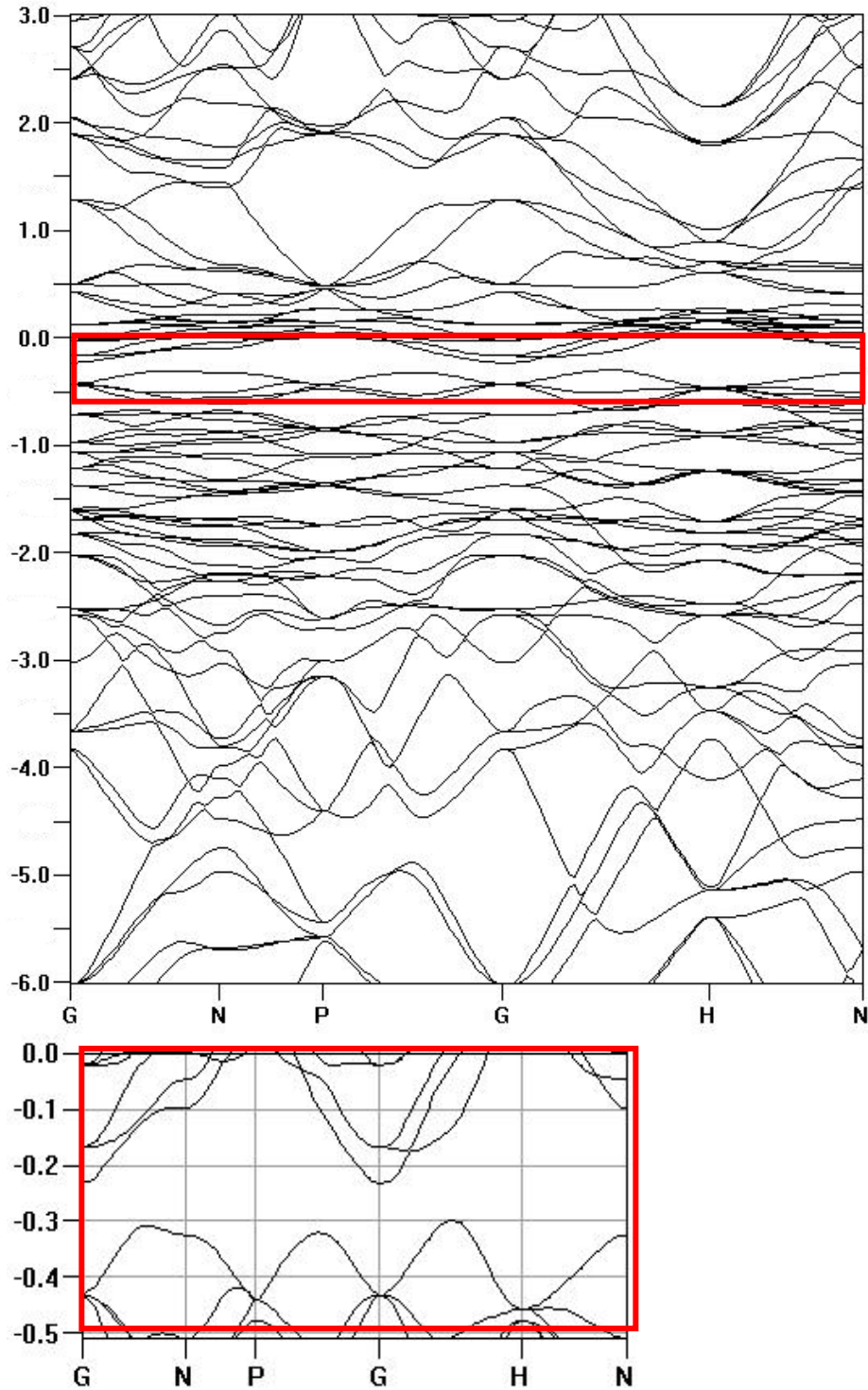COHP and DOS of the Rhombohedral, "Mn$_9$Al$_{15}$Zn$_2$" and "Mn$_8$Al$_{12}$Zn$_6$" coloring models with similar decoration to SCXRD refinements

Mn$_{10}$Al$_{12}$Zn$_4$ Band structure showing a band gap from -0.30 eV to 0.23 eV

CHAPTER 5: STUDY OF BONDING AND MIXED SITE OCCUPATION IN PRIMITIVE PACKINGS OF Γ-BRASSES VIA PROTOTYPICAL Cu₉Al₄

Stephanie Eveland[a,b*], Gordon Miller[a,b]

[a] Department of Chemistry, Iowa State University Ames, IA, USA 50011

[b] Ames Laboratory Ames, IA, USA 50011

Abstract

Results from a theoretical assessment of Cu-Al γ-brasses using first principles calculations are presented. The Cu_9Al_4 and Cu_8Al_5, an Al-rich extension of the phase width, crystalize in space groups $P\bar{4}3m$ (cP52, a= 8.7068) [1]. Atomic site occupation indicates a preference for heteroatomic overlap by separating Al atoms into two crystallographic sites, one on each 26-atom cluster in Cu_9Al_4. Primitive decoration is preferred for Cu_9Al_4 and TB-LMTO-ASA calculations show that locating the Al on the CO and IT of adjacent clusters minimizes the number and strength of Al-Al contacts in Cu_9Al_4. A comparative discussion of existing primitive γ-brasses focusing on bonding schemes and the role of VEC in stability is included.

Introduction

The sheer number of metal-metal and metal-metalloid combinations that comprise intermetallic compounds is staggering. A portion of that number can be considered complex metallic alloys, (CMAs), which have proven to be interesting systems for structural, physical property, and solid solution studies. [2] Their characteristically large unit cells can be described by packings of clusters with some manner of disorder, be it vacancies, mixed site

occupancies, or structural variations. Stability of certain 'families' of intermetallic compounds occurs at or near specific *e/a* (electron per atom) ratios. The structural dependence of a particular compound on the *e/a* ratio has been well established for Hume-Rothery phases such as γ-brasses, quasicrystals, polar intermetallic compounds, and Zintl-Klemm type compounds [3-5].
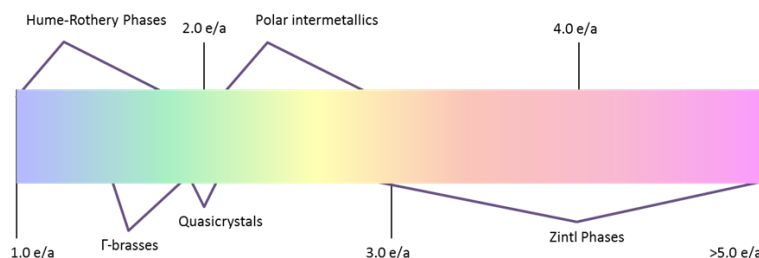

Figure 5.1: Full spectrum of structure types according to *e/a* ratios

In general, γ-brasses can be split into three groups depending on the constituent elements [6]. Group I γ-brasses have a monovalent noble metal such as Cu, Au, or Ag with a polyvalent metal or metalloid with a well-defined valency such as Al, Ga, In, or Ge. Group II examples have a partially filled 3dmetal with a fully filled d-band element (Zn or Cd) or a trivalent metal such as Al, In, or Ga; and, finally, Group III consists of cases that do not include transition metals like $Li_{21}Si_5$. [6, 7, 8] For Group I γ-brasses, the number of valence electrons assigned to each element is clearly defined making the interpretation of electronic structure calculations straightforward, and relatively more useful in comparing different compounds within Group I, than in Groups II and III.Γ-brasses exhibit large variations in atomic decoration even within individual groups. Body-centered packings of 26-atom clusters, as well as face-centered packings, are commonly observed results of atomic decoration on the 26-atom clusters [6]. The special stability of γ-brasses appears in the range of 1.5 −1.8 valence sand p electrons per atom (e/a) with the idealized e/a ratio falling at

21/13, 1.62based on the Cu$_5$Zn$_8$(I-43m, cP52) γ-brass [6]. Several prototypical decorations and structural variances have been reported within this range, the most well documented being Cu$_5$Zn$_8$, Ni$_2$Zn$_{11}$, Fe$_3$Zn$_{10}$, CrGa, Cu$_9$Al$_4$and Mn$_5$Al$_8$

109[9,10, 11, 1, 3]. The extreme ends of the *e/a* range exhibit the most noticeable structural or symmetry related variations. In the case of Cu$_9$Al$_4$, and the members of its subgroup (Au$_9$In$_4$, Ag$_9$In$_4$, and Cu$_9$Ga$_4$) [12, 13], a symmetry variation occurs resulting in primitive atomic decoration though the *e/a* ratio falls on the ideal 21/13 value. Other primitive γ-brasses are seen in Cd-rich phases, (Cd$_5$Ni and Cd$_5$Pt, cP48; Cd$_{43}$Pd$_8$, cP51) [14, 15] with varying concentrations of vacancies, which do not fall on the idealized *e/a* ratio. The Mn$_3$In (cP52) [16] variant of the Cu$_9$Al$_4$structure type has an *e/a* ratio of 0.75, due to the conventional electron counting scheme employed. I-centered, F-centered and R-centered unit cells display structural distortions in packings of the same 26-atom cluster, whereas for primitively decorated body-centered packings, there are two different 26-atom clusters labeled as "A" and "B", which is the case of the Cu$_9$Al$_4$cubic γ-brass. According toa series of diffraction studies by Arnberg and Westman, which improved upon the results of Heidenstam, Johansson and Westman, a high-quality understanding of the structural arrangement and atomic decoration was brought to the Cu$_9$Al$_4$γ-brass [1]. Al occupies the inner tetrahedron of Cluster A and the cuboctahedron of Cluster B. In the paper published by Arnberg and Westman they note that the size of the thermal parameter on the inner tetrahedron site of Cluster B indicates a likely choice for Al substitution in an Al-rich end of the phase [1]. This phase width is supported by the phase diagram reported by Murray [17] including at temperatures above 800°C, where typical Cu$_5$Zn$_8$-type is reported by De Lima et al. A γ-Cu$_{67}$Al$_{33}$, (Cu$_{8.71}$Al$_{4.29}$) [18], with space group I-43m was formed via mechanical

alloying for 100hrs from elemental Cu and Al powders, though it crystalizes poorly. It was concluded that the low temperature employed during milling causes a "slow down in reaction kinetics" which yields the I-43m structure. DSC shows that a symmetry change from P-43m to I-43m would take place within a range of 383 and 584 K and a corresponding energy change of 20.93 J/g. [18] Increasing the annealing temperature increases the disorder and the P-43m decoration forms with a higher degree of crystallinity. Synthesis and structural characterizations were not duplicated for the Cu-Al system. Previous work by Arnberg and Westman [1] was deemed satisfactory and due to the significant difference in atomic scattering factors, stoichiometric refinements of Cu_9Al_4 can be reasonably trusted. The $Cu_9Al_4\gamma$-brass has been found prolifically both as a main and secondary phase in thin-film and wire studies [19, 20, 21]. There are three questions we attempt to answer in the following work. First, what is the role of Cu–Al bonding in the stability of the atypical coloring of Cu_9Al_4 and how it differs from a body-centered coloring of the reported ht-Cu_9Al_4 across the reported phase width. Second, regarding the ht-phase, what sites are likely to mix to yield an off-stoichiometric $Cu_{8.71}Al_{4.29}$ composition [18]. Finally, does the unique geometry of clusters A and B play a role beyond the preferred Al–Al, Al–Cu, and Cu–Cu metallic bond distances? In order to achieve this goal, first principles-based electronic structure calculation methods were employed to generate DOS, COHP curves, charge density values at individual sites, and optimize the structure of averaged cluster coordinates.

Experimental Methods

Tight-Binding Linear Muffin-Tin Orbital-Atomic Sphere Approximation (TB-LMTO-ASA)[22]

Calculations of the electronic structures were performed by TB-LMTO-ASA using the Stuttgart code. Exchange and correlation were treated by the Local Density

Approximation (LDA).This computational approach uses overlapping Wigner-Seitz (WS) spheres surrounding each atom so that spherical basis functions, i.e., atomic orbital (AO)-like wavefunctions, are used to fill real space of the structure while keeping the WS sphere overlap to be less than 16 percent. If necessary, any remaining space is accounted for by empty WS spheres. The specific calculations where empty spheres were employed are listed in the Supporting Information. The percent overlap ranged between 8.526 and 9.986 % and the Cu WS radius ranged from 1.355 to1.538 Å with a basis set which consisted of 4s/4p/3d, and the Al WS radius range was 1.464-1.545 Å with a basis set which consisted of 3s/3p. Reported experimental atomic positions derived from SCXRD were used as structural input to produce the electronic density of states (DOS) and crystal orbital Hamilton population (COHP) curves, charge densities, and total energies.

Vienna Ab-initio Simulation Package VASP [23-26]

VASP is a first-principles method that uses pseudopotentials or projector augmented wave methods and a planewave basis set to build electronic structure. Electron densities are independent of crystallographic positions making it an ideal option for performing total energy calculations, structural optimizations, and charge density analyses. The Bloch description of PAW potentials is a more accurate method than the atomic sphere approximation to describe the behavior of the valence electron waveforms, allowing analysis based on an orbital description. Experimental atomic positions derived from SCXRD were used as input to determine the electron distribution through charge density analysis. Due to the different geometries of the 26-atom clusters, (A and B)the average positions of the two clusters were used as starting positions to optimize the structures of various hypothetical coloring models.

Data and Results

In the following discussion, we let cluster A and cluster B geometries refer,
respectively, to the experimentally determined coordinates of the corresponding clusters A
and B as determined by Arnberg and Westmen[1].

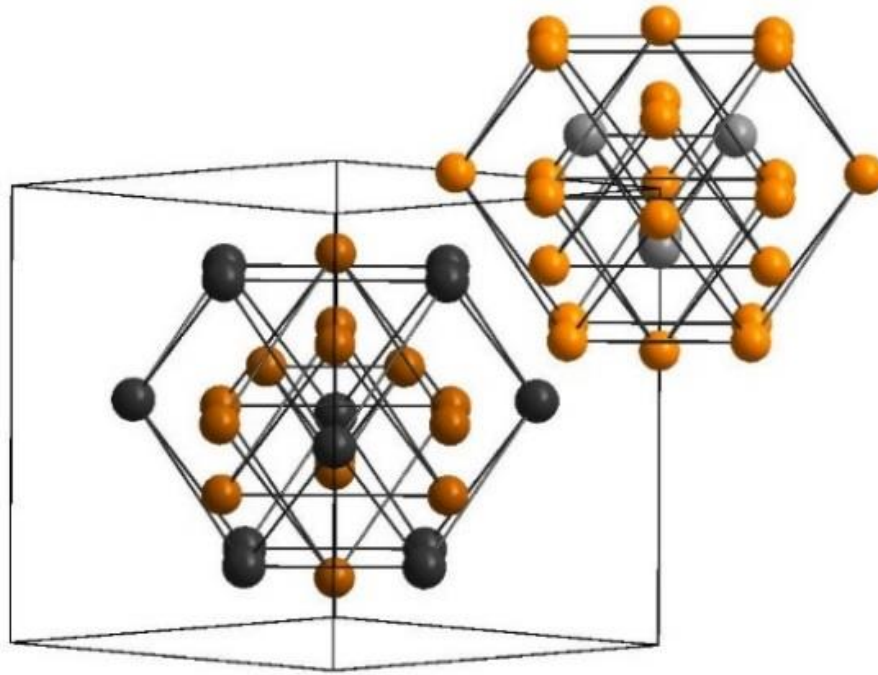Figure 5.2: Cluster A is located at the corner and Cluster B is shown at the center of the
cubic unit cell. Shades of gray indicate Al occupied sites and shades of orange indicate Cu
occupied sites.

In Table 5.1 the coordinates of the two clusters are compared to the Averaged cluster
coordinates. All calculations except those specifically marked as average cluster (AC) use
the experimentally determined atomic coordinates.

Table 5.1 Experimental Atomic Coordinates and Decoration

Cluster	Wyck.	Element	x/a	y/b	z/c
A	4e	Al	0.1157(6)	0.1157(6)	0.1157(6)
	4e	Cu	0.1704(4)	0.1704(4)	0.1704(4)
	6f	Cu	0	0	0.3553(5)
	12i	Cu	0.3153(2)	0.3153(2)	0.0322(3)
B	4e	Cu	0.6066(3)	0.6066(3)	0.6066(3)
	4e	Cu	0.3253(4)	0.3253(4)	0.3253(4)
	6g	Cu	1/2	1/2	0.8549(5)
	12i	Al	0.8113(4)	0.8113(4)	0.5332(6)
AC-A	4e		0.11115	0.11115	0.11115
	4e		0.17255	0.17255	0.17255
	6f		0	0	0.3551
	12i		0.3133	0.3133	0.0322
AC-B	4e		0.61115	0.61115	0.61115
	4e		0.32745	0. 32745	0. 32745
	6f		1/2	1/2	0.8551
	12i		0.8133	0.8133	0.5322

In Table 5.1 the coordinates of the two clusters are compared to the averaged cluster coordinates. All calculations except those specifically marked as Average Cluster (AC) use the experimentally determined atomic coordinates. Table 5.1 shows the average cluster atomic coordinates, where the geometry creates a body-centered packing of 26-atom clusters with atomic decorations either in P or I lattice symmetries.

Structural trends of related Cu_9Al_4-types and reported phase widths

In previous work γ-brasses have been simplified by looking at one 26-atom cluster at a time; however, in primitive γ-brasses the two clusters are compositionally and/or geometrically unique. VEC has been shown to explain the crystallographic arrangement of atoms, but, in the following γ-brasses the individual pairwise interatomic interactions are the driving factors in their formation. In Cu_9Al_4, as well as other isostructural examples, the composition of each cluster is different in the unit cell, and a higher number of different inter-atomic contact types exist. Whereas Ni_2Zn_{11}-types and Cu_5Zn_8 show four Wyckoff

sites, the cubic Cu$_9$Al$_4$ γ-brasses have eight sites, four for each 26-atom cluster. The number of distinct bonding interactions also is significantly increased in a P-43m structure vs the I-43m variant.
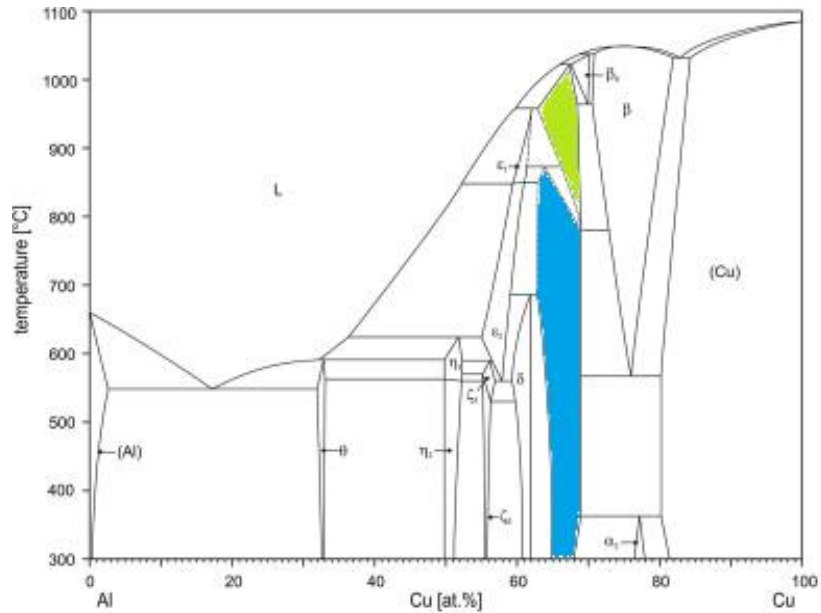

Figure 5.3: Phase diagram of Cu–Al system. [28]

The P-43m designation is not unique to the Cu-Al system; it appears in the Ag$_9$In$_4$ and Au$_9$In$_4$ γ-brasses. According to the reported phase diagrams, the phase width of Cu$_9$Al$_4$ (rt) ranges from Cu$_{8.16}$Al$_{4.84}$ – Cu$_{9.10}$Al$_{3.90}$, 63 at. % Cu to 70 at. % Cu, shown in blue in Figure 5.3, as does the high-temperature Cu$_9$Al$_4$ compound, which is reported to form in a range of 780-1025°C, shown in the bright green section in Figure 5.3. This high-temperature phase is reported to have I-43m symmetry, while the room temperature phase shows P-43m symmetry[1, 17, 18]. The most recent experimental phase diagram for the Ag-In system shows Ag$_9$In$_4$ at low temperatures, 0-300°C, and in the Au-In system the most recent experimental phase diagram shows a high-temperature Au$_9$In$_4$ which forms above 482 °C [12]. A possible reason for a high-temperature structure forming in the Au$_9$In4 system is that the size difference between the Au and In atoms no longer falls within Hume-Rothery's solid

solution rules. The relative ratio of Cu:Al, Ag:In, and Au:In are 1.12, 1.16 and 1.16 respectively. The Au and Ag ratios indicate that the size differences could play a role in decoration schemes observed at high temperatures as could the possible differences in electronegativity. Due to the importance of relative atomic radii in the stability of this phase, the following calculations will minimize expansion of the atomic overlap when utilizing TB-LMTO-ASA.

Electronic structure coloring model explanations

Figure 5.4 (A-H) shows the lowest energy coloring models for primitive and body-centered in both the experimental atomic coordinates, (A, E) and the average atomic coordinates (B, D, F, H). Models "C" and "G" use experimental coordinates but have decoration schemes which yield identically colored 26-atom clusters. Moving from the innermost ring out, the decoration of the IT, OT, OH and CO shells are shown.

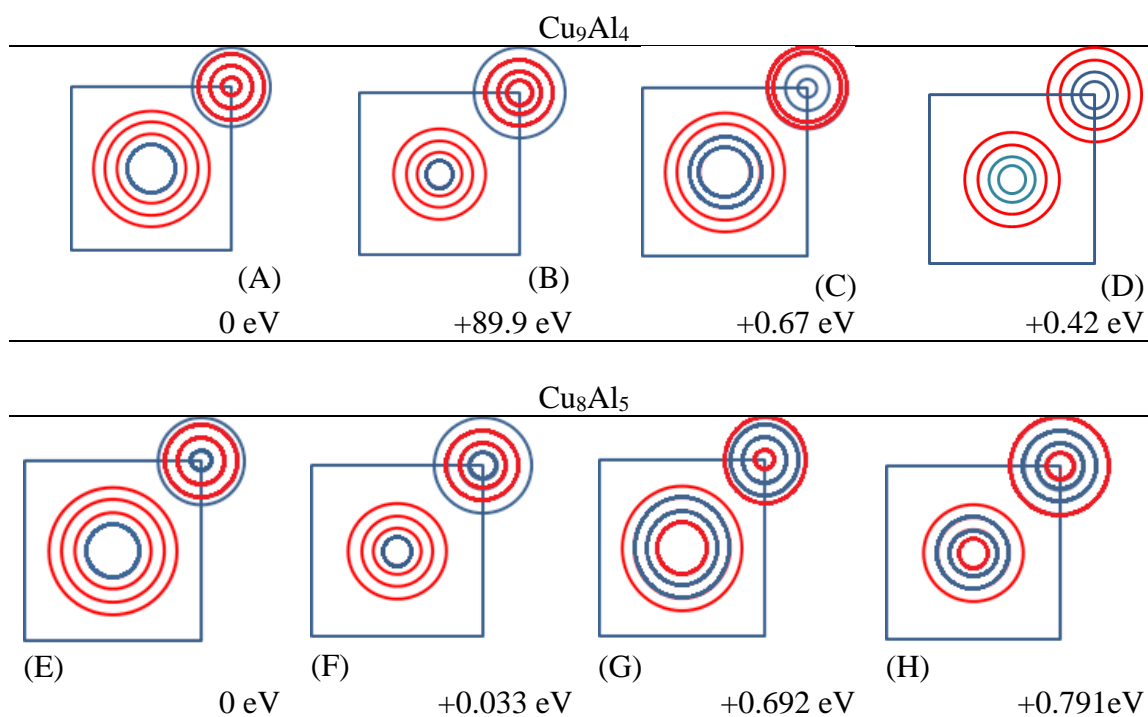Figure 5.4: Lowest energy coloring models for Cu_9Al_4 and Cu_8Al_5 (a-h) Each circle represents one of the concentric polyhedral of the 26-atom cluster. Model "B" introduces unrealistic Cu–Cu contact lengths, and is not energetically competitive.

Red circles indicate polyhedral shells occupied by Cu atoms and blue circles represent polyhedral shells occupied by Al atoms. The energies are relative to the lowest energy coloring and scaled per unit cell. The lowest energy Cu_9Al_4 structure comes from the "A" arrangement, and the lowest energy "Cu_8Al_5" structure comes from the "E" decoration.

Cu_9Al_4 primitive or body-centered?

The rigid band model (RBM) can be applied to the analysis of DOS and COHP data. The assumption that the shape of any alloy's electronic structure will not change significantly when lightly doped allows one to investigate small changes in valence electron concentration by using a single electronic structure calculation. By changing the *e/a* value, one can shift the E_F higher or lower, effectively modeling a hypothetical composition of a calculated structure. Treating Cu as having 1 valence electron and a filled soft core of 3d electrons and Al as a 3 valence-electron element implies that increasing the Cu content will lower the e/a and increasing the Al content will raise the e/a. Due to the treatment of Cu 3d band as 'soft core' mixing between Cu and Al at any site only involves s and p electrons and is straightforward using RBM. The lowest energy configuration for both the I and P decoration schemes are used in the Cu_9Al_4 and Cu_8Al_5 DOS, COHP curves and IDOS/Atom tables. The general shapes of the DOS and COHP of "A" and "C" are similar, which supports the application of RBM to the bonding comparison of Cu_9Al_4 with primitive and body-centered atomic decorations. SCXRD refinements of Cu_9Al_4 at room temperature show the IT-A and CO-B sites have full Al occupation resulting in a primitive decoration scheme, although an I-43m variant has been observed at high temperatures but is not well documented crystallographically.

Figure 5.5 shows the DOS and COHP curves for model "A" and model "C". The Cu 3d band is filled well below the Fermi level, between -6 and -2 eV, and a shallow pseudogap

can be seen in Figure 5.5 (c) between -2.5 and -1.5 whereas in (a) the shallow gap is less clear in the same region. Model "C" represents an increase in total energy of 0.67 eV/f.u, which supports the phase diagram reporting a ht body-centered variant of Cu9Al4.
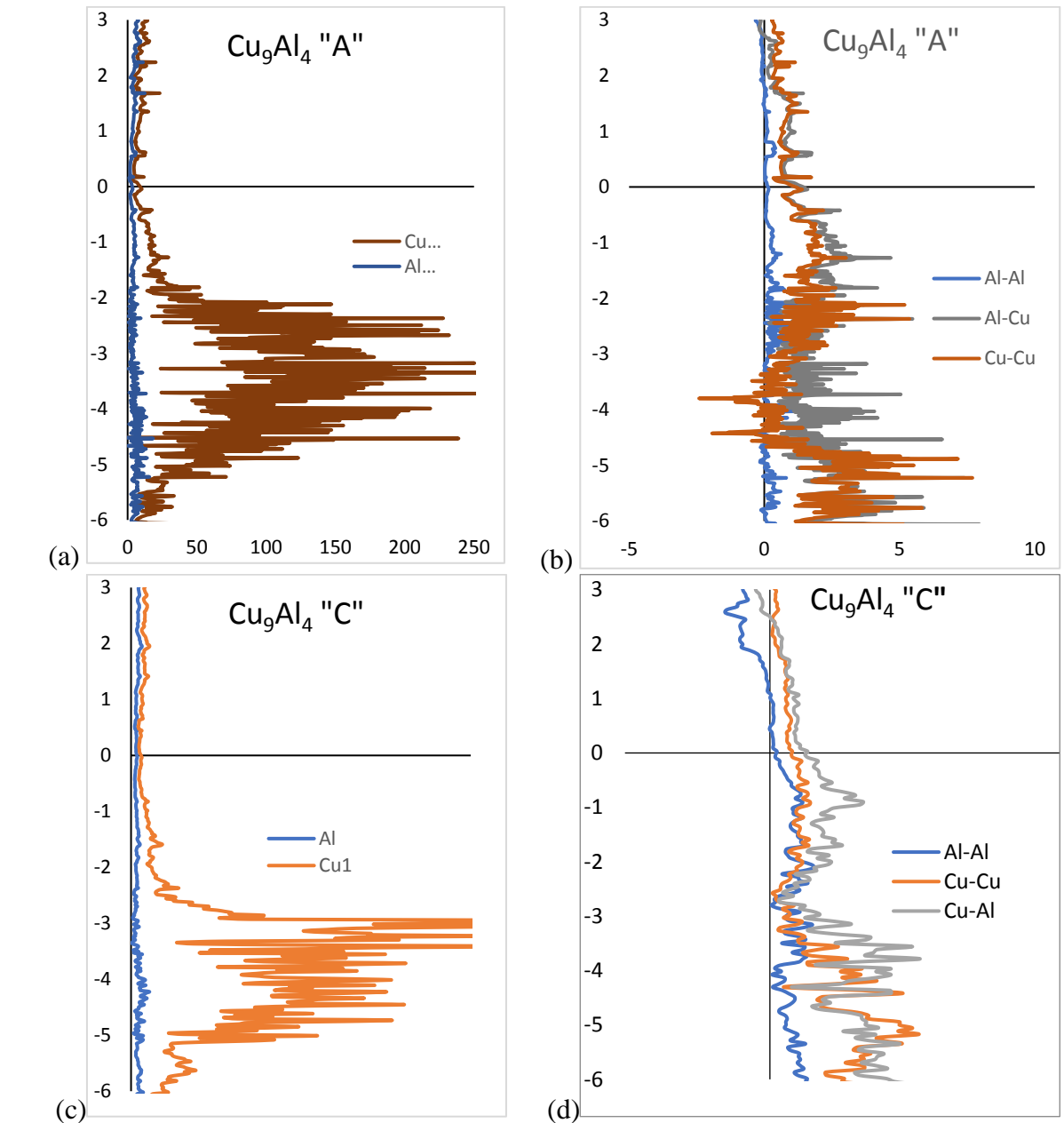

Figure 5.5: Cu9Al4 DOS and COHP using experimental coordinates. Primitive decoration are shown in (a) lowest energy model "A" DOS (b) lowest energy model "A" COHP. Body centered decoration are shown in (c) lowest energy coloring C" DOS (d) Lowest energy coloring "C" COHP. X-axes are in the same scale for COHP and for DOS.

The COHP curve of model "A", shown in Figure 5.5 (b), exhibits a peak at the Fermi level as is shown in the DOS. Shifting EF higher in energy to approximately+ 0.1 eV, on Figure 5.5 (b) to represent the incorporation of more Al moves the Fermi level into a pseudogap. In 5.5(d) the peak no longer occurs. In Figure 5.5(b) all curves remain positive or non-bonding until approximately 2 eV above the Fermi level, whereas in (d) the Al–Al interactions are non-bonding immediately above the Fermi level and Cu–Al interactions become antibonding before +2 eV. To further analyze the interactions between Cu–Al,Cu–Cu, and Al–Al contacts in Cu9Al4one can utilize the ICOHP, up to the Fermi level to determine the percent bonding of each type of pairwise interactions.

Table 5.2 lists the percent bonding in both the primitive and body-centered decorations. Bonding between Cu and Al occupied sites contributes a majority of the number of bonds and the highest percent bonding. The most significant change in bonding is the increase in contact between the Al occupied sites in the body-centered model, which comes at the expense of both Cu–Cu and Cu–Al bonding.

Table 5.2: Bonding Analysis of Cu_9Al_4 by Element

	Cu_9Al_4 (cP52)	Cu_9Al_4 (cI52)
Bond type	% Bonding	
Cu-Cu	38.03	29.01
Cu-Al	56.64	49.51
Al–Al	5.33	21.48

Phase width of primitive "Cu_8Al_5" – Cu_9Al_4

The Al-rich end of the phase width for Cu9Al4reported in the phase diagrams extends to approximately 63 at. % Cu, i.e. $Cu_{8.19}Al_{4.81}$. The DOS for both the body-centered and the primitive decorated "Cu_8Al_5"models are located in the Supporting Information. To understand how bonding differs between the body centered ht phase and the reported

primitive decoration at rt, one must investigate the phase width of the room temperature phase. The total energy for the primitive decoration is 0.67eV/f.u. lower than the body-centered decoration in Figure 5.4. A notable difference between the COHP curves for the "Cu_8Al_5"models and those of "Cu_9Al_4"is the width of the peak near the Fermi level. In the "Cu_8Al_5"modelthe Cu 3dband is more disperse and the Cu–Cu connections of the IT shell are relatively short and a marked increase in the Cu–Al connections is observed, causing the 3dband to exhibit more spikes near E_F than in the "Cu_9Al_4"models. The Cu–Al pairwise interactions increase significantly in the Al-rich models.   The Al–Al interactions become antibonding at a relatively lower energy in primitive "Cu_8Al_5"(0.83eV) than for primitive "Cu_9Al_4"(1.43eV) suggesting that increasing the Al content becomes destabilizing in the primitive decorations, which is in agreement with the reported phase diagram which suggests that the Cu-Al γ-brasses will not form with more than 37 at. % Al.

In Figure 5.6 the various COHP curves for the Al-rich "Cu_8Al_5" models are shown with body-centered decoration "G" and primitive decoration "E". These COHP curves exhibit the same slight dip between -2eV and E_F. In the cI52 coloring "G", the first class of orbital overlaps to become antibonding is Cu-Al and in the cP52 coloring, "E", Al-Al becomes antibonding first.
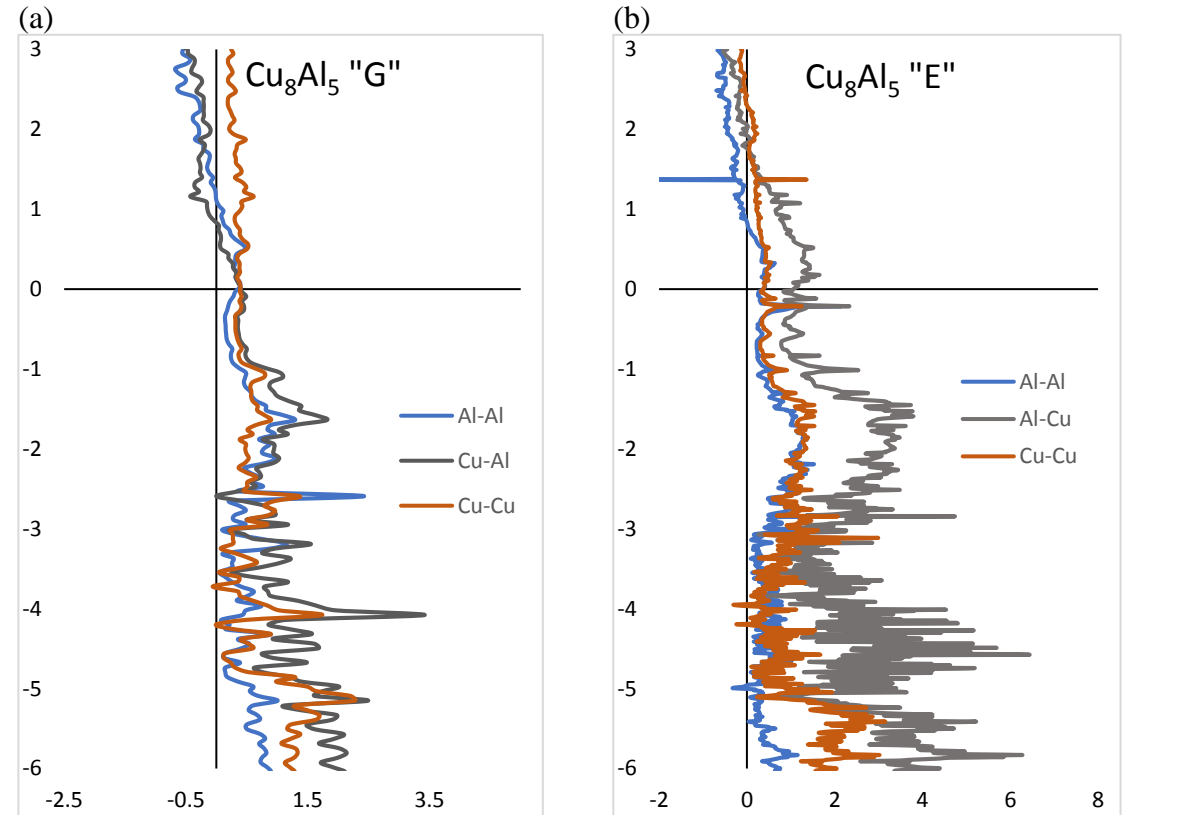
Figure 5.6: Cu$_8$Al$_5$ COHP utilizing experimental coordinates (a) COHP of model "G" a body centered decoration (b) COHP of model "E" a primitive decoration

Table 5.3 lists the percent bonding for models "E" and "G". By moving the Al from the IT and CO sites of separate clusters to the IT and OH sites of both clusters increases the direct contact between Al occupied sites at the cost of heteroatomic Cu–Al overlap. The primitive decoration is 0.692 eV lower that the body-centered decoration which parallels the findings of the Cu$_9$Al$_4$ γ-brass models.

Table 5.3: Bonding Analysis of Cu$_8$Al$_5$ by Element

	Cu$_8$Al$_5$ (cP52)	Cu$_8$Al$_5$ (cI52)
Bond type	% Bonding	
Cu-Cu	22.4%	24.7%
Cu-Al	60.4%	47.9%
Al–Al	17.2%	27.5%

Site preferences and charge density

Utilizing the charge density by means of evaluating the integrated density of states at individual sites can provide support for mixed site occupancies refined by SCXRD or, more valuably, provide insight into atomic decoration patterns when quality crystallographic data are missing. The latter is the case for ht-Cu_9Al_4 and the Al-rich end of this structure's reported phase width.   In Tables 5.4 the locations of individual sites are indicated with -A and -B to denote the A or B cluster where relevant. These calculations were performed using the experimentally refined coordinates. The values of IDOS/Atom in Table 5.4 were calculated by subtracting the charge built up at each atomic site from the number of valence electrons, as determined by the basis set employed for the calculation. The electronegativity of Cu, according to both the Pauling and Allen scales, is greater than that of Al [29], so that Al sites with negative IDOS/Atoms values are susceptible to mixing with Cu and Cu sites with positive IDOS/Atom values could be satisfied by Al mixing.

Table 5.4 shows the differences in charge distribution between the most energetically favorable primitive and body-centered atomic colorings. In both the primitive "Cu_8Al_5" and Cu_9Al_4 models the same polyhedral shell have a different sign for the value of IDOS/Atom and moving from innermost shell to outermost there are alternating signs from positive to negative within each 26-atom cluster. Regardless of the element occupying the site, the pattern of alternating charge density excess or deficiency remains unaltered. The positive IDOS/Atom values on the OT–B and OH–A of primitive Cu_9Al_4 indicate sites that have a driving force for mixing with Al and could be routes for uniform composition in the ht-phase. In the primitive "Cu_8Al_5" the negative values on the Al occupied IT-B site show this site could incorporate Cu. With mixing at these three sites, a rationale for a BCC decorated ht phase emerge.

Table 5.4: Charge Density Analysis

Cu$_9$Al$_4$ – cP52		Cu$_8$Al$_5$ – cP52	Cu$_9$Al$_4$ – cI52		Cu$_8$Al$_5$ – cI52
Element: (IDOS/Atom)	Shell	Element: (Δ IDOS/Atom)	Element: (ΔIDOS/Atom)	Shell	Element: (ΔIDOS/Atom)
Al: +0.060	(IT-A)	Al: +0.056	Al: +0.195	IT	Al: +0.192
Cu: -0.125	(IT-B)	Al: -0.013			
Cu: -0.172	(OT-A)	Cu: -0.224	Al: +0.150	OT	Cu: -0.299
Cu: +0.061	(OT-B)	Cu: +0.071			
Cu: +0.095	(OH-A)	Cu: +0.043	Cu: -0.071	OH	Al: +0.333
Cu: -0.129	(OH-B)	Cu: -0.111			
Cu: -0.142	(CO-A)	Cu: -0.128	Cu: +0.105	CO	Cu: +0.021
Al: +0.216	(CO-B)	Al: +0.190			

Regarding the body-centered decoration, the flipped decoration of the OT and OH shells highlight possible points for mixed site occupation which agrees with the results of the primitive decoration. The Cu occupied CO sites in both primitive decorated Cu9Al4 and "Cu$_8$Al$_5$" indicate that a driving force for Al substitution exists. Applying these finding to the assessment of phase width and potential coloring of the ht-Cu$_9$Al$_4$ phase, the driving force for a majority occupation of Al on the IT shell and mixing between Cu and Al on the CO shell is apparent. This further illustrates the competition between the site-energy and bond energy terms in total energies listed in Figure 5.4.

Geometry analysis and structure relaxation

In order to understand the role of the different geometries of clusters A and B in the stability of Cu9Al4, beyond the size differences expected from different numbers of each constituent element, an average cluster model is allowed to relax its atomic positions using VASP. The experimentally observed, stoichiometric decoration scheme for Cu9Al4 is applied to the averaged coordinates and over the course of the relaxation, the lattice parameters and atomic positions were allowed to optimize from the average positions shown in Table 5.1. The I-43m lattice relaxes to Cm, which represents a significant decrease in

symmetry. This suggests that the higher symmetry lattices are less favorable than lower

symmetry lattices, which supports the results of the phase diagram. The experimental

composition is likely comprised of mixed occupancy sites, that are not modeled well by the

relaxed structure, and add some degree of stability.

Table 5.5: Representative inter-shell distances before and after relaxation

Site	Experimental distance (Å)	Relaxed distance (Å)	% change
IT-A (Al)	2.849	2.919	+2.45
IT-B (Cu)	2.625	2.522	-3.93
OT-A (Cu)	4.196	4.052	-3.44
OT-B (Cu)	4.302	4.168	-3.12
OH-A (Cu)	2.520	2.438	-3.24
OH-B (Cu)	2.527	2.456	-2.80
CO-A (Cu)	3.265	3.458	+5.92
	4.279	4.163	-2.71
CO-B (Al)	3.336	3.283	-1.60
	4.242	4.142	-2.36

Shifts in atomic location which alter bond distances more than 15% are considered

influential to the geometry of individual clusters. Adjustments of bond distances below 15%

will be attributed to the innate differences in metallic radii. The metallic radius of Al is 1.43

Å and that for Cu is 1.28 Å [27]. Table 5.5 lists the bond distances for each intrapolyhedral

connection. These are not nearest neighbor interactions but are representative of changes

accrued during the structural relaxation. The shortest connections between atoms of each

polyhedral shell show a general trend that as the total volume of the Cu_9Al_4 cubic unit cell

decreased the atomic distances between atoms of the same shell decreased, with the

exception of the IT-IT connections of the centeral (A) cluster and the short contact between

CO atoms of the center A cluster. The differences in geometry between clusters A and B can

be explained by the differences in bonding distances within the Hume-Rothery solid solution

rules.

Conclusion

Calculations reveal two driving forces within this Cu–Al γ-brass system. Site preferences are driven by electronegativity, and charge density calculations reveal mixing on the OT and OH shells could provide a route from primitive to body-centered decoration at higher temperatures. The second driving force for stability in this phase is maximizing the heteroatomic Cu–Al pairwise interactions by separating the Al onto different sites and different clusters, yielding primitive decorations. The distinct geometries of each cluster reflect the optimal bond distances for maximizing Cu–Al bonding interactions, and may reflect idealized distances for mixed site bonding, which is not well modeled under the stoichiometric constraints of the chosen models. Relaxation of atomic coordinates from averaged atomic coordinates reveals that lower lattice symmetry is preferred for the Cu_9Al_4 decorations.

Acknowledgements

References

[1] Arnberg, L.; Westman, S.Acta Crystallographica A (24,1968-38,1982) (1978) 34, (*) p399-p404

[2] Mizutani, U., Hume-Rothery Rules for Structurally Complex Alloy Phases, CRC Press, New York, 2010

[3] Srinivasa Thimmaiah, Zachary Tener, Tej N. Lamichhane, Paul C. Canfield and Gordon J. Miller Zeitschrift für Kristallographie - Crystalline Materials, Volume 232, Issue 7-9, Pages 601–610, ISSN (Online) 2196-7105, ISSN (Print) 2194-4946,

[4] An Icosahedral Quasicrystal and Its 1/0 Crystalline Approximant in the Ca–Au–Al System Joyce Pham, Andreas Kreyssig, Alan I. Goldman, and Gordon J. Miller Inorganic Chemistry 2016 55 (20), 10425-10437,

[5] Yuan, Fang & Toombs, Asa & J. Miller, Gordon & Mozharivskyj, Yurij. (2018). Gd(Co1-xGax)2: Synthesis, crystal structures, and investigation of structural transformations and magnetic properties. Journal of Solid State Chemistry. 264.

[6] U. Mizutani, Hume-Rothery Rules for Structurally Complex Alloy Phases, Boca Raton: CRC Press, 2011

[7] A. F. Phragmen and G. Westgren, "X-Ray Studies on Alloys," *Metallwirtschaft,* pp. 380-385, 1929.

[8] H.-G. von Schnering and R. Nesper, "Li21Si5 Hume Rothery and Zintl," *Journal of Solid State Chemistry,* pp. 47-52, 1987.

[9] A. Westgren and G. Phragmén, Z. Anorg. Chemie, 175 (1928) 80

[10] A. Johansson, H. Ljung and S. Westman, "X-Ray and Neutron Diffraction Studies on gamma-Ni, Zn and gamma-Fe. Zn," *Acta Chemica Scandinavica,* vol. 22, pp. 2743-2753, 1968

[11] Hyunjin Ko, Olivier Gourdon, Delphine Gout, Eun-Deok Mun, Srinivasa Thimmaiah, and Gordon J. Miller Rhombohedrally Distorted γ-Brasses Cr1−xFexGa Inorganic Chemistry 2010 49 (24), 11505-11515

[12] Brandon, J.K.; Brizard, R.; Pearson, W.B.; Tozer, D.J.N. Gamma-brasses with I and P cells, Acta Crystallographica B (24,1968-38,1982) (1977) 33, (*) p527-p537

[13] Stokhuyzen, R.; Brandon, J.K.; Chieh, P.C.; Pearson, W.B Copper-gallium, gamma Cu9 Ga4, Acta Crystallographica B (24,1968-38,1982) (1974) 30, (*) p2910-p2911

[14] Ljung, H.; Westman, S. X-ray determination of the structure of the primitive cubic gamma Ni, Cd phase, Acta Chemica Scandinavica (1-27,1973-42,1988) (1970) 24, (*) p611-p617

[15] Arnberg, L. The structures of the gamma-phases in the Pd-Cd and Pt-Cd systems, Acta Crystallographica B (24,1968-38,1982) (1980) 36, (*) p527-p532

[16] Brandon, J.K.; Kim, H.S.; Pearson, W.B., The crystallographic analysis of In Mn3, a new form of gamma - brass structure with a P cell, Acta Crystallographica B (24,1968-38,1982) (1979) 35, (*) p1937-p1944

[17] Murray J.L., Al-Cu (Aluminum-Copper), Binary Alloy Phase Diagrams, II Ed., Ed. T.B. Massalski, Vol. 1, 1990, p 141-143

[18] De Lima J.C., Triches D.M., Dos Santos V.H.F., and Grandi T.A., Formation of γ-$Cu_{67}Al_{33}$ alloy by mechanical alloying, J. Alloys Compd., Vol. 282, 1999, p 258-260

[18] Tian, Yanhong & Hang, C & Wang, Chunqing & Zhou, Y. (2007). Evolution of Cu/Al Intermetallic Compounds in the Copper Bump bonds during Aging Process. IEEE Electron Packag Technol. 10.1109/ICEPT.2007.4441444.

[19] K. Rajan and E. R. Wallach. A transmission electron microscopy study of intermetallic formation in aluminum-copper thin film couples. J Crystal Growth 1980; 49: 297-302

[20] H. J. Kim, J.Y. Lee, K. W. Paik, et al., Effects of Cu/Al Intermetallic Compound (IMC) on Copper Wire and Aluminum Pad Bondability. Trans Comp and Packg Technol 2003; 26(2): 367-374

[22] Jepsen, O.; Andersen, O.K. TB-LMTO, version 47; Max-Planck-Institut für Festkörperforschung: Stuttgart, Germany, 2000

[23] (a) Kresse, G.; Hafner, J. Phys. Rev. B1993, 47, 558. (b) Kresse, G.; Hafner, J. Phys. Rev. B1994, 49, 14251,

[24] Kresse, G.; Furthmüller, J.Comput. Mat. Sci.1996, 6, 15.,

[25] Kresse, G.; Furthmüller, J. Phys. Rev. B1996, 54, 11169.,

[26] Kresse, G.; Joubert, D. Phys. Rev. B.1999, 59, 1758.,

[27] Greenwood, Norman N.; Earnshaw, Alan (1997). Chemistry of the Elements (2nd ed.). Butterworth-Heinemann.

[28] Y. Tamou, J. Li, S. W. Russell, and J. W. Mayer. Thermal and ion beam induced thin film reactions in cu-al bilayers. Nucl Instrum Methods Phys Res 1992; B64: 130-133

[29] J. B. Mann, T. L. Meek, E. T. Knight, J. F. Capitani and L. C. Allen, "Configuration Energies of the d-Block Elements," *J Am. Chem Soc.,* vol. 122, no. 21, pp. 5132-5137, 2000.

126

Supporting Information

Table SI5.8.1: Decoration Scheme for Cu$_9$Al$_4$

Trial	IT-B	OT-B	OH-B	CO-B	It-A	OT-A	OH-A	CO-A
C	Cu	Cu	Cu	Al	Al	Cu	Cu	Cu
C'	Al	Cu	Cu	Cu	Cu	Cu	Cu	Al
D	Al	Al	Cu	Cu	Al	Al	Cu	Cu
E	Cu	Al	Cu	Al	Cu	Cu	Cu	Cu
E'	Cu	Cu	Cu	Cu	Cu	Al	Cu	Al
F	Al	Cu	Cu	Al	Cu	Cu	Cu	Cu
F'	Cu	Cu	Cu	Cu	Al	Cu	Cu	Al
G	Cu	Cu	Cu	Al	Cu	Al	Cu	Cu
G'	Cu	Al	Cu	Cu	Cu	Cu	Cu	Al

Coloring schemes indicated with a (') have switched the atomic decoration between Cluster A to Cluster B. All models here reference the experimental atomic coordinates from Table 5.4.1
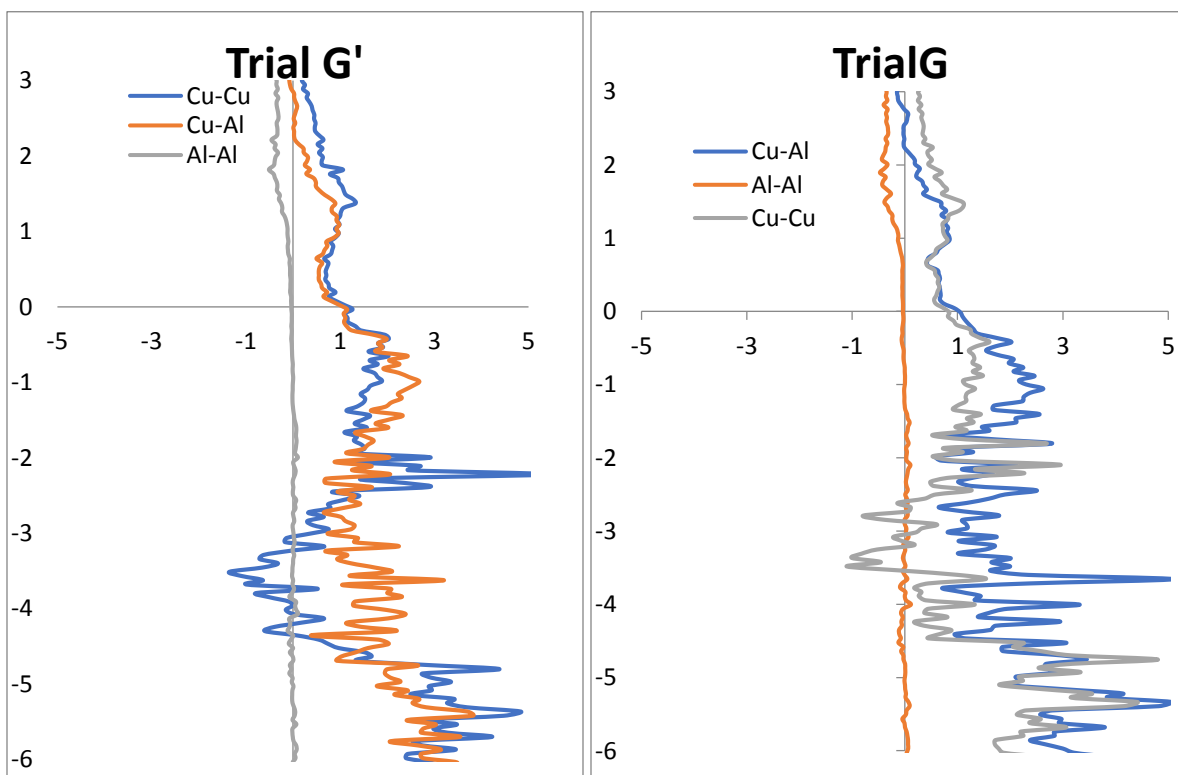
COHP for colorings "G" and "G'"
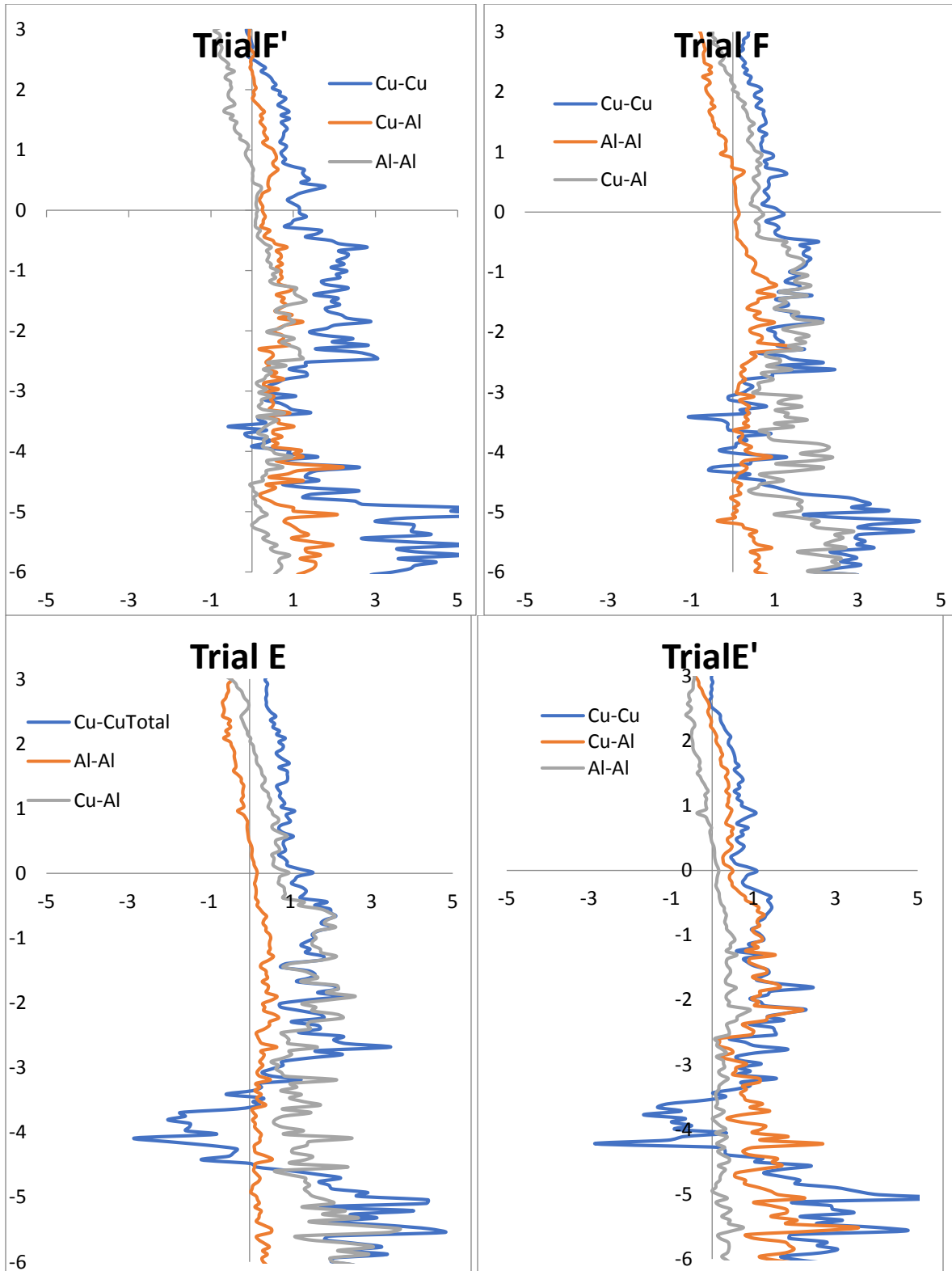
COHP for less energetically favorable trials

Bonding by Element

	Cu-Cu%	Cu-al%	Al-Al%
C	38.03	56.64	5.33
Cp	37.34	55.62	7.04
D	29.01	49.51	21.48
Dp	32.22	44.13	23.65
E	36.93	50.72	12.35
Ep	41.79	43.96	14.26
F	36.48	45.99	17.53
Fp	54.00	25.69	20.31
G	34.09	64.27	1.64
Gp	41.63	56.77	1.60
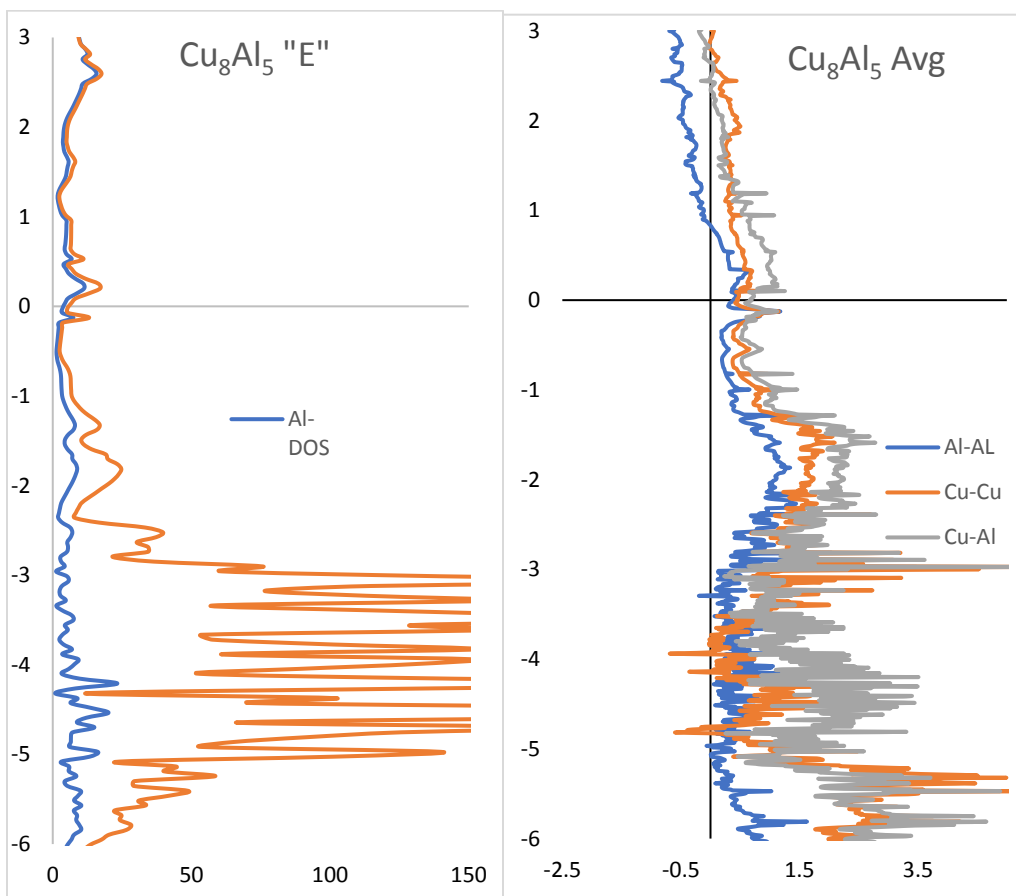
Density of states comparing Trial E and Averaged Coordinates for Cu_8Al_5 composition

CHAPTER 6: CONCLUSIONS

The work in this dissertation investigated the synthesis, electronic structure, and bonding schemes of γ-brasses in the Mn–Zn–Al, Mn–Zn, and Cu–Al systems. The results deepen our understanding of the role of *e/a* ratios and local bonding environment have on the formation, and stability of complex metallic alloys (CMAs) of group I and group II γ-brasses.

Synthesis of binary Mn–Zn and ternary Mn–Zn–Al γ-brasses shows the role of valence electron concentration on the lattices of CMAs. From an understanding of previous work in the Co–Zn system an analogous binary, cI52 Mn – Zn γ-brass was synthesized while independently a binary, hR78 Mn–Al γ-brass was discovered. Systematic doping of Zn from the middle of the phase width in the Mn–Al system, Mn_5Al_8, connected the two binaries through a *e/a* driven structural transformation.

Electronic structure calculations elucidated the role of Zn *d* orbitals in the $Mn_{2+x}Zn_{11-x}$ as well as preferred sites for Al and Zn in the ternary series, which complements the SCXRD refinements from quality data. Hypothetical coloring models show adding Zn to any Al occupied site in the Mn–Al γ-brasses promotes a structural transition toward the cubic, although, Zn occupation of specific sites sequentially optimizes the structural transition. In binary compounds with significant Zn content the minority component mixes occupancy of specific sites to minimize unfavorable Zn–Zn orbital overlap. For the binary Mn–Al γ-brasses multiple coloring models indicate an optimum number of electrons for each 26-atom cluster to be 104-105 electrons.

Electronic structure studies of the Cu-Al systems γ-brasses show an atypical coloring of a cP52 structure is stabilized by increased heteroatomic bonding and minimization of Al-Al contact through both the decoration and geometry of individual clusters. Charge density

calculations show specific sites have a driving force to mix Al and Cu, which increases overall Al content and could explain the change in decoration associated with a high temperature cI52 phase.

APPENDIX: ADDITIONAL REACTIONS

Mn–Zn–Al System

Loading Composition	Synthetic process	Results	Series number
$Mn_{0.984}Zn_{1.027}Al_{1.022}$	Ramp to 400 and anneal for 48 hours slow cool	Mixed phase Possible γ-brass	SE001
$Mn_{0.995}Zn_{1.933}Al_{1.022}$	Ramp to 800°C at 1°/min. dwell at 800 for 12 hours cool at 0.1°/min to 700°C and anneal for 138 hours. Slow cool inside furnace	Zn escaped	SE002
$Mn_{1.012}Zn_{0.990}Al_{2.000}$		Severe oxidation Zn escaped	SE003
$Mn_{1.017}Zn_{2.038}Al_{2.000}$			SE004
$Mn_{1.001}Zn_{1.990}Al_{1.002}$			SE005
$Mn_{0.978}Zn_{0.973}Al_{2.001}$			SE006
$Mn_{0.996}Zn_{1.989}Al_{1.972}$			SE007
$Mn_{0.994}Zn_{0.991}Al_{0.986}$		Zn boiled off, oxidation	SE008
$Mn_{0.999}Zn_{2.027}Al_{1.074}$		Mn oxidation	SE009
$Mn_{1.977}Zn_{1.028}Al_{1.003}$		Mixed phases	SE010
$Mn_{0.997}Zn_{1.017}Al_{2.036}$		Reacted with Ta tube	SE011
$Mn_{1.986}Zn_{2.014}Al_{0.991}$		oxidation	SE012
$Mn_{2.011}Zn_{0.983}Al_{1.975}$		Mn unreacted	SE013
$Mn_{0.992}Zn_{2.036}Al_{19.73}$		Reacted with Ta tube	SE014
$Mn_{1.016}Zn_{0.994}Al_{1.007}$	Ramp to 750°C at 1°/min. dwell at 750 for 48 hours cool at 0.1°/min to 600°C and anneal for 128 hours. Slow cool inside furnace	Mixed Mn and Zn oxides	SE015
$Mn_{1.246}Zn_{0.994}Al_{0.994}$		destroyed	SE016
$Mn_{0.749}Zn_{0.999}Al_{0.994}$		amorphous	SE017
$Mn_{0.995}Zn_{2.113}Al_{1.214}$		Zn boiled off, mixed oxides	SE018
$Mn_5Zn_6Al_2$	Ramp to 600°C at 1°/min. dwell at 600 for 6 hours. Ramp to 800 at 1 °/min and dwell for 24 hours. cool at 0.01°/min to 400°C and anneal for 48 hours. Slow cool inside furnace	γ-brass + amorphous	SE020
$Mn_5Zn_5Al_3$		γ-brass	SE021
$Mn_5Zn_4Al_{1.214}$		γ-brass	SE022
$Mn_{0.995}Zn_{2.113}Al_{1.214}$		γ-brass	SE024
$Mn_{0.995}Zn_{2.113}Al_{1.214}$		γ-brass	SE025

Mn – Zn Series

Loading Composition	Synthetic process	Results	Series number
$Mn_{3.5}Zn_{1.5}$	Ramp to 800°C at 4°/min. dwell at 750 for 24 hours cool at 0.1°/min to 650°C and anneal for 168 hours. Slow cool inside furnace	Zn boiled off, Ta tube cracked, contents lost	SE026
Mn_3Zn_2			SE027
$MnZn$			SE028